ANTI-BIOFOULING IMPLANTABLE CATHETER USING THIN-FILM MAGNETIC MICROACTUATORS

A Dissertation

Submitted to the Faculty

of

Purdue University

by

Qi Yang

In Partial Fulfillment of the

Requirements for the Degree

of

Doctor of Philosophy

August 2019

Purdue University

West Lafayette, Indiana

THE PURDUE UNIVERSITY GRADUATE SCHOOL
STATEMENT OF DISSERTATION APPROVAL

Dr. Hyowon Lee, Co-Chair

Weldon School of Biomedical Engineering

Dr. Pedro Irazoqui, Co-Chair

School of Electrical and Computer Engineering

Dr. Jeffrey Rhoads

School of Mechanical Engineering

Dr. Babak Ziaie

School of Electrical and Computer Engineering

Approved by:

Dr. Dimitrios Peroulis

Head of the School Graduate Program

To my parents

ACKNOWLEDGMENTS

The past five year has been a unique journey where I grew remarkably as a scholar and an individual. I feel very fortunate to accomplish a research project that spans from theoretical design to therapeutic outcome on animals. I would not have been able to complete this manuscript and reach current level of maturity without a strong supporting system. I would like to recognize individuals and groups that helped me along the way from many aspects.

First of all, I would like to thank my advisor Dr. Hyowon 'Hugh' Lee for offering the opportunity to work on this exciting project when I was a new college graduate without a single research credential under my belt. I appreciate his early hands-on guidance on design of a MEMS system and in-depth discussion on microfabrication techniques. I am grateful for his frequent and timely feedback which ultimately pushed me to unleash my potential to become an independent researcher. I endeavor to match his level of critical thinking, attention to detail, and logical clarity.

I would also like to express my gratitude towards my committee members Dr. Rhoads, Dr. Irazoqui and Dr.Ziaie. I appreciate their time and effort spent on providing comments on exams and thesis writing. In particular, I thank Dr. Rhoads for offering technical insights on vibrational systems as well as Jacob Miller for assisting with LDV setup. I must also thank Dr.R.T. Bentley for preforming the animal surgery and feedback on experimental design. His expertise in veterinarian medicine played an integral part in this work. I am also appreciative for the help from Robyn Maccain, Christa Crain and other staffs from vet school during animal treatments.

I was lucky to meet a group of brilliant peers from whom I received strong support. I would like to thank my colleagues and good friends Hyunsu Park and Tran Nguyen for their assistant with fluorescent imaging and technical feedback. More importantly, I appreciate our meaningful conversations about shared interests, life goals and challenges at the time when we were the sole members in the lab. I also thank my good friends and LIMR colleagues Bahar Dhowan, Chunan liu, Angel Enriquez, Haesoo Moon, Jongcheon Lim, James Nolan, Jinjia Xu and Jian Xu for timely assistant with experiments and memorable fun times spent outside the lab. Of course, I would like to thank my undergraduate colleagues Dillan Nayee, Ryan Harris, Doug Satoski, Christian Figueroa-Espada, Adam Killeen and Barnabas Obeng-Gyasi for providing critical aids to auxiliary experimental setups and measurements. Without their help I would not have completed the project in time.

Finally, I express my highest gratitude towards parents Richard and Elizabeth. I cannot thank enough for their unconditional love and support behind my decision to pursuit this PhD study. I strive to become the best of myself because of them.

TABLE OF CONTENTS

Page

Page

LIST OF TABLES

LIST OF FIGURES

Figure Page

Figure Page

ABSTRACT

Yang, Qi PhD, Purdue University, August 2019. Anti-Biofouling Implantable Catheter Using Thin-Film Magnetic Microactuators. Major Professor: Hyowon Lee.

Hydrocephalus is a neurological disease characterized by abnormal accumulation of cerebral spinal fluid (CSF) in ventricle of brain. 1 in 1000 newborns are affected each year and it is life-threatening if left untreated. The golden standard of treatment is to surgically implant a shunt that divert excessive CSF away from ventricle to alleviate intraventricular pressure (ICP) in patient. Unfortunately, shunt failure rate is notoriously high because of obstruction of catheter intake pore. The obstruction is primary caused by normal and inflammatory tissue (biofilm) buildup over time. Shunt replacement surgery is typically required after only 1 year of implantation for 40% of patients. To prolong the lifespan of hydrocephalus shunt, we previously proposed and designed magnetic micro-actuators platform to remove biofilm mechanically. Removal of muscle cells and microbeads were demonstrated from wafer level devices on bench-top.

To examine device efficacy in ventricular catheter, I developed magnetic actuator on polymer substrate. First, polyimide-based flexible thin-film devices were micro-fabricated and integrated into a single-pore silicone catheter. A proof-of-concept self-clearing smart catheter was presented. Removal of microscopic biofilm was evaluated against bovine serum protein (BSA). Detachment of BSA up to 95% was achieved by shear stress from magnetic actuation. Next, I developed resistive deflection sensing using a metallic strain gauge, allowing device alignment with magnetic field for maximum energy delivery. In addition, auxiliary functionalities such as occlusion detection and flow rate measurement were demonstrated on catheter. Moreover, a new serpentine cantilever geometry with increased magnetic volume was proposed for

improved delivery of torque and deflection. In a bench-top evaluation, we showed prolonged catheter drainage (7x) in a dynamic fluid environment containing macroscopic blood clots. Finally, using an intraventricular hemorrhage (IVH) porcine model, we observed that self-clearing catheter had longer survival than control catheter (80% vs. 0%) over the course of 6 weeks. Animals treated with magnetic actuation had significantly smaller ventricle size after 1 week of implantation.

1. INTRODUCTION

1.1 Hydrocephalus

Hydrocephalus is a neurological disorder characterized by an abnormal accumulation of cerebral spinal fluid (CFS) in ventricle of the brain. Although precise definition is controversial, the disease is associated with elevated intracranial pressure (ICP) and dilatation of cerebral ventricle. The symptoms vary with age and severity. For infants, the most notable sign is enlargement of skull because of CSF buildup. For older patients, headache, vomiting, nausea, blurred or double vision, poor coordination, urinary incontinence and or cognition problems can occur [1].

It is commonly observed in children with approximately 1-2 newborns diagnosed for every 1000 in the US [2, 3]. There were nearly 40,000 new admissions, 433,000 hospital days spend for pediatric hydrocephalus each year [4]. It is the most common disease treated by pediatric neurosurgeons and accounts for roughly $2 billion in health expenditures in the United States every year [4, 5].

According to traditional bulk flow model, CSF is secreted by the choroid plexus epithelium in the cerebral ventricles. It flows into the subarachnoid spaces, and enters the cerebral venous system via the arachnoid granulations [5]. For a hydrocephalic individual, the production and absorption of CSF is imbalanced due to an obstruction to the CSF flow. In rare cases, hydrocephalus is caused by overproduction of CSF. If untreated, elevation of ICP can lead to irreversible central nervous system (CNS) injury and could be life threatening.

Congenital hydrocephalus is present at birth and may be caused by genetic abnormalities or developmental disorders such as spina bifida and encephalocele. Acquired hydrocephalus develops at time of birth or at some point afterward caused

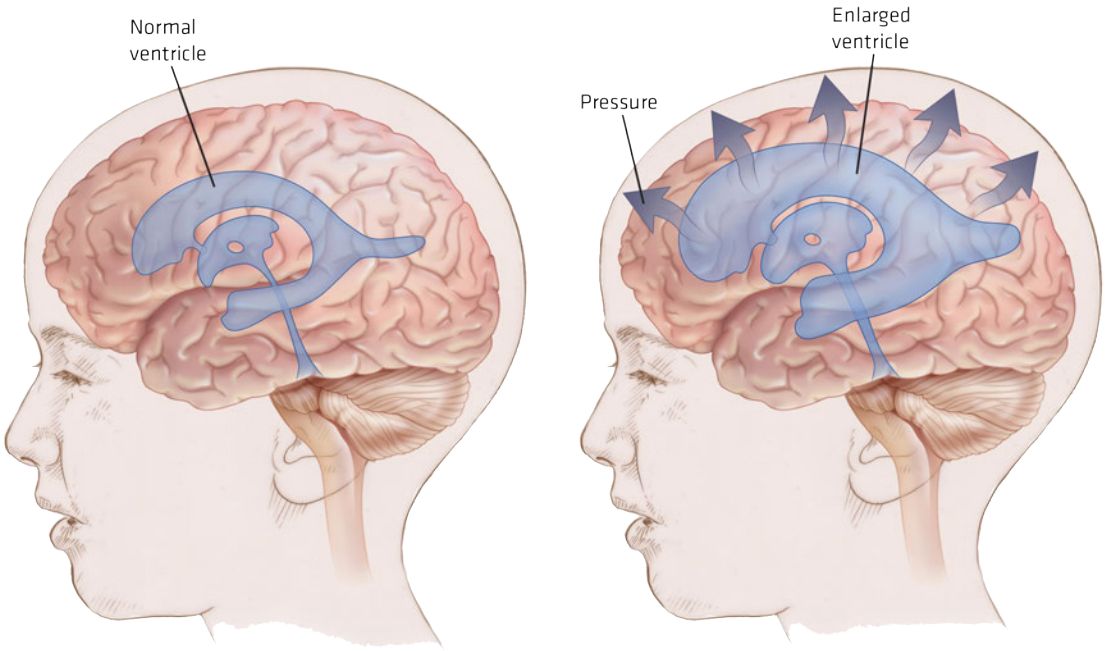

Fig. 1.1. Left: a brain with normal ventricle. Right: a brain with enlarged ventricle. Image reprinted from [6].

by subarachnoid hemorrhage, head trauma, infection, brain tumor, or other surgical complications [1].

1.1.1 Treatment

Shunt

For acute cases where ICP becomes dangerously high, patients are treated by external ventricular drainage (EVD) to immediately release CSF and inflammatory fluids outside of brain. For long-term in-patient management, most hydrocephalic patients are treated by a hydrocephalus shunt, an implanted drainage path to divert excessive CSF. The shunt consists of three components. A proximal catheter is used

for CSF intake. Next, a valve is connected to regulate flow and pressure to prevent over-drainage and posture related siphoning. Following the valve, a distal catheter is connected for fluid exit (Fig. 1.2-1.3). Shunt is typically made from silicone, a polymer biocompatible material used extensively in various medical applications [7,8]. Proximal catheter is placed in cerebral ventricle or lumber system and distal catheter is planted at abdomen or atrium of heart [1]. Ventriculo-peritoneal shunt (VPS) is the most common type in practice. It diverts CSF from ventricle to peritoneal cavity. Ventriculo-atrial shunts, lumbo-peritoneal shunts are occasionally used [5]. Each year an estimation of 400,000 shunt-related operations are performed in the United States [9, 10]. Unfortunately, shunting has enormous complications related to infection and malfunction. Long term shunt survival reliability is extremely poor.

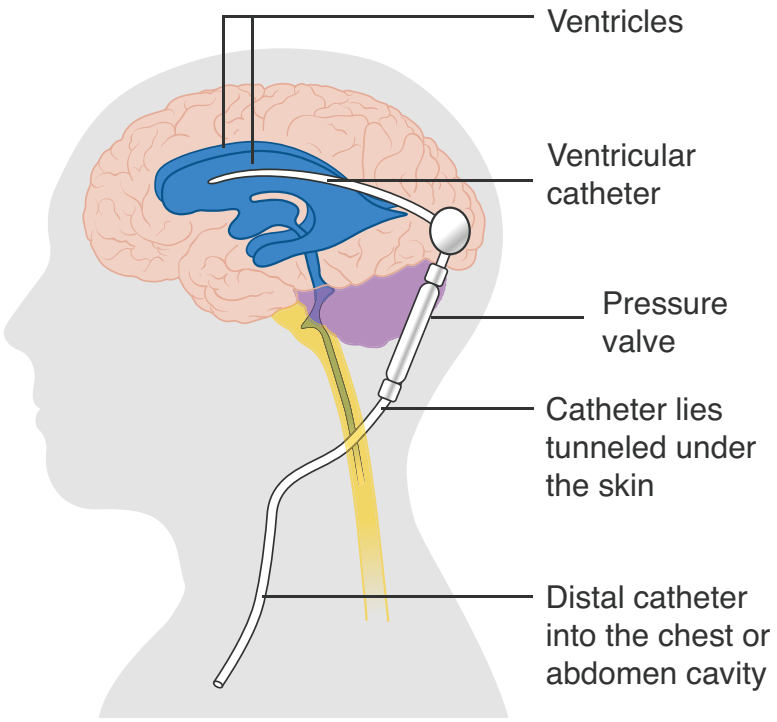

Fig. 1.2. Excessive CSF enters ventricular catheter and exits from distal catheter at abdomen or chest. Image adapted from wikimedia commons.

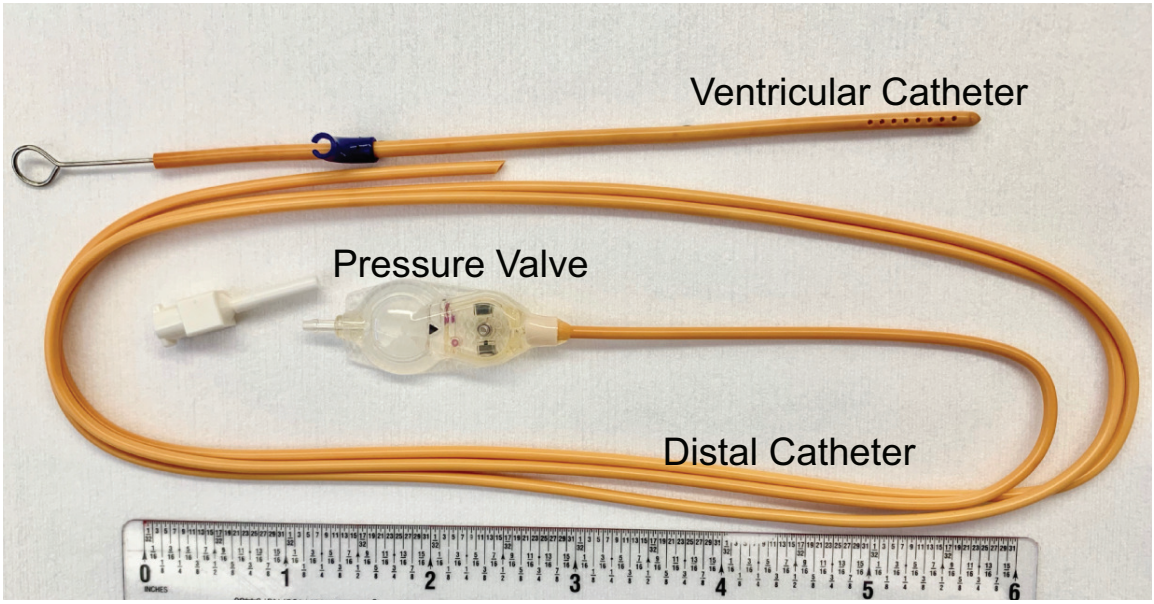

Fig. 1.3. A full set of VP shunt consists of ventricular catheter, programable pressure valve, distal catheter and connectors. Model 82-8803PL from Codman is shown.

Endoscopic third ventriculostomy (ETV)

Endoscopic third ventriculostomy (ETV) is an alternative surgical procedure for treatment of non-communicating (obstructive) hydrocephalus, the case where CSF flow is obstructed within the ventricle. This procedure requires endoscope to access into third ventricle. A puncture is made to open the floor of third ventricle, enabling a direct communication into prepontine cistern [5, 11]. Studies suggest that EVT is advantageous in long term treatment survival [12] in comparison to shunt. However, there is a high rate of early failure, particularly in infants [13]. Therefore VPS remains the standard of care for adult patients and children older than 2 years of age [5].

1.2 Shunt Failure

Shunt systems are notorious for their extremely high failure rate. More than 40% of patient experience shunt failure within 1 year and up to 85% experience within 10 years of implantation [14,15]. Apart from infection, shunt malfunction is the primary failure mode. Extreme physical movement can cause undesired shunt dislocation or disintegration of catheter. [15, 16]. Most shunt malfunctions, however, are caused by an obstruction in one or multiple locations within the drainage path, including proximal catheter, valve or distal catheter. Shunt failure is diagnosed by expansion of ventricle volume. Imaging techniques such as computed tomography and magnetic resonance imaging are typically used to determine the level of occlusion. Once an obstruction is confirmed a revision surgery is required to replace the failed component or the entire shunt system. Shunt revision surgery has become a routine procedure that burdens both patients and healthcare givers. As high as 70% of hydrocephalus related surgeries were shunt revision operations [15]. Furthermore, there is an increase in shunt failure risk associated with each additional number of revision surgeries [17]. Therefore, there is an urgent need for a robust, failure-free shunt system.

Fig. 1.4. Occluded ventricular catheters removed during shunt revision surgeries. Image reprinted from Lin et al [18] with permission.

1.2.1 Shunt Obstruction

Implantable medical device is susceptible to attachment of biological materials over the course of implantation. Hydrocephalus shunt is no exception as it is placed at a biological environment where proteins, cells, tissues, blood clots and other biofilms exist. Proximal end of hydrocephalus shunt is the most likely location to occlude. About one third of the occlusion is found at the valve or inlet pore of ventricular catheter [14, 19–21] as shown in Fig. 1.4. Normal brain tissues, such as choroid plexus, white or grey matter and connective tissue can invade and infiltrate ventricular catheter. It has been suggested that physical proximity or a pressure driven contact can cause tissue ingrowth and eventually mechanical blockage of inlet pore [22, 23]. Pathological tissue (red blood cells, platelet, blood-borne or CNS inflammatory cells) can also enter proximal end of catheter. Catheter insertion related injury response or secondary injuries from mechanical agitation can inflicts pathological tissues growth around ventricular catheter. If ventricular hemorrhage is incited during surgery, blood clots may form via platelet mediated adhesion. Hemorrhagic debris could enter and obstruct the pore or downstream. Inflammatory cells are the last type of material that triggers shunt occlusion [16, 24]. When a foreign object is introduced inside the brain, a series of foreign body response is initiated. Local inflammatory and wound-healing response produce cells that adheres at catheter sidewalls. Lymphocytes, macrophages, mast cells, giant cells and fibrin matrix, etc. have been observed to cause cellular buildup and eventual obstruction [24–27]. Undesired cellular buildup is commonly referred as biofouling (or fouling) in biomedical, marine and water treatment industries. Immune response related fouling not only hinders reliability for hydrocephalus shunt but also plagues other implants such as chronic neurostimulation and neurorecording devices (Fig. 1.5).

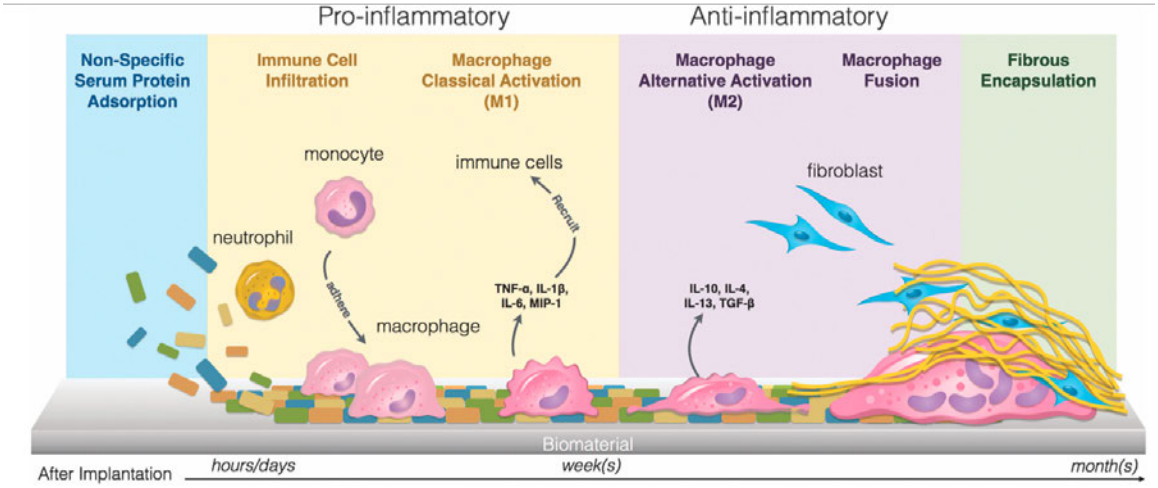

Fig. 1.5. Upon implantation of biomaterials, foreign body immune response cause biofilm accumulation and encapsulation over time. Image reprinted from [28] with permission.

1.2.2 Obstruction Prevention Strategies

Since the introduction of shunt usage in 1955 by Pudenz [29,30], various obstruction prevention methods have been proposed and studied in vitro, in vivo or in clinical practice. Here, a brief review of obstruction management at ventricular catheter is presented. Improvements made at pressure valves and distal catheter is outside the scope of this manuscript and therefore not being discussed.

Surgical Remediation

Surgical techniques were developed to alleviate shunt occlusion at initial implantation or subsequent operations. For instance, Kehler et al. [31] employed a ventricular sheath that is peeled away after placement of catheter to avoid infiltration of brain tissue upon insertion. A nonsignificant 13% revision decrease was reported within 1 year of shunt implantation.

Pattispu et al. [32] utilized electrocautery to removal obstruction material from electrically generated heat. This procedure is done post-occlusion and requires endoscope to access inner lumen of ventricular catheter. A 85% shunt survival rate was observed post-operation within 20 months in a study carried out on 20 patients.

Ultrasonic cavitation has been explored to clear up occluded pores as well. Ginsberg et al. [33] designed a low frequency ultrasound system that can deliver sound wave at 20-28 KHz to produce localized cavitation. The miniaturized system was inserted into shunt catheter lumen during surgeries. An in vitro sheep study revealed 90% of pores were cleared from choroid plexus blockage.

Laser was used to remove obstructing biofilms found in ventricular catheters. Chrstens-Barry et al. [34] demonstrated in vitro removal of choroid plexus, scallop and 8% polyacrylamide by delivering focused and pulsed laser with energy from 200 mJ to 400 mJ.

Initial catheter position inside the brain also plays a role in the development of catheter occlusion. Prolonged shunt survival can be achieved when placing ventricular catheters in the frontal horn, anterior to the choroid plexus [24, 35–37]. In some cases, decreased rate of failure was found when immersing ventricular catcher tip in CSF [38]. Furthermore, Harris et al. [15] indicated that gravity enhances macrophage and astrocyte adhesion on lower half of catcher inner lumen parallelled to the ground. Therefore, tilting angle may play a role in reducing occlusion risk.

Aforementioned strategies may reduce the need and frequency of a full revision surgery to some extent; however, they require invasive interventions from highly trained personnel. Hence, an autonomous and in-patient obstruction prevention approach may be more advantageous.

Surface Approaches

Many attempts focused on superior material substitute to silicone or surface coatings less likely to attract biofilms. For instance, in 1991 Wong et al. tested poly-

2-hydroxyethyl methacrylate (pHEMA) because of its hydrophilicity and gel-like nature [39]. Recent studies suggested that pHEMA can impede cell attachment and protein deposition [40–43]. However, the occlusion prevention outcome was minimal. Six out of seven explanted devices were covered by fibrous encapsulation in an in vivo study.

Ellis et al [44], in association with Medtronic, reported the use of 'extracted silicone' (commercially branded extracted Delta valve and extracted ventricular and peritoneal catheters) as shunt material. Extracted silicone was removed of silicone oligomers, a small composition native to standard silicone elastomers. Unpolymerized oligomers was removed because it interacts with immune system and elicit inflammatory response. Two clinical cases studies showed prolonged life time (revision free for > 1 year) for children hypersensitive to silicone [44, 45].

Patel et al [46], studied neuron cell proliferation on hydrophobic monomers with additional coating agents. Fuoroalkylsilane (FAS), anticoagulant heparin and hyaluronan were coated on silicone sheets and tested. They indicated that FAS reduced astrocyte growth in vitro while heparin and hyaluronan did not lower cell attachment compared to bare silicone. All three coatings failed to prevent choroid plexus binding. It was suggested that polymer surface characteristic, other than wettability, may play a role in specific cell adhesion.

Polyvinyl pyrrolidone (PVP) was another material coated on silicone to improve shunt functionality and reliability. PVP is a hydrophilic material that was used to inhibit fibroblast adhesion [47]. In 1997, Medtronic introduced PVP coated hydrocephalus shunt under the commercial name 'Bioglide'. It was advertised for easy insertion of catheter during surgical placement. Its smooth surface minimizes tissue damage and therefore reduces the chance of inflammatory response [48]. Although PVP coated catheter showed lowered bacteria adhesion [49, 50], subsequent report indicated that the use of PVP coated catheter had little to no improvement in infection over bare silicone catheter. Bioglide was eventually taken off market in 2010 because

its lubricous surface was unable to provide enough friction for a reliable lock between catheter and pressure valve connector.

Antibiotic-impregnated shunt surface was also utilized to prevent or reduce CSF infection. For instance, Izci et al [51], examined the efficacy of silver impregnated polyurethane tubing against CFS infection from bacteria. The surface lowered CSF protein and bacterial level after one month of implantation. However, its long term efficacy has yet to be studied.

Catheter pore modification

The architectural design of ventricular catheter is an ongoing interest of modification. The effect of ventricular catheter hole location, size and quantity was studied and manipulated. Typically, holes of ventricular catheters are evenly spaced and identical in size with diameter between 500 μm to 1000 μm. Lin et al indicated that holes at the most proximal end of the catheter is the primary location of obstruction [18]. According to their computational fluid dynamic (CFD) study, the two most proximal holes receive 80% percent of flows in an eight-hole catheter system. To avoid large influx of biofouling material from CSF at the proximal hole, a design featuring gradually decreased hole diameters away from tip end was proposed. The design evenly distributes flow intake among the holes, preventing a less aggressive fluid intake. A subsequent study on number of holes and ratio between hole/segment was reported by Galarza et al [52]. Furthermore, reducing the number of holes from 32 to 6 or even one can potentially increase shunt patency [27, 53]. It was suggested that reduced number of opening lowers the chance of tissue infiltration without reducing flow velocity [27, 54]. Shear stress was identified as a key factor that affects biofilm attachment strength [15, 18, 55, 56]. Harris, et al. indicated that there was an increase in macrophage and astrocyte adhesion with higher shear stress. The positive dependence between shear stress and cell adhesion was observed in the range between 0 to 0.01 N/m^2. It was also suggested that this relation is threshold dependent. High

shear stress above a certain limit reduces cellular attachment [15,57–59]. In addition, the effect of hole shape has been studied [60]. Conical hole alters flow distribution and reduce local shear stress as compared to conventional cylindrical hole. Hole sidewall roughness is another factor that affects cellular adhesion [61–63]. Lowered cell adhesion might be achieved using smooth surface from advanced hole patterning technics. Despite efforts made from computational and bench-top studies, catheters with hole modification have yet to be tested systematically in vivo or in patient for functional evaluation, best to author's knowledge.

1.3 Passive Anti-fouling Strategies

Passive fouling prevention strategies aim to reduce biofilm binding autonomously without external human intervention. It has been an ongoing area of research as the need for reliable chronic implantable devices is increasingly recognized. These methods primarily focus on modifications in material, geometry, surface physical and chemical properties.

Typically, a decrease in interfacial energy between implant material and targeted biofilm is engineered to achieve anti-fouling outcome. Common anti-fouling materials, such as polyethylene glycol (PEG) terminated polymers [64, 65], perfuoropolyether-based random terpolymers [66], zwitterionic polymers [67,68] and phosphazene polymers [69] have been extensively studied and tested against proteins, bacteria and fungus.

Release of nitric oxide (NO) was suggested to inhibit biofilm proliferation. NO is a gas molecule that prevents platelet adhesion, thrombus formation and bacteria reproduction. It was also utilized to promote wound healing and biofilm dispersal by chemical reactions [70–79]. NO release layer was engineered to incorporate onto donor substrates, such as silicone and teflon, for applications from water treatment to implantable grafts and stents [75, 78, 80–83]. However, NO release surface has finite dose and the gas is typically consumed within days or even hours. Therefore, the

use of NO release may have limited impact for chronically implanted applications. Currently, It has never been used for addressing hydrocephalus shunt failure, best to author's knowledge.

Next, with advancement in microfabrication and nanotechnology, customized microscopic surface structures were patterned to prevent microbial growth. Chung, et al, reported an engineered biomimetic micro-topography based on skin of sharks that disrupts biofilm formation [84]. Protrude micro-columns were designed on PDMS substrates to penetrate and rupture cell walls. Greatly reduced bacterial proliferation was demonstrated within 30 days test period.

Evenly spaced nano-pillars topography, observed from cicada wings, was found to have bactericidal effect [85]. The structural origin of such effect was explained by Pogodin et al [86]. A mathematical model was established to describe bacteria deformation on top of nano-pillars arrays. PMMA substrate has been used to realize nano-pillar surface from using nano-imprint lithography. The substrate was shown effective in killing gram negative E-coli in vitro [87].

Although these passive anti-fouling strategies are encouraging in reducing the progression of micro-scale biological film attachments, they do not fully prevent fouling process. Moreover, these strategies usually target against a specific spices of biofilm but fail to inhibit growth of other types [46]. A generalized strategy that removes all types of biofouling material is more appealing. This is particularly true for hydrocephalus shunt because both microscopic and macroscopic biomaterials can lead to occlusion.

1.4 Active Anti-fouling Strategires

While passive anti-biofouling surfaces may decrease the rate of biofilm accumulation, they do not eliminate bio-accumulation entirely. Thus, active anti-biofouling approaches that periodically remove, reduce or dislodge a biofilm on demand is more appealing, especially for chronically implanted devices. With the advancement in

micro and nano fabrication and miniaturization of transducers, active strategies became possible and gained interests among academic researchers. Existing strategies utilize actuators to deliver electrical or mechanical energy locally upon request for biofilm detachment and disruption. Strategies targeting generic biofilms, fouling in cardiovascular, ophthalmological and dental diseases were designed and reported.

Ultrasound has been long identified as an assistive method to treat deep vein thrombosis [88–90]. For instance, Kim et al, designed PZT based micro-ultrasonic transducer to reduce blood clot in size from directional mechanical wave [91]. The device was less than 1.5 mm in diameter and could be potentially integrated into a catheter for vein access. As much as 40% clot mass reduction was achieved with additional microbubble-assisted cavitation in vitro. The device showed mechanical disintegration of clot even without delivery of typical thermolytic drug at an implantable footprint.

Pepakayala et al [92], designed a magnetoelastic microstructure to address glaucoma drainage device (GDD) failure from obstruction. GDD is a small tubular structure (typically less than 500 microns in diameter) that drains excessive aqueous humor out of eye ball to regulate intraocular pressure for glaucoma patients [93]. However, it is prone to fouling from collagen and fibroblast buildup. This magnetoelastic resonant device was micro-machined from Fe40Ni38Mo4B18, a magnetoelastic alloy that shrinks or expands microscopically under magnetic field. The device vibrates up to 1.5 μm under a static bias and a time varying magnetic field. The structure was mounted at exit of GDD tubbing and a flow up to 266 μm/s was induced to address fouling. However, no anti-fouling result was reported in vivo or in vitro so far.

Hwang, et al [94] proposed a biofilm removal technique using catalytic antimicrobial robots that combined molded helical propeller with magnetic nanoparticles. They suggested that iron oxide nanoparticles can catalyze hydrogen peroxide and release free radicals which eradicates bacteria chemically and breaks down exopolysaccharide (EPS) matrix. They demonstrated S. mutans films removal from inner lumen of a glass tubing (7 mm diameter) by rotating and propelling the robot through the path

magnetically. The robot may be useful for accessing confined space like inside of human teeth and catheters, however, imaging guidance and multi-coil magnetic field generating system are required to navigate the robot, which complicates the use in patients.

Wang, et al. designed a configurable surface that combined ferrofluid on top of micro-channels [95]. The surface changes its physical geometry and flow pattern under external magnetic field to manipulate friction, adhesion properties and water droplet interaction. At large field strength, macro scale protuberance was utilized to rupture and remove green algae. However, the surface requires ferrofluid on top and may not be suitable for implantable applications.

Electric field has also been explored as an active anti-fouling source. For instance, Yeh, et at. demonstrated nano-molecule desorption on PZT membrane by vibration assisted electric field [96]. They indicated that electrostatic potential produced by PZT can overcome binding energy (Van der Waals and hydrophobic effect) between proteins and substrate underneath to cause detachment. As much as 50% bovine serum proteins was removed from titanium surface from actuation.

These active strategies provide excellent insight on how biofilm can removed by localized energy delivery. However, none of the techniques can be easily adapted to prevent hydrocephalus shunt obstruction non-invasively. For ultrasonic transducers, a voltage delivery requires a separate implantable battery or sophisticated energy delivery system, which raises question of battery compatibility risk. For magnetic propeller, the magnetic spatial gradient required for adequate force may be challenging to achieve. This is particularly difficult for penetrating deep brain space because the gradient dissipates as $\frac{1}{R^3}$, with R being distance from coil to target. A satisfying active anti-fouling strategy should not only address a wide variety of biofilm materials on demand but also tailored for the location and architecture of hydrocephalus shunt.

1.5 Magnetic Actuators for Hydrocephalus Shunt Obstruction Prevention

To address hydrocephalus shunt failure problem, especially biofilm related obstruction at fluid intake pore of ventricular catheter, magnetic micro-actuator was proposed to actively prevent or remove occlusion mechanically by shear generation [97–100]. The micro-electromechanical system (MEMS) structure consists of a pair of anchored torsional beams or a single cantilever. A structural plate with ferromagnetic or permeant magnet material is attached at end of beams. Under the presence of magnetic field, the structure experiences mechanical torque to deflect out of plane as illustrated in Fig. 1.6. The structure was indented to sit at pores of ventricular catheter to remove biofilm by in-and-out of plane motion under alternating magnetic field. This device is advantageous because it can be operated wirelessly and is battery-free.

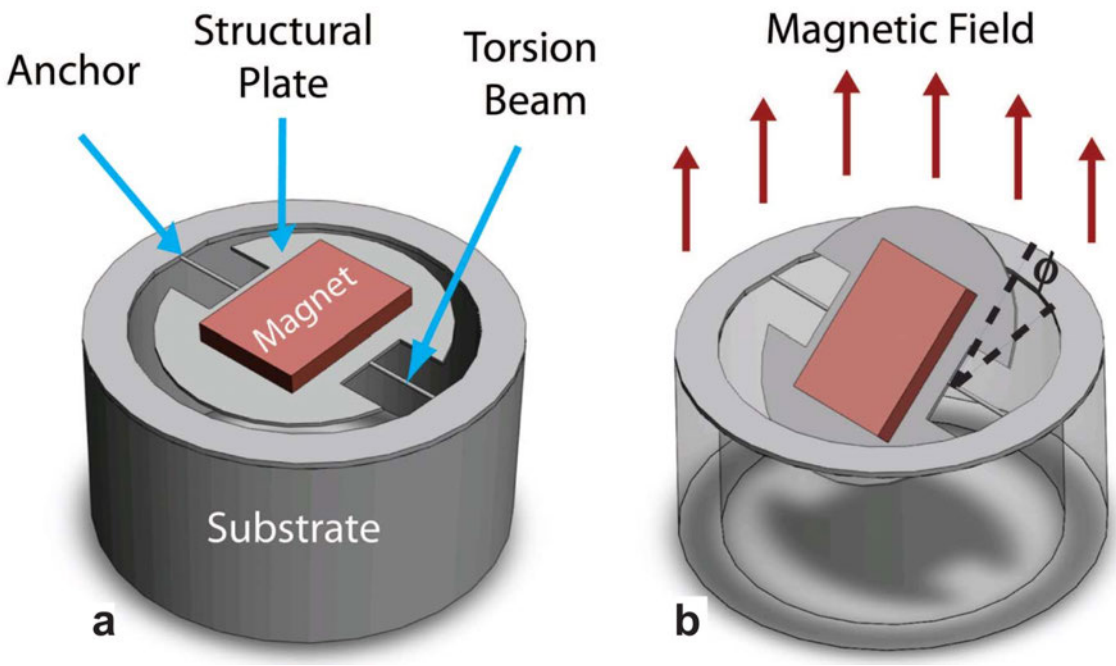

Fig. 1.6. (a) Torsional magnetic actuator at rest. (b) Actuator rotate out of plane under the presence of magnetic field. Image reprinted from [100] with permission.

Magnetic actuator of this kind was first reported by Judy. et al in 1995 [101]. It was fabricated using a batch process that combined electroplating with conventional IC-lithography, materials and equipment. The cantilever material was made from polysilicon. Nickel iron alloy (Ni80Fe20) was electroplated as magnetic material. A large displacement (1.2 mm) and rotation angle (over 180 degrees) was achieved. Later, a torsional actuated structure was designed and fabricated with an on-chip planar actuation coil [102] Judy. et al, primarily focused on proof-of-concept, fabrication technics and mathematical modeling of deflection behaviors in their original reports. Micro-mirrors, micro-grippers and optical switches were potential applications for magnetic actuators at the time [101–103].

In 2006, Lee. et al, first demonstrated a design of magnetic actuator intended for cell removal at ventricular catheter intake pore [104]. An array of torsional device was fabricated from silicon nitride (SixNy) beams with rectangular Nickel ferromagnetic element. The structural plate has round edges contour closely to shape of circular opening. The moveable structural plate was enclosed by silicon substrate with a small gap in between (5 - 80 microns), resembling a cylindrical pore. The study focused on cell detachment and removal in vitro. They indicated that as much as 50% of pre-coated muscle cell was removed off from actuator surface by actuation. In addition, device resonant behavior and mechanical fatigue performance were reported in 2011 [97].

Later, Lee. et al examined magnetic resonant imaging (MRI) compatibility of torsional magnetic actuator [100]. Under exposure to strong static (7 T) and radio frequency (RF) magnetic field from a 7-Tesla MR system, the structural integrity of magnetic actuator remained unaffected. Static and dynamic response showed insignificant difference before and after experiencing MRI operation. The result also showed minimal increase in RF heating (1.6 °C). However, imaging artifact was detected because of high susceptibility of ferromagnetic nickel.

Next, Lee et al, proposed and fabricated magnetic actuator with bimorph cantilever that bends naturally downward at resting state to allow better fluid pas-

sage[237]. The resting flexural bent was produced from stress between two layers of silicon nitride deposited using low pressure chemical vapor deposition (LPCVD) and plasma enhanced chemical vapor deposition (PECVD) sequentially. Lee et al examined mechanical behaviors of the device, including post release bending angle, static and dynamic responses. Finally, microbeads removal clearance capability was demonstrated through a circulatory setup. Shear stress generated from liquid-actuator interaction was identified as the main mechanism of debris removal. Jet impingement tests and 2D finite element analysis [97] were conducted to support the claim.

Thus far, magnetic actuators were designed for intake pore on ventricular catheter. However, detachment of cells and microbeads were only examined on wafer level. An integration of magnetic actuator into catheter had yet to achieve. Silicone catheter is soft and compliant as compared to brittle silicon chip. The inherent mechanical mismatch makes it difficult to integrate the existing design into a polymer tubbing. Therefore, it is necessary to develop a secure attachment between magnetic actuator and catheter to further investigate the functionality of magnetic actuator in vivo.

1.6 Scope of Study

The objective of this study is to advance the development of magnetic micro actuator to increase reliability and extend lifetime of hydrocephalus shunt. More specifically the primary goal is to: 1) Develop a device integration strategy for a 'smart catheter' featuring magnetic actuators in situ; 2) Create a new generation of devices that address tissue level fouling *in vivo*. In order to achieve the goal, the primary strategy was fabricating the actuator using a flexible polymer substrate, allowing a precise and secure attachment to the contour of catheter.

In Chapter 2, I will discuss the development of novel fabrication process for polyimide based implantable magnetic micro-actuator. An adaption from a published journal article [105] is presented. Device integration, mechanical behaviors, protein and bacteria clearance evaluations were accomplished. Chapter 3 features an adap-

tation from a published journal article [106]. Metallic strain gauge material was integrated to detect strain on cantilever produced from actuation. Optimal alignment between external magnetic field and actuator can be achieved through resistive readout. In Chapter 4, a new actuator geometry was proposed to improve deflection and torque for prevention of blood clot obstruction in vitro. Occlusion from tissue level blood clot was significantly reduced in a dynamic in vitro setup. Next, an in vivo evaluation of smart hydrocephalus shunt with integrated magnetic actuators was presented. An intraventricular hemorrhage porcine model was used to enlarge ventricle. Improved shunt survival outcome was observed by magnetic actuation. Chapter 5 concludes this dissertation with closing remarks on device limitation and future research direction.

2. FABRICATION AND FUNCTIONAL EVALUATION OF POLYIMIDE BASED MAGNETIC ACTUATORS

Biofouling is a serious issue with enormous implications for devices used in biomedical, maritime, and environmental applications [107]. For devices that chronically interface with the body, biofouling can have a detrimental impact on device performance [108]. Implantable devices such as catheters and biosensors, often suffer from catastrophic functional degradation over the course of their lifetime due to biofouling [109]. An example of biofouling related failure that can lead to critical injury for patients can be found in shunt systems used for hydrocephalus. Hydrocephalus is a neurological disorder that is characterized by an abnormal accumulation of cerebrospinal fluid (CSF) in the brain, often due to an imbalance between the generation and absorption of CSF. It is commonly diagnosed in children with approximately 1-2 newborns diagnosed for every 1000 in the United States [110, 111]. Unfortunately, there is no cure for this debilitating disease. The gold standard for the treatment of hydrocephalus is the implantation of a shunt system to divert excess CSF from the brain to another part of the body [112]. As such, a sudden failure in this important device can lead to significant and rapid health decline for the patient. Unfortunately, shunt systems are notorious for their extremely high failure rate of more than 40% within 1 year and up to 85% within 10 years of implantation [14, 15]. A large portion of this high failure rate can be attributed to biofouling-related obstruction and infection [14, 21].

A significant amount of research effort has been devoted to mitigating such biofouling-related device failures by preventing and minimizing the attachment of biomolecules onto a surface of interest. Most anti-biofouling strategies can be classified as either passive or active methods. The passive approaches aim to prevent biofilm accumulation by creating a 'stealth surface', which ideally remains undetected in a biological milieu and therefore is not prone to biofouling [113]. Typically, these anti-biofouling

surfaces are created using polymer coatings to decrease the interfacial energy between the surface with the surrounding solution or to reduce the intermolecular forces between the surface and the biomolecules [113]. Examples of anti-biofouling polymers include polyethylene glycol (PEG) terminated polymers [64, 65], perfluoropolyether-based random terpolymers [66], zwitterionic polymers [67,68] and phosphazene polymers [69]. More recently, biomimetic micro and nanoscale patterns have also been explored to prevent biofouling. Pogodin et al., demonstrated the antimicrobial properties of nanopillar structures found on the wings of a Cicada [86]. Moreover, Chung et al., recently engineered micro-topography found on shark skin that were shown to disrupt biofilm formation [114].

While passive anti-biofouling surfaces may decrease the rate of biofilm accumulation, they do not eliminate bio-accumulation entirely. Thus, active anti-biofouling approaches that can periodically remove, reduce or dislodge a biofilm on demand remain more attractive, especially for chronic applications (e.g., implantable devices, marine sensors, etc.). Several different electro-mechanical transducers have already been proposed for anti-biofouling applications including electrostatic repulsion, electroosmotic forces, and ultrasound-induced shear forces to combat against proteins [96], bacteria [115], and even blood clots [91]. Although these active methods demonstrate exciting potential for combating biofouling, they pose challenges for chronically implantable devices because of their complexity and high power requirements.

To combat biofouling *in situ* without the morbidity, mortality, and expense of additional surgical intervention, we have previously proposed to use microfabricated magnetic actuators for removing bio-accumulation on ventricular catheters [98]. A magnetic microactuator is ideal for such applications due to its simplicity (i.e., they do not require integrated circuits or power source). Although the cellular removal capabilities [98], durability [99], and magnetic resonance imaging compatibility [100] of these devices have been demonstrated, they have only been fabricated on a rigid silicon substrate thus far, which complicates their integration into flexible devices. To facilitate the integration of microfabricated devices into silicone-based catheters, we

designed, fabricated, and tested novel thin-film polymer-based magnetic microactuators in an effort to create a self-clearing smart catheter. In this work, we demonstrate the new process flow to create polyimide-based magnetic microactuators and integrated them into silicone-based implantable catheter for future *in vivo* evaluations. We report static and dynamic mechanical responses of these devices, and evaluate their bacteria clearing capabilities. The mechanical stability of these device is also examined. To demonstrate anti-biofouling properties of these thin-film-based magnetic microactuators, we evaluated the impact of actuation using fluorescent protein and bacteria.

2.1 Design

2.1.1 Material and Device Structure

Our thin film devices use a single cantilever beam structure. The structural plate is patterned out of a uniform polyimide layer as illustrated in Fig. 2.1. Polyimide is chosen as the structural material because of its excellent chemical resistance, biocompatibility, compatibility with MEMS process and good mechanical properties [116]. The microdevice features the same design previously reported in [99]. At the tip of the cantilever beam, an electroplated nickel magnet covers the surface of a circular structural plate. The diameter of the structural plate is chosen to be 900 μm, which is slightly smaller than the pore size of a ventricular catheter. In the presence of a magnetic field, the magnetic element can apply a moment on the flexure to cause out-of-plane deflection. The large amplitude out-of-plane deflection produced in this manner is used to mechanically remove biofouling. Assuming that the torsional load on polyimide cantilever is a concentrated on tip, the relationship between the applied magnetic field and the resulting deflection angle can be described by [117], [101]:

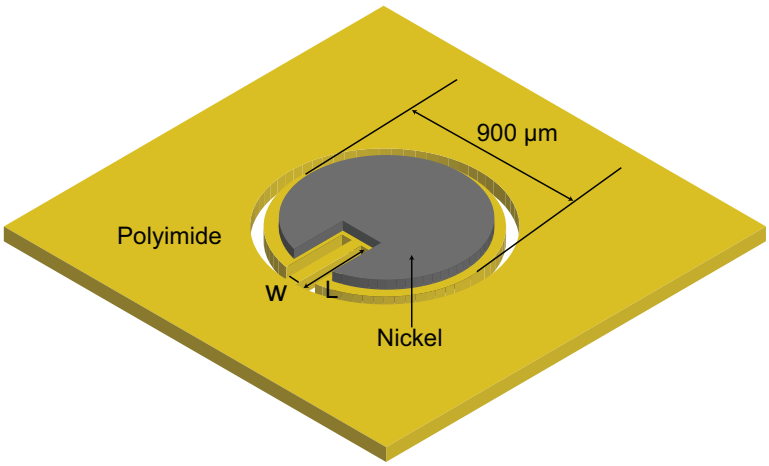

Fig. 2.1. Dimension and structure of polyimide-based magnetic actuator.

$$\Phi = V_m M H \sin\left(\frac{\pi}{2} - \phi\right) / k_{beam} \tag{2.1}$$

$$k_{beam} = EI; I = \frac{wt^3}{12L} \tag{2.2}$$

with beam cantilever beam stiffness k_{beam}, magnet volume V_m, magnetization M, applied magnetic field H, modulous of elasticity E, beam width w, beam length L and beam thickness t. We experimentally determined 12 μm as the optimal thickness for reasonable stiffness and overall structural strength. With the fixed thickness, we varied the cantilever beam length (250-500 μm) and width (40-55 μm) to optimize device performance as shown in Table 2.1.

2.1.2 Dynamic Response Theory

To evaluate dynamic behavior, our magnetic microactuator was modeled as a cantilever–tip mass system. The resonant frequency can be approximated by solving the natural modes of free vibration. According to Euler-Bernoulli theory [118], free transverse vibration of a thin uniform cantilever can be described by:

$$\frac{EI}{\rho A}\frac{\partial^4 W(x,t)}{\partial x^4} + \frac{\partial^2 W(x,t)}{\partial t^2} = 0 \tag{2.3}$$

Table 2.1.
Design variation

Device Type	A	B	C	D	E	F
Beam Length [μ**m**]	500	400	400	350	300	250
Beam Width [μ**m**]	55	55	50	50	45	45
Nickel Area [μ**m**^{2}]	418541	440341	438911	448911	458711	468911

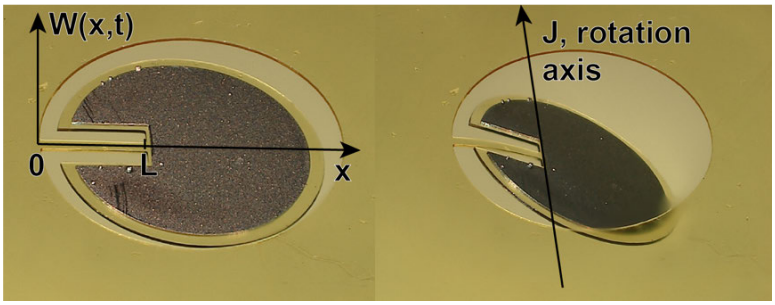

Fig. 2.2. An illustration of coordinate system defined for the calculation of natural resonant frequencies.

where $W(x,t)$ is vertical deflection amplitude as a function of length and time t, at position x along length of the beam. A, I, ρ, E, are the cross section area, the second moment of inertia, density, and the Young's modulus of beam, respectively. The natural vibration frequency $\omega = 2\pi f$ can be solved by applying proper boundary conditions to $W(x,t)$. In our case, the cantilever is fixed at base at all time, therefore:

$$W(0,t) = 0; \frac{dW(0,t)}{dx} = 0 \tag{2.4}$$

On the other end of cantilever ($x = L$), the shear force must match with the tip mass m:

$$EI\frac{\partial^3 W(L,t)}{\partial x^3} = m\frac{\partial^2 W(L,t)}{\partial t^2} \tag{2.5}$$

Tip mass m is defined as the mass of structural plate plus the nickel on top. The bending moment at $x = L$ must also match with the moment of inertia of tip mass J:

$$EI\frac{\partial^2 W(L,t)}{\partial x^2} = -J\frac{\partial^3 W(L,t)}{\partial x \partial t^2} \tag{2.6}$$

The moment of inertia J is calculated from the geometry of structural plate as illustrated in Fig. 2.3. The primary flexural resonant frequency is solved for numerically after applying boundary conditions (2.4), (2.5), (2.6) to equation (2.3). Assume $W(x,t)$ can be separated by a function of time and a function of space:

$$W(x,t) = W(x)T(t); \tag{2.7}$$

$$W(x) = Ce^{sx} \tag{2.8}$$

$$T(t) = A_1 cos\omega t + B_1 sin\omega t \tag{2.9}$$

By separation of variable:

$$\frac{d^4 W(x)}{dx^4} - \frac{\rho A\omega^2}{EI}W(x) = 0 \tag{2.10}$$

$$\frac{d^2 T(t)}{dt^2} + \omega^2 T(t) = 0 \tag{2.11}$$

The general form of solution for $W(x)$ is given by:

$$\begin{aligned} W(x) = {} & C_1(cos\beta x + cosh\beta x) + C_2(cos\beta x - cosh\beta x) \\ & + C_3(sin\beta x + sinh\beta x) + C_4(sin\beta x - sinh\beta x) \end{aligned} \tag{2.12}$$

where:

$$\beta^4 = \frac{\rho A\omega^2}{EI}; \omega = \beta^2\sqrt{\frac{EI}{\rho A}} \tag{2.13}$$

After applying boundary conditions the final equation to solve has the form:

$$\begin{aligned} & -2\beta^5(EI)^2[\rho^2 L^4 A^2 - x^4 mJ + cosh(\beta L)cos(\beta L)\rho^2 L^4 A^2 \\ & + cosh(\beta L)cos(\beta L)\beta^4 L^4 mJ + sinh(\beta L)cos(\beta L)\rho L^4\beta^3 JA \\ & + sin(\beta L)cosh(\beta L)\rho L^4\beta^3 JA + sinh(\beta L)cos(\beta L)\rho L^4\beta mA \\ & - sin(\beta L)cosh(\beta L)\rho L^4\beta mA)]/(\rho^2 L^9 A^2) = 0 \end{aligned} \tag{2.14}$$

Natural resonant frequency is the only unknown. A Matlab script was written to calculate the primary flexural resonant frequencies (See Appendix).

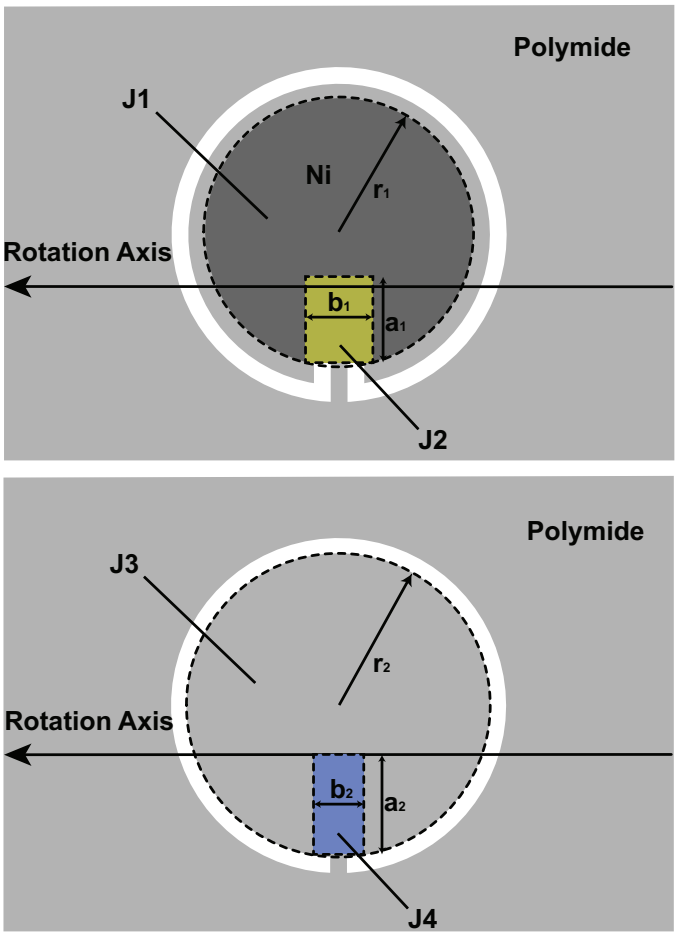

Fig. 2.3. An illustration of moment of inertia calculation from superposition principle. Total moment of inertia J = J1-J2+J3-J4. The figure on top describes mass of structural plate from nickel. J1 is calculated from thin disk of nickel layer enclosed by dotted circle. J2 indicates thin sheet of nickel layer to be subtracted as indicated by dotted rectangular boundary. The figure on bottom describes mass of structural plate from polyimide. J3 is calculated from thin disk of polyimide layer enclosed by dotted circle. J4 indicates thin sheet of polyimide to be subtracted as indicated by dotted rectangular boundary.

2.2 Fabrication

Fig. 2.4 illustrates the overall process flow. Starting from a single side polished 100 mm silicon wafer (Silicon Quest, San Jose, CA), 500 nm of silicon dioxide (SiO2) was

first deposited as a release layer using Plasma Enhanced Chemical Vapor Deposition (Axic, Milpitas, CA). On top of the oxide layer, polyimide (PI-2525, HD Microsystem, Parlin, NJ) was spin coated at 1500 rpm and soft baked on hotplate (130 °C and 150 °C successively for 30 s each). An adhesion promoter (VM652, HD Microsystem, Parlin, NJ) was then used before the application of polyimide to ensure good adhesion. The sample was then cured with a nitrogen oven using the manufacturer specified heating sequence.

Next, a 20 nm chromium adhesion layer and 50 nm gold conduction layer were deposited using an electron beam evaporator (Varian). The pattern of the electroplated nickel was defined by 25 μm thick photoresist (AZ9260, Microchemicals, Germany). The nickel ferromagnetic element was electroplated in 2 L plating solution containing 1 M nickel sulfamate, 0.4 M boric acid, and 10 g sodium dodecyl sulfate at 60 °C. Ten-micron-thick nickel was deposited in 38 min using the current density of 10 mA/cm^2.

The structural plate was defined by oxygen plasma etching in an Advance Oxide Etcher (Surface Technology System, Newport, United Kingdom). An Oxygen and Argon gas mixture (7:1) was used under 600 W RF coil and 20 W platen power. The polyimide thickness was then verified using Alpha-Step IQ surface profiler (KLA-Tencor, Milpitas, CA) after oxygen plasma etching. To release the sample, the wafer was placed in 6:1 buffered oxide etchant (BOE) for approximately 40 hours. After release, 500 nm of Parylene C was conformally coated (PDS2010, Specialty Coating System, Indianapolis, IN) to improve biocompatibility.

2.3 Mechanical Evaluation

2.3.1 Static Response

To characterize the static mechanical response of fabricated magnetic microactuator, the angular deflection as a function of applied magnetic field strength was measured for each device. The magnetic field was generated by a custom made iron core electromagnet magnet. The magnetic field strength was measured using a gauss-

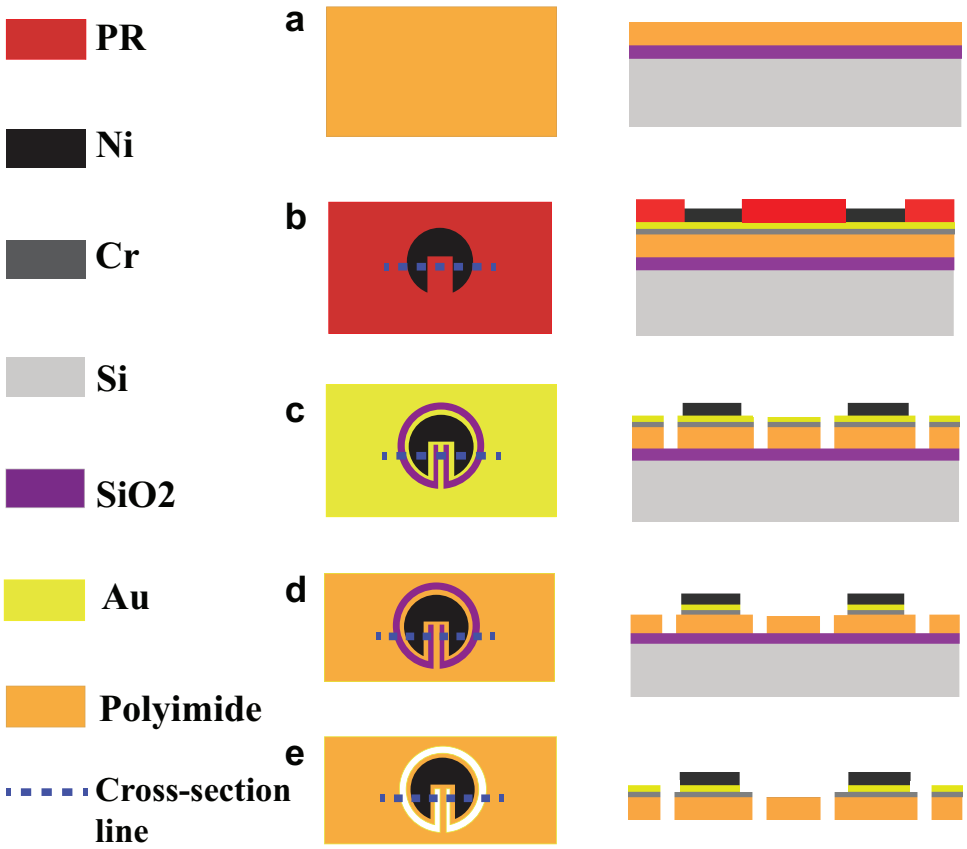

Fig. 2.4. Fabrication sequence of a polyimie-based magnetic microactuator. (a) Deposition of 500 nm SiO 2 followed by 12 μm polyimide. (b) Evaporation of Cr/Au followed by Ni electroplating. (c) Definition of structural plate patterning. (d) Removal of Cr/Au. (e) Release of the thin-film magnetic microactuator.

meter (8010 Gauss/Telsameter, Pacific Scientific, Chandler, AZ) as a function of applied current. The individual device structure was aligned and gently placed on a 5 mm thick PDMS mold with 2 mm diameter through-holes for structural support as shown in Fig. 2.6a. PDMS was then placed on top of the electromagnet under a digital microscope (KH8700, Hirox, Hackensack, NJ). The top edge of nickel magnet and the base of the cantilever, shown in Fig. 2.6b, were focused and their vertical positions were recorded. The difference between two points was then converted into deflection angle using device geometry as illustrated in Fig. 2.6c. The vertical length

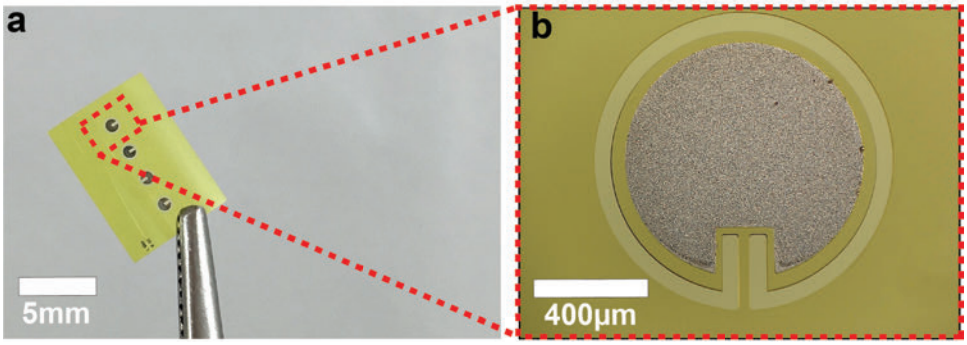

Fig. 2.5. (a) Photograph of an array of 5 devices. (b) microscopic image of a single device (Type D, top view).

Z was directly recorded by the microscope at deflection. The angle conversion is given by trigonometry:

$$sin(\phi) = \frac{Z}{\frac{L_1}{\phi tan(\frac{\pi-\phi}{2})} + L_2} \tag{2.15}$$

The deflection angle ϕ can be solved numerically. Results obtained from each device type is presented in Fig. 2.7. Our results indicate that approximately 15–25 KA/m of magnetic field strength can give us fairly large deflections (>45 degrees), and this will serve as a general guide to what magnetic field strength we need to use to actuate the device *in vivo*.

2.3.2 Dynamic Response

The dynamic responses of the polyimide-based magnetic microactuators were measured in air and in deionized water to identify the resonant frequency at which the device actuates with high energy efficiency. An electromagnet with a 6-inch-long ferrite 77 core (Fair-Rite, Wallkill, NY) was made for measuring the dynamic responses because of its high relative permeability and excellent frequency response. The test sample was placed on a PDMS fixture on top of the electromagnet in the same manner as with the DC measurements. A scanning laser Doppler vibrometer (MSA-400, Poly-

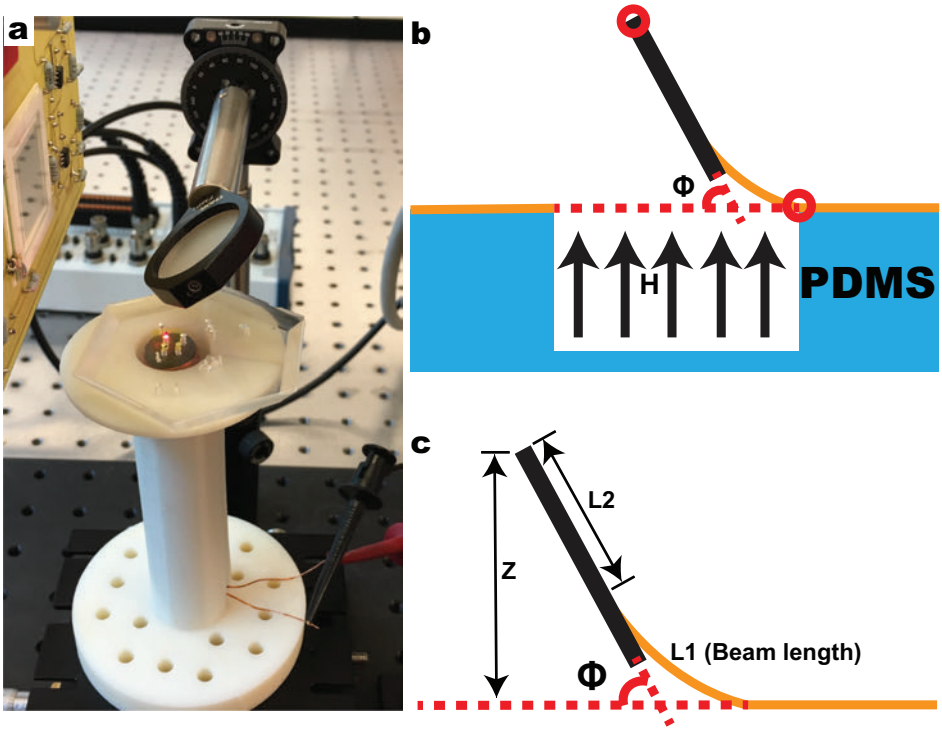

Fig. 2.6. Schematic and definitions for static deflection measurements. (a) A photograph of PDMS testing structure on top of the bespoke electromagnet. (b) Schematic of bench-top mechanical evaluation setup, which allows large out-of-plane deflection ϕ in applied magnetic field. (c) Definition of geometric measurements made for static response.

tec, Waldbronn, Germany) was used to measure the out-of-plane velocity at a series of points across the actuator surface (Fig. 2.10). The electromagnet was driven with a swept sine excitation generated by the MSA-400 system. The fast Fourier transform algorithm was applied to the time series velocity data, and frequency-domain integration was used to develop a spatially averaged displacement spectrum for the device (Fig. 2.11).

A linear approximation of the impedance of the magnet was used to estimate the current applied. The H1 frequency response estimator (amplitude per unit actuation current) was then calculated, giving the best linear estimate of the relation between current and displacement from 1.25 to 1200 Hz with a 1.25 Hz resolution. A plot of the

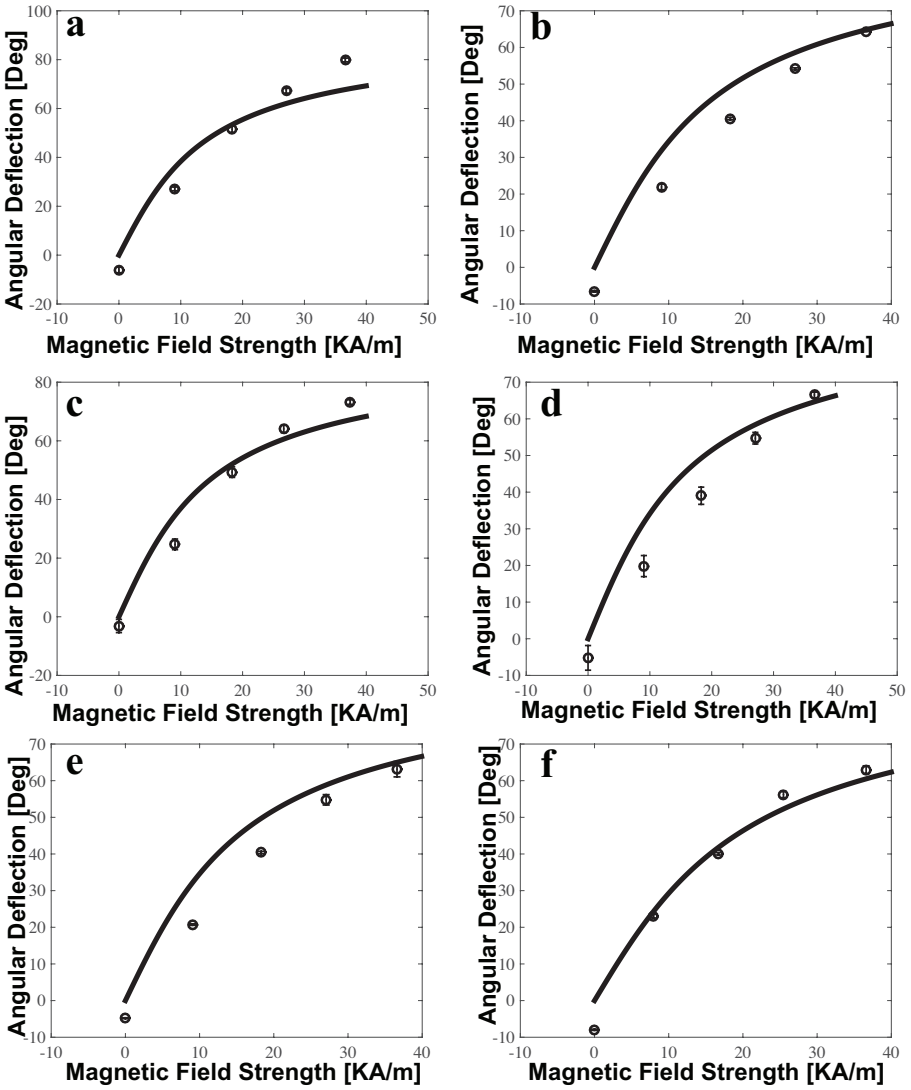

Fig. 2.7. Static angular deflection. Solid line indicates theoretical prediction, circle represents measured values, a-f correspond to designs A through F. The results ($n = 2$) are expressed as average $\pm$ s.d. The theoretical calculations were made based on nickel thickness = 10μm, polyimide thickness = 12μm and a saturated Ni magnetization = 0.6T.

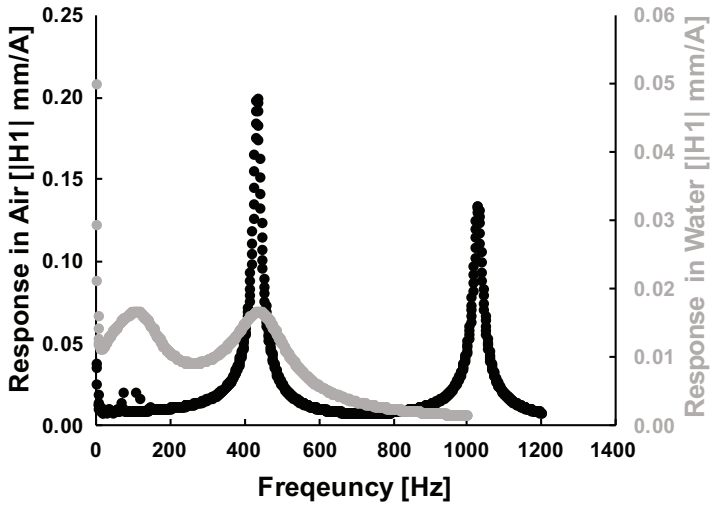

Fig. 2.8. H1 frequency response estimators of a representative magnetic microactuator (Type B) in air and in water. Black dots and axis represent data in air, grey dots and axis represents data in deionized water.

magnitude of the H1 frequency response estimator is shown in Fig. 2.8. The frequency at which the peak amplitude occurred in air was recorded. Theoretical prediction and measurement of primary resonant frequencies for 3 sample devices (Type B) are compared in Table 2.2. The discrepancy between observed resonant frequency in air and theoretical prediction is most likely from nickel thickness variation due to electroplating.

2.3.3 Mechanical Fatigue

It is important to ensure that the polymer-based the micro actuator is strong enough to survive extended cycles of actuation. We examined its mechanical fatigue property by continuous actuation for 300 million cycles. This translates to 30 minutes of actuation every week for 30 years. Physical appearance and resonant frequencies of the devices were compared before and after actuation.

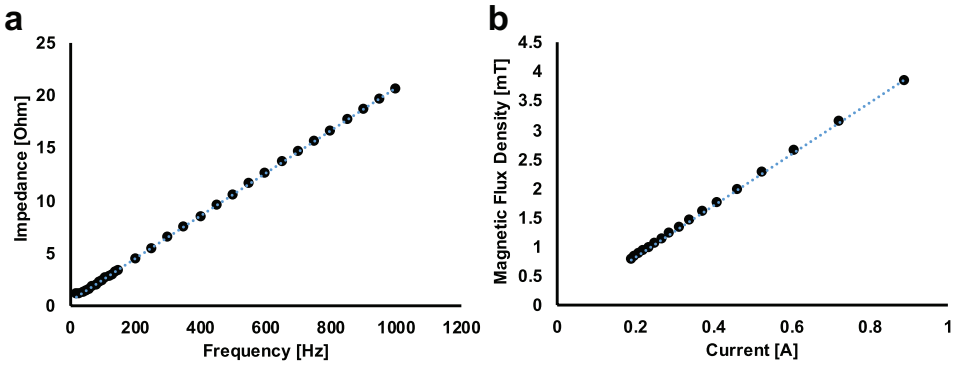

Fig. 2.9. Characterization of electromagnet used for dynamic response. (a) Impedance as a function of excitation frequency. (b) Magnetic flux density produced at location of actuator as a function of supplied current.

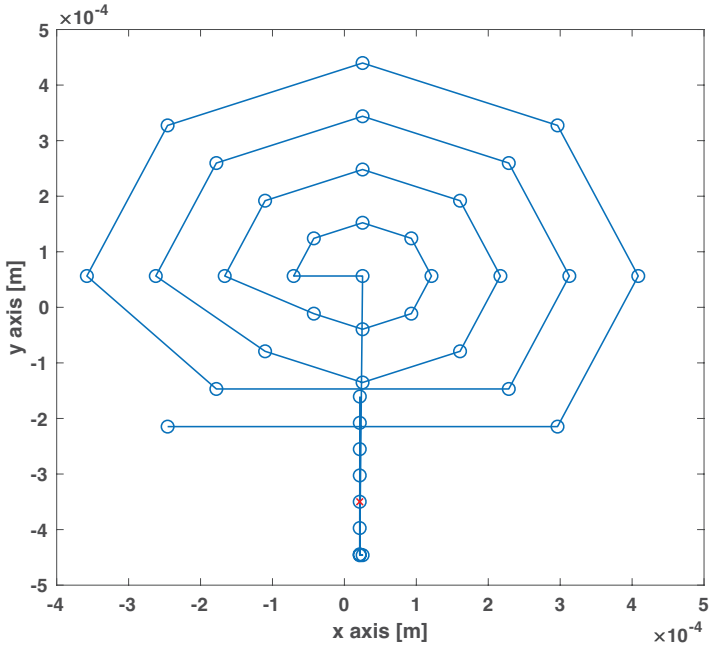

Fig. 2.10. An example of laser projection mapping on an actuator surface. Circle indicates laser position.

Total of 3 actuators (Type B, C, D) in a sheet of polyimide substrate were tested. They are suspended on top of two thin PDMS anchor points covalently bonded on a glass slide. This configuration allows actuator to deflect up or down during actuation.

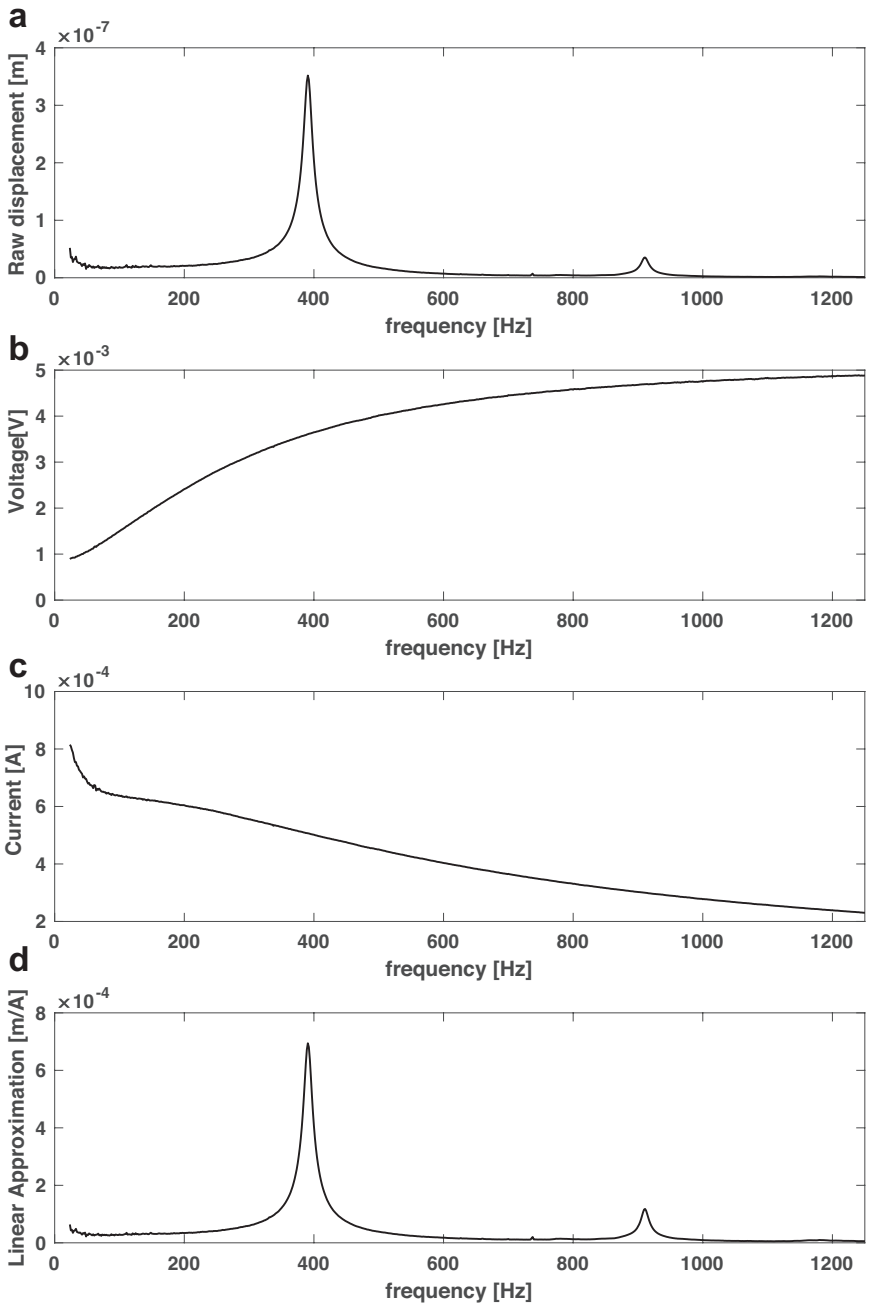

Fig. 2.11. (a) Spatially averaged raw displacement. (b) Voltage supplied to the electromagnet. (c) Calculated AC current supplied to the electromagnet. (d) Calculated vertical spatially averaged displacement from actuator surface per unit current supplied.

Table 2.2.
Expected vs. measured resonant frequency ($n = 3$)

	Theory	*Measured*	Δ*[%]*
Beam length [μm]	400	409.98 $\pm$0.75	2.49
Beam width [μm]	49	48.90 $\pm$0.95	-0.20
Tip mass [Kg]	4.57×10^{-8}	4.54×10^{-8} $\pm3.62\times10^{-10}$	-0.65
J Calculated [Kg·m^2]	2.54×10^{-15}	2.52×10^{-15} $\pm2.02\times10^{-17}$	-0.78
f [Hz]	464.93	449.13$\pm$7.94	-3.39

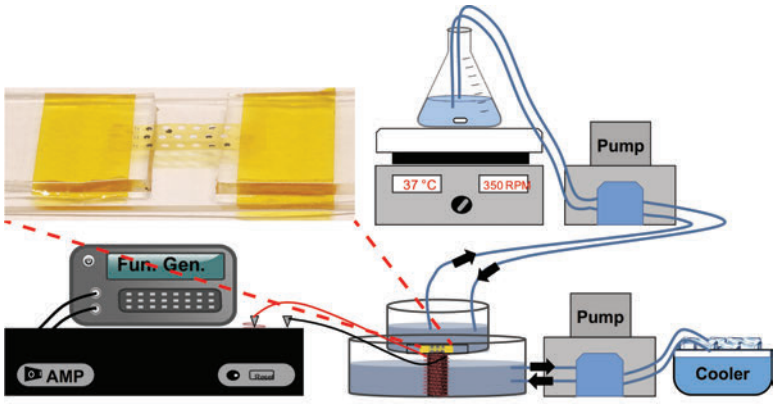

Fig. 2.12. Schematic of the mechanical fatigue setup and a photograph of the array of devices tested.

The glass slide along with five devices were put in a small beaker filled with 1X PBS solution. Temperature of PBS was maintained at 37 °C by circulating solution between a flask sitting on top of a hotplate and small beaker via a peristaltic pump (Cole-Parmer). The actuators were driven by a the same electromagnet used in static response. The magnet sat below the small beaker and was aligned to devices. Actuation current was supplied from an amplifier driven by a function generator set at 100 Hz sine wave. The magnet was water cooled in a large beaker. Ice water was

circulating between the larger beaker and a cooler via the multichannel peristaltic pump.

Three devices were periodically taken out of the testing setup at 300 thousand, 3 million, 30 million, 150 million and 300 million cycles and tested for resonant frequency in air under LDV. The results are concluded below in Fig. 2.13. At the end of 300 million cycles all 3 devices maintained good attachment to substrate. Polymer geometry did not swell or shrink and there were no visible cracks or dents on cantilevers.

The resonant frequency shifts at the end of 300 million cycles compared to initial 0 cycles were less than 5%. (Fig. 2.13a). A comparison between frequency response mode shapes from 0 cycles and 300 million cycles is shown in Fig. 2.13b (Type D). Most of the shift can be attributed by mass building on the device from salt formation when device was dried up from PBS, as can be seen in Fig. 2.13c.

2.4 Functional Evaluation

2.4.1 Protein Removal

To characterize the protein-based biofouling removal capability of polyimide-based thin-film magnetic microactuators, we coated our devices using fluorescent-tagged bovine serum proteins (BSA-FITC, ThermoFisher Scientific, Waltham, MA, USA). The shear stress required to remove BSA has previously been reported to be in the order of 1-10 dyn/cm^2 [119, 120]. Previous finite element simulation indicates that magnetic actuator with similar geometry can generates a surface shear stress over 100 dyn/cm^2 at 30 degrees and 10 Hz [97]. As such, we expected our microactuators to have little trouble in removing the adsorbed BSA-FITC. The fluorescence intensity of absorbed BSA-FITC plateaued around 5 mg/ml on Parylene surface, therefore, all BSA-FITC evaluations used this concentration. Each sample was placed inside a sterile test tube with 5 mg/mL of BSA-FITC in PBS and incubated for 2 h. The images of protein coated samples ($n = 8$) were taken using a fluorescence microscope

(Axio Observer Z1, Carl Zeiss Microscopy, LLC) using filter set 17 (excitation, BP 485/20, and emission BP 515-565, Carl Zeiss Microscopy, LLC). Next, we investigated the impact of actuation of our microdevices on adsorbed protein concentration. Four protein-coated microactuators were subjected to 26.5 kA/m of magnetic field at 40 Hz for 5 minutes, and re-imaged. A set of control devices ($n = 4$) was treated with 5 minutes of zero magnetic field. The fluorescence intensity of microactuator surfaces before and after actuation was quantified using imageJ software (version 1.50i). Fig. 2.14 a-d shows fluorescence images of BSA-FITC coated microactuators. Without actuation, little change in fluorescence intensity was observed. However, actuated samples show statistically significant reduction in fluorescence ($p < 0.01$), which suggests robust biofouling removal.

By periodically removing protein coating that occurs following implantation, it may be possible to delay the inflammatory response that can leads to a premature implant failure. Compared to the control devices, the amount of albumin reduction exceed more than 90% with only 5 min of actuation. Indeed, there are several other plasma proteins that can trigger inflammatory response including fibrinogen (340 kDa) and fibronectin (220 kDa) that have different molecular weights than albumin (66.5 kDa). However, the non-specific interaction is mainly affected by the hydrogen bonding as well as the hydrophobic, Van der Waals, electrostatic, and macromolecular forces, and thus more sensitive to the isoelectric points (pI) of each protein [121, 122]. Although additional experiments will be needed, our hypothesis is that these other proteins will feature similar adhesion properties that can be overcome by our microactuators since they all have similar isoelectric points (pI = 5.5 for fibrinogen and fibronectin and pI = 4.7 for albumin) [123–126]. Therefore, we believe our result provides the preliminary evidence to suggest that these self-clearing catheters can not only be used to remove cellular biofouling [98], but may also be used to combat protein ?lm growth that precedes macrophage recruitment.

2.4.2 Bacteria Removal

The device was placed inside a sterile test tube with *Escherichia Coli* in a 5 ml Lysogeny Broth and incubated overnight in a shaker incubator (250 rpm) at 37 °C. Following incubation, the tube was taken out and placed in room temperature for another two hours to facilitate the adhesion of *E.coli* onto the device. Three groups of devices were tested: control, non-actuated, actuated in a cross-sectional comparison. For the control condition, devices were taken from the incubation tube, immediately stained (t = 0) using Live/Dead Bacteria Viability Kit (Thermo Fisher Scientific) and imaged under an inverted fluorescent microscope (Axio Observer Z1, Carl Zeiss). The images were taken at 10X objective under 17-Alexa Fluor 488 reflector (live/green) and a 20-HE Rhodmanie reflector (dead/red). The non-actuated devices were placed in the 1X PBS solution for 20 min without applying magnetic field, then stained with fluorescent dyes, and imaged under the microscope. The actuated devices were subjected to 26.5 KA/m of magnetic field at 100 Hz, then stained and imaged. The time elapsed due to the actuation and imaging was approximately 45 min (Fig. 2.15).

Images were taken and processed using Fiji software (Life-line version) [127]. Fig. 2.16 includes images of the device at each experimental conditions. Intensities of the devices in all conditions were calculated and presented as integrated density for region of interested (Fig. 2.17). We compared the amount of remaining bacteria as evidenced by the integrated density for both live and dead bacteria. There was a large decrease in the amount of live bacteria and increase in the amount of dead bacteria after 45 minutes compared to the control, which indicates progression of bacteria death during the treatment phase of experiments. The actuated devices had even less live bacteria remain on the surface. Interestingly, we also noticed further decrease in dead bacteria after the actuation compared to devices without actuation. These results suggest that our devices may be able to remove both live and dead bacteria from its surface.

2.5 Device Integration

Our device structure was manually slid inside a catheter and aligned to the hole punctured in a central venous access device (Cook Model G0664), which has the inner diameter of ∼1300 μm. The polyimide substrate was rolled to comply with catheter wall curvature and fixed in place without silicone adhesive. We found that the flexible nature of our microfabricated devices facilitates the integration with into an implantable catheter (Fig. 2.18). The manual integration of our single device was relatively simple and straightforward, although we suspect that alignment of an array of device in a multi-pore catheter design may be more challenging. Nevertheless, it may not be necessary to have each inlet pores be integrated with a magnetic microactuator since the biofouling-related occlusion occurs most often on the proximal inlet pores where the flow rate is the highest [18, 52]. Therefore, it may be possible to vary the number and location of devices to optimize catheter performance.

2.6 Conclusions and Discussion

Here we report on the development of polyimide-based thin-film magnetic microactuator, which exhibits great promise for combating biofouling. The flexible nature of the device facilitates the integration with into an implantable catheter as we demonstrated (Fig. 2.18). The manual integration of our single device was relatively simple and straightforward, however, alignment of an array of device in multi-pore catheter design may be more challenging. The mechanical responses of these microfabricated devices showed good agreement with theoretical values, which indicates good control of our fabrication processes. The static deflection of magnetic microactuator mirrored the expected value closely (Fig. 2.7) and the resonant frequency of our microactuators differed on average by less than 4% (Table 2.2).

To mitigate potential device failure due to chronic actuation, we evaluated the shift in resonant frequency following over 300 million cycles of actuation, which corresponds to more than 30 years of lifetime for 30-min of weekly actuation at 100 Hz. The

change in resonant frequency was also relatively minor with the maximum change being approximately 4.3% (Fig. 2.13a). Our post-actuation examination showed that all tested samples showed deposition of salt crystals which could have contributed to the shift in resonant frequency. Overall, the polyimide-based magnetic microactuators were demonstrated to be flexible enough for simple integration into an implantable catheter and were mechanically robust enough to be chronically implanted.

Finally, we have demonstrated the capability of our devices to expel protein layer that adheres to it surface (Fig. 2.14). We have shown previously that our microactuators can reduce the amount of cell grown on our devices [98]. Inflammatory processes often begin with proteinaceous layer formation that triggers recruitment of macrophages [109]. By periodically removing protein coating that occurs following implantation, it may be possible to delay the inflammatory responses that can leads to premature implant failure. Compared to control devices, the amount of protein reduction exceed more than 90% with only 5 minutes of actuation. This result provides preliminary evidence to suggest that these self-clearing catheters can not only be used to remove cellular biofouling materials as previous demonstrated, but may also be used to combat protein film growth.

One potential caveat to our anti-biofouling approach is that it is not clear what happens to the displaced material. Understanding the downstream impact of removed biomaterials will be important in clinical utility of these devices. The ultimate aim of this research is to utilize these smart self-clearing implantable devices to improve the reliability and lifetime of implantable devices by preventing and removing biofouling. The reported results further demonstrate the proof-of-concept of using active mechanisms to combat biofouling in a more physiologically relevant test environment against various biofouling materials. In the future, however, we will evaluate the performance of our devices *in vivo* to demonstrate that our smart catheter can combat biofouling in a more complex environment without adverse effects.

Our magnetically driven wireless actuation system can be easily adapted for real clinical application. For future In-Vivo study, external magnetic field can be generated

by air core multi-turn multiplayer coil with diameter similar to head size of animal of interest. In this way near uniform magnetic field is produced in direction along axis of coil. Strength of magnetic field will be adjusted by varying current supplied. Depending on orientation of catheter placement, the actuation can be achieved by either suspending coil on top of head or putting head inside. To achieve optimal alignment of field and device, we plan to develop and incorporate piezoresistive strain gauge sensor on cantilever for feedback of actuation amplitude. In this study, results from single pore catheter with single device are presented. Area of impact is limited to vicinity of single pore. In future development, multi-device array on multiple pores or on inside catheter lumen will be explored and we expect stronger active biofilm clearance performance. Furthermore, optimization of cantilever geometry and ferromagnetic element will be studied for enhanced range of actuation motion and higher shear stress. One particular approach author would like to explore is combing passive anti-microbial surface, for instance nano-pillar [86], nano-flower [128] or nitric oxide release [83] surface, with active actuation platform for improved biofilm prevention and reduction.

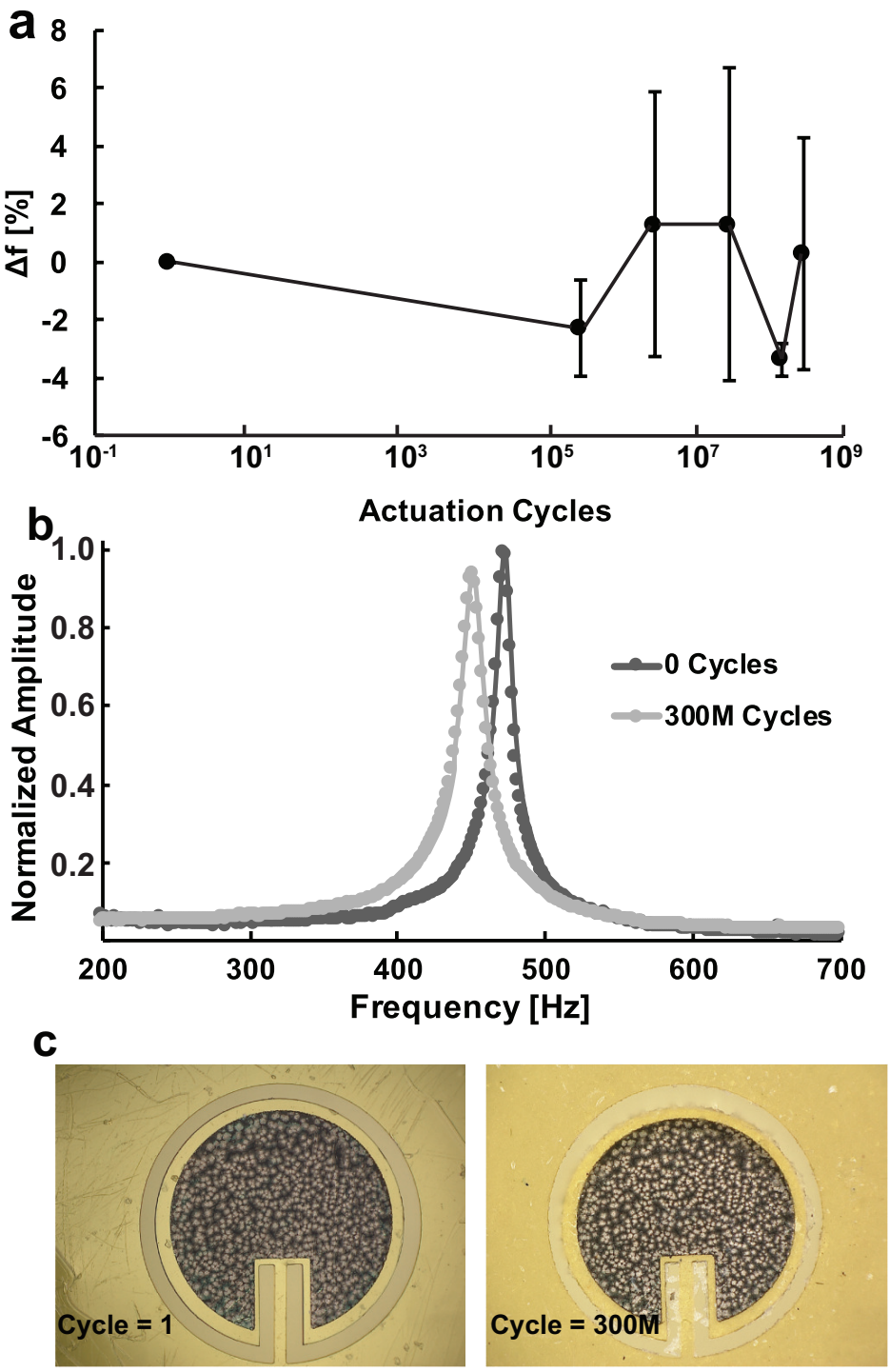

Fig. 2.13. Mechanical fatigue result. (a) Percent change in primary resonant frequency at various actuation cycles. The results ($n = 3$) are expressed as average $\pm$ s.d. (b) Frequency responses of a representative device before and after 300 M actuation cycles. (c) Photographs of a microactuator before and after 300 M actuation cycles. Note the crystalline deposit around the perimeter of the device.

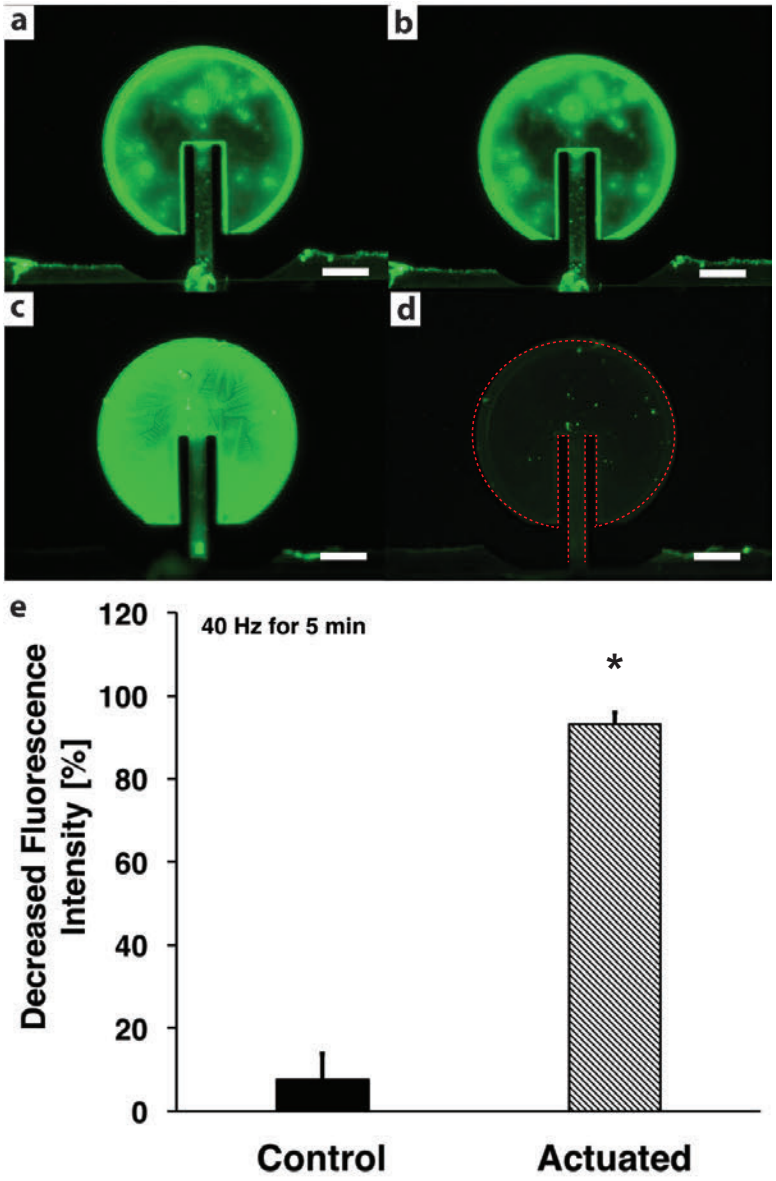

Fig. 2.14. (a-d) Fluorescent images of BSA-FITC coated magnetic microactuators. Scale bar = 200 μm. The control device shows little change before (a) and after (b) treatment. The actuated device shows significant change in fluorescence intensity before (c) and after. (d) application of magnetic field. Red dots outline the actuated device. (e) Plot of fluorescence reduction due to actuation ($n = 4$). Note that the difference in fluorescence reduction between control and actuated devices is statistically significant ($p < 0.01$).

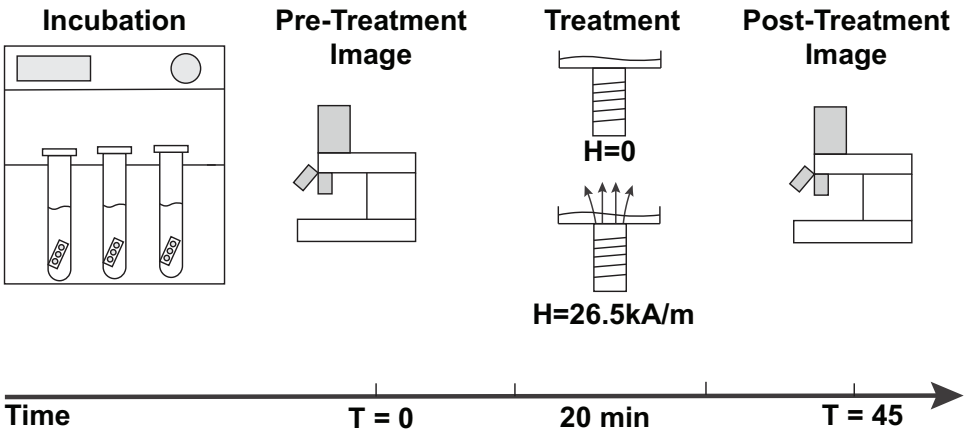

Fig. 2.15. Timeline of bacteria removal experiment.

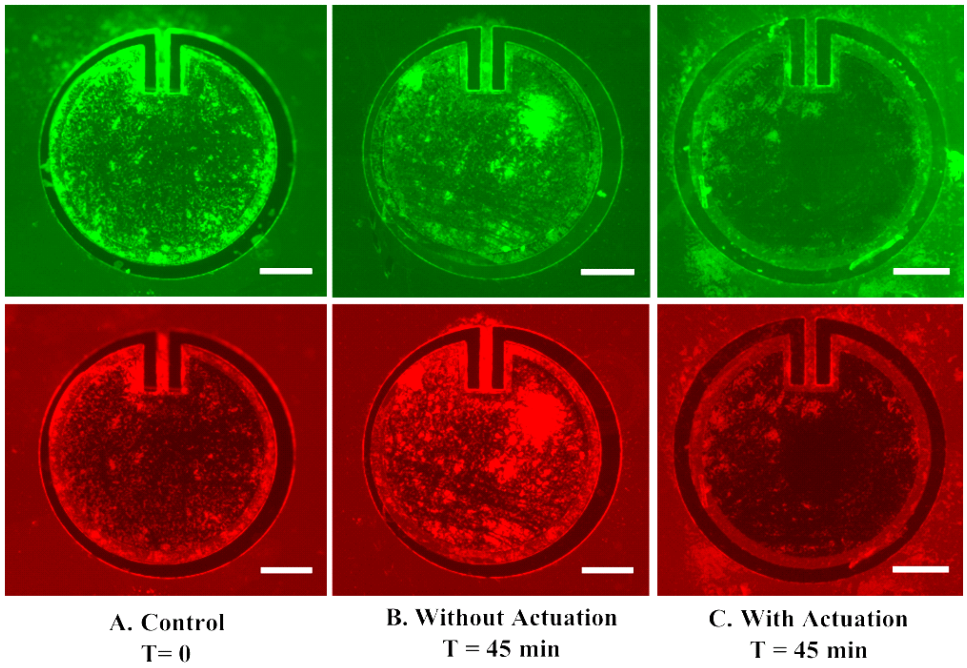

Fig. 2.16. **A.** Initial Bacteria distribution as control at T = 0 min for live and dead bacteria. **B.** Bacteria distribution after 20 min in PBS without actuation at T = 45 min. **C.** Bacteria distribution after 20 min actuation in PBS at T = 45 min. The scale bars = 200 μm.

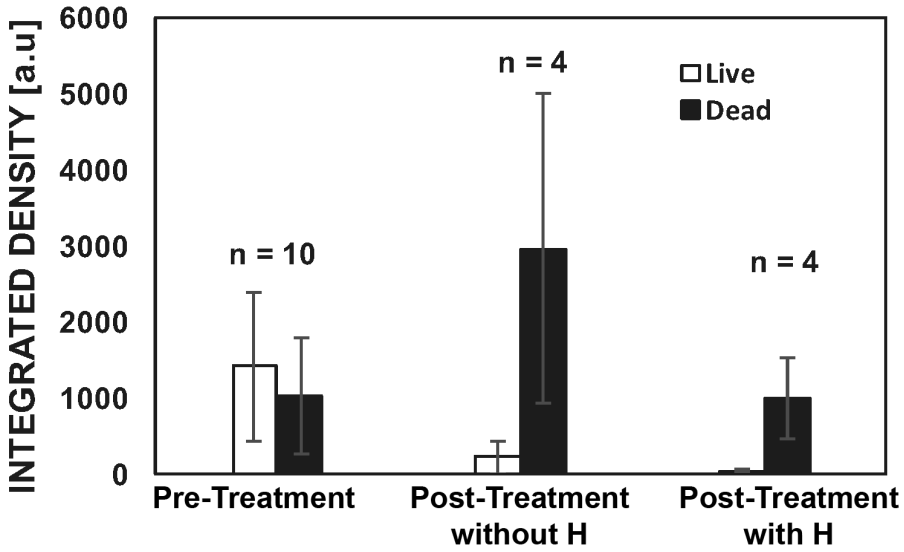

Fig. 2.17. Integrated fluorescent density for live and dead bacteria at various experimental conditions. At T = 45 min, there was a large decrease in the amount of live bacteria and an increase in the amount of dead bacteria compare to the control devices. There was a further decrease in the amount of live bacteria and dead bacteria of the actuated devices compared to the devices without actuation at T = 45 min. The results are represented as mean ± standard deviation.

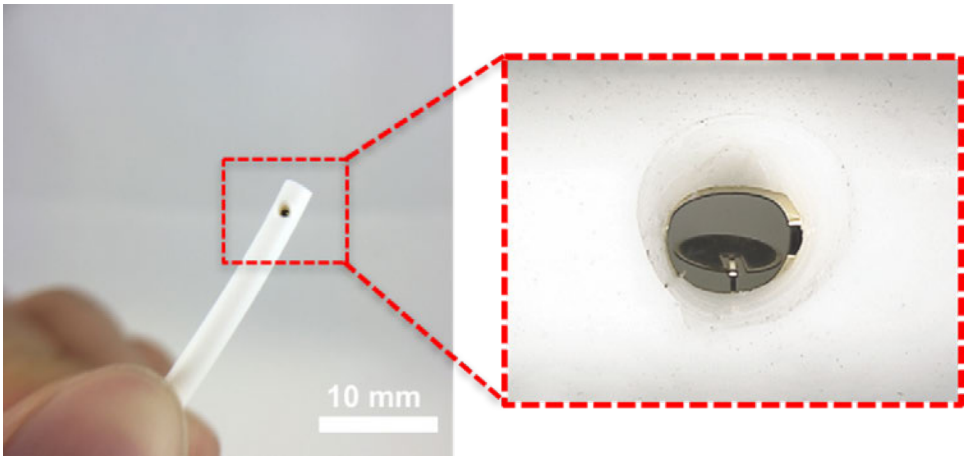

Fig. 2.18. Images of integrated thin-film magnetic microactuators into an implantable silicone-based catheter to provide self-clearing capability.

3. PIEZORESISTOR-EMBEDDED MULTIFUNCTIONAL MAGNETIC MICROACTUATORS FOR IMPLANTABLE SELF-CLEARING CATHETER

Hydrocephalus is a neurological disease characterized by excessive accumulation of cerebral spinal fluid (CSF). The gold standard for treating hydrocephalus is chronically implanting a drainage system to remove the CSF from the brain. Unfortunately, the implantable catheters are notorious for obstruction-related failures which can have devastating consequences for hydrocephalus patients [129–131]. Previously we reported fully integrated polymer cantilever based microscale magnetic actuators to realize a self-clearing catheter. Translational in-and-out of plane motion from the cantilever have been used to remove various obstruction materials. However, as we move forward to examine *in vivo* efficacy of our self-clearing catheter, the need to periodically monitor the performance of implanted microactuator became apparent. Here we integrated gold-based piezoresistive strain-gauge on our magnetic microactuators to measure the device deflection. With the integrated strain-gauge, we demonstrate multi-functional capabilities of our magnetic microactuators that facilitates device alignment, measure flow rate through the pores, and detect the presence of obstruction. This development brings us a step closer towards a smart hydrocephalus shunt system that can improve the patient outcome.

3.1 Introduction

Hydrocephalus is a neurological disease characterized by an excessive accumulation of cerebral spinal fluid (CSF) in the ventricles of the brain. The gold standard of hydrocephalus treatment is the implantation of hydrocephalus shunts through which CFS can be diverted out of the brain. However, the failure rate of these shunt systems

remain high, especially among children. A clinal study conducted from April 2008 to December 2011 reported that 33% out of 1036 patients experienced shunt failure [130]. The time at which the shunt fails is also alarming. In a more recent clinical study, Anderson et al., reported that 30-day shunt failure rates range from 9-18% for primary shunt implants and 23-26% for revision shunts [131]. Among failure cases, up to 77% were due to shunt malfunction, which includes obstruction, over-drainage, and loculated ventricles [129, 130].

Previously, we reported the development of fully integrated self-clearing implantable catheter using thin-film polyimide-based magnetic microactuators [99,132]. The large out-of-plane motion of the microactuators in the presence of externally applied magnetic fields are used to provide local mechanical shear stress at the catheter inlet pores to disrupt biofilm and clear the obstructions from the catheter. This active mechanical removal mechanism was seen in an acoustic device that treats glaucoma drainage shunt failure [92]. The polyimide-based structure was robust enough to withstand more than 300 million actuation cycles while demonstrating significant protein and microbead clearance [105]. Moreover, our microactuators have been determined to be rugged enough to withstand up to the 7-Tesla Magnetic Resonance Imaging system while producing minimum heating or image artifact. [100]. Our hypothesis is that the in situ self-clearing capability will address obstruction-related shunt failures and increase the longevity of this critical implantable devices.

During our preliminary *in vivo* evaluation on the efficaciousness of the self-clearing catheter, however, the need to periodically monitor the mechanical responses of the microactuators became apparent. For example, we found that, once the device is implanted, it is impossible to verify whether the device is oriented properly or even actuating as expected. We also found that it is difficult to determine whether the animal condition is deteriorating due to a failed device or other complications. This difficulty in determining the cause of illness in shunted patients is also echoed by many clinicians. Given the average time to shunt failure of approximately 45 days [130], being able to prophylactically check the shunt status in the early days following

implantation would be immensely helpful in preventing a more catastrophic device failure.

Several groups have proposed methods to monitor catheter pore obstruction by measuring CSF impedance between inside and outside the lumen of ventricular catheters [133,134]. Impedance is modulated as a function of change in ionic concentration and inlet pore patency area due to biofouling and obstruction. The impedance of CSF, however, may be affected by changes in CSF constituents including blood, immune cells, and choroid plexus. Thus, here we explored a direct mechanical method integrated into our microactuator to determine whether the pore is obstructed. Using a piezoresistive strain sensor on our actuator, it is possible to measure amount of deflection. When the pore is free of any biofouling, the device will provide the maximum resistance change while the amount of deflection and the corresponding resistance change will decrease as the pore becomes more obstructed.

In this work, we used *ex vivo* blood clot to mimic biofouling obstruction that can be introduced during surgery or due to a traumatic brain injury. The intracranial hemorrhage often leads to bleeding into the ventricle, which can lead to post-hemorrhagic hydrocephalus with up to a 50% mortality rate [135]. Rapid removal of blood from the brain is crucial in improving patient outcome [136]. Although ultrasound wave has been shown to facilitate breakdown of blood clot mass with and without thrombolytic agents, application of ultrasound to deep brain structures likely remains a challenge [88, 91, 137, 138].

Here we demonstrate piezoresistor integrated magnetic microactuators that can provide additional capabilities including obstruction detection, device alignment, and flow rate measurement on top of existing biofouling-removal capabilities of the microactuator. The work principle in piezoresistivity is variation of the resistivity of the material itself due to an applied stress [139]. For Convention MEMS device, semiconductor materials are usually chosen for high sensitivity to strain and stress. Microscopic origin of piezoresistivity is from stress induced band gap and mobility change. Resistivity varies because of its dependence on electron mobility and carrier

density [140]. A common parameter describing piezoresistor performance is gauge factor G ($G = \frac{\Delta R}{R}/\epsilon$, where ΔR is resistive change, R is baseline resistance and ϵ is strain). For example, Single crystalline silicon and germanium have gauge factors greater than 150 [141]. Boron doped CVD deposited polysilicon substrate has a gauge factor up to 27 when annealed at 1100°C [142]. Single and poly crystalline diamond films show gauge factors above 2000 [143]. However the problem with semiconductor based piezo resistor is that deposition and annealing temperature is easily above 400°C hence not compatible with polymer substrate. Recently, nanomaterial-based resistive transducers have been reported and they are notable for exceptional sensitivity at small strain and stress [144, 145]. However, integration of these material requires more complex fabrication steps that affect manufacturability.Metals can also be used as piezoresistors. Resistance variation of metal mostly comes from stress induced geometry change and normal gauge factor of a thin metallic pattern is between 2 and 5 [139]. Metal can be easily deposited and patterned on polymer film by evaporation or sputtering followed by lift off without damaging underneath polymer layer. The thin-film gold (Au) strain gauge is chosen for its biocompatibility, chemical inertness, linearity, and ease of fabrication. There are several examples of using Au in a microfabricated pressure sensor and implantable applications [146,147]. Furthermore, the G of 1-2 from Au piezoresistor provide more than enough sensitivity to generate detectable signal given large deflections of our magnetic microactuators.

3.2 Device Design and Fabrication

3.2.1 Device Design

The general structure of the flexible micro magnetic actuator follows our previous design [105, 132]. In short, the device consists of a rectangular polyimide cantilever with a tip mass structure attached at the end. The tip mass structure consist of a near circular polyimide base and Ni ferromagnetic element on top. Tip mass rotate in response to magnetic field and deflect cantilever. The newly integrated Au piezoresis-

tor is located at base of cantilever to maximize the change in resistance. The shape of piezoresistor follows conventional serpentine pattern to increase net resistance given the confined space [148]. The design has three windings evenly distributed at width of cantilever. Entire area of piezoresistor including the contact pads has a total of 109 effective squares in which 94% is on active region that experiences stress from cantilever deflection.

3.2.2 Microfabrication Process

Fabrication of polymer-based magnetic microactuators with piezoresistive element was adapted from our first-generation flexible device [105]. Fig. 3.1 illustrates the fabrication steps. On top of a 100 mm single-side polished silicon wafer, 500 nm of silicon dioxide (SiO_2) release layer was deposited using PECVD (Axic, Milpitas,CA). Next, polyimide (PI2525, HD Microsystem, Parlin, NJ) was spin coated at 1600 rpm and cured in a nitrogen oven. Prior to coating, an adhesion promoter (VM-652, HD Microsystem, Parlin, NJ) was applied onto the oxide layer to improve adhesion. The polyimide thickness was verified to be 10.7μm using an Alpha-Step IQ surface profiler (KLA-Tencor, Milpitas, CA).

On top of polyimide layer, the piezoresistor (20 nm Cr and 50 nm Au) was deposited using an e-beam evaporator (Airco) and lifted off using a predefined photoresist mold. Following the metal deposition, a second layer of polyimide (PI 2545 HD Microsystem, Parlin, NJ) was spin-coated at 8000 rpm to achieve 1.2 μm-thickness. Cr/Au adhesion and conduction layer was then evaporated on the wafer globally in preparation for Nickel (Ni) electroplating. A 8-μm-thick of Ni ferromagnetic element was deposited and defined by the plating mold (AZ9260, MicroChemicals GmbH, Ulm, Germany). Afterwards, the outline of structural plate, cantilever and device boundary was dry-etched using oxygen (O_2) plasma (Advanced Oxide Etcher, STS, Newport, UK). Polyimide pattern was etched down until the sacrificial SiO_2 layer was exposed. The samples were released in 6:1 buffered oxide etchant that removed the

sacrificial layer. After the devices were detached and collected, piezoresistor contact pads were opened up using O_2 plasma.

3.2.3 Device Integration into Catheters

The integration of the thin-film device into an implantable catheter requires accurate alignment between actuator and the inlet pore. Once they are aligned, thin film substrate also needs to be secured and immobilized even in the presence of flowing liquid. Furthermore, an electrical connection between piezo resistor and measurement equipment needs to be established. To satisfy these requirements, a 'needle and thread' integration approach was developed. Two 15-inch long magnet wires were aligned and attached to the gold contact pads located at the end of the piezoresistor. Electrically conductive joints between wires and pads were formed by applying liquid silver paste (CI-1001, Engineered Conductive Materials, Inc, Delaware, OH) and curing on hotplate at 85 °C for 10 min. The wires along with actuator substrate were then transferred and bonded to a small piece of polyimide tape for increased structural integrity. Afterwards, the entire sample was coated with Parylene C (PDS 2010, Specialty Coating System, Indianapolis, IN) for improved insulation and biocompatibility.

Next, the microactuator substrate was cut so that it can fit inside the lumen of the catheter. Using a commercial implantable catheter (Central Venous Catheter Set, Cook Inc. Bloomington, IN), a 1.2-mm-diameter pore was manually punched. The free ends of the two wires were inserted through the pore and pulled out from catheter opening. Then, the actuator was dragged through the pore opening to complete the assembly. Once the thin-film device enters the lumen of the catheter, it curled around the inner wall. Finally, the catheter end with wires was sealed with silicone adhesive. To test the robustness of the integration, deionized water was manually injected to catheter opening using a 10 ml syringe. The actuator was able to withstand five consecutive bursts of flow (>5 ml/s) without being dislodged or

shifting in position. Fig. 3.1 shows an example of fully assembled smart catheter with piezoresistor-embedded multifunctional magnetic microactuator.

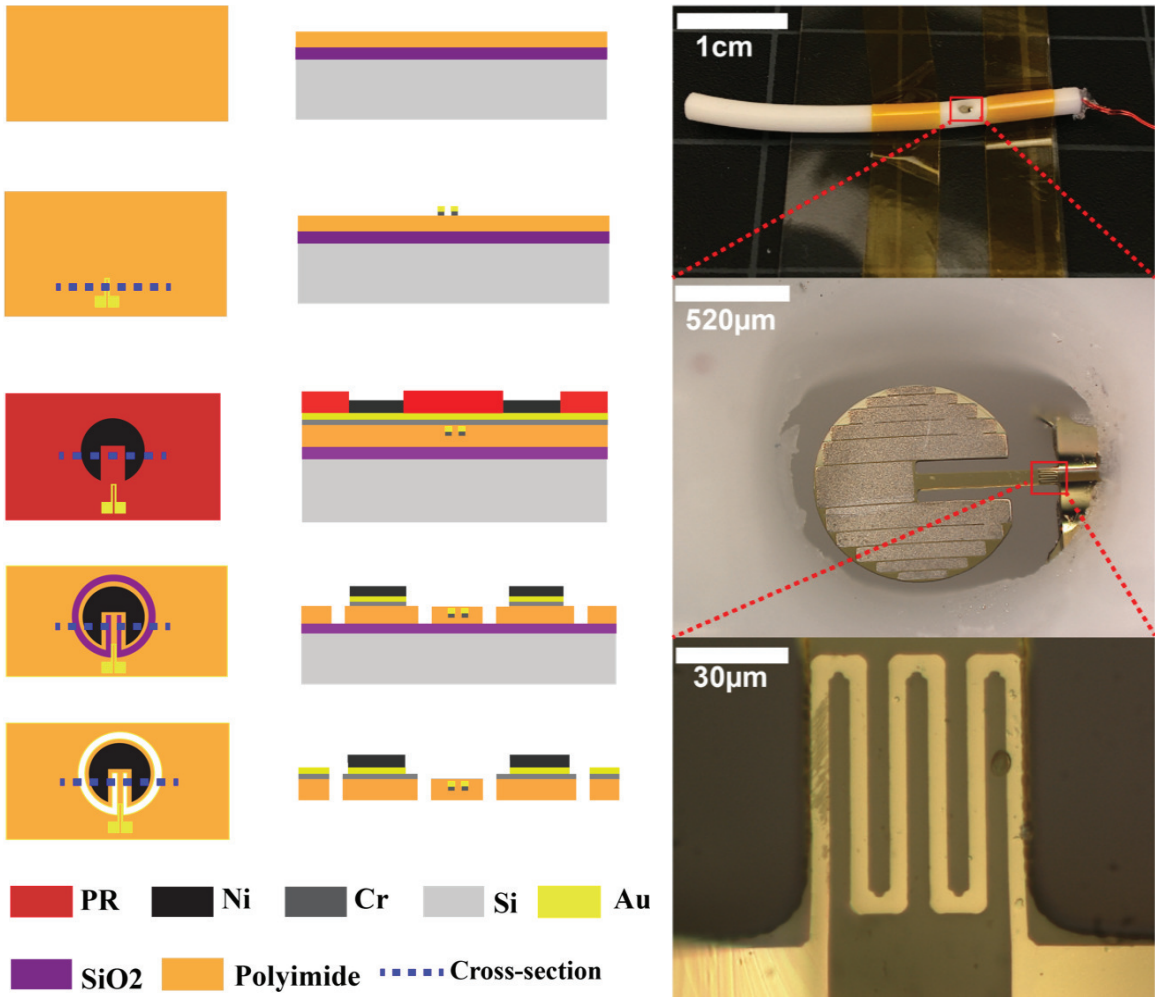

Fig. 3.1. Process flow and fabricated multifunctional smart catheter. Left: top and corresponding cross-sectional views of each fabrication step. Right: photographs of fully integrated smart catheter with piezoresistor-embedded multifunctional magnetic microactuators.

3.3 Characterization

3.3.1 Static and Dynamic Responses

A bespoke electromagnet and a test fixture was used to assess the performance of the piezoresistive strain gauge of a fully integrated smart catheter sample. The fundamental function of the strain gauge is to provide static deflection angles as a function of percentage resistance change. The change in resistance was measured through the wired connection using a custom LabView 2013 with a 4-wire resistance measurement mode. A static deflection response was measured by actuating the device in short magnetic pulses at different magnetic flux density produced by an electromagnet in a direction perpendicular to the catheter pore (Fig. 3.2). Static deflection results showed that the thin-film piezoresistor has adequate sensitivity (0.035%/Deg) with a range $-30°$ to $30°$. The expected percentage change in resistance R is calculated from equating cantilever deflection angle ϕ to maximum stress σ_{max} produced by point force F on the tip of cantilever:

$$\phi = \frac{FL^2}{2EI}; \sigma_{max} = \frac{FLt}{2I}; \tag{3.1}$$

$$\frac{\Delta R}{R} = G\frac{\sigma_{max}}{E} = \frac{Gt\phi}{L} \tag{3.2}$$

with cantilever beam length L, thickness t, elastic modulus $E = 2.45$ GPa for polyimide, and the moment of inertia $I = \frac{wt^3}{12}$ for rectangular beam. Experimental results indicated that our Au piezoresistor closely matched G of 1.1, which corresponds well with G values from literatures (Fig. 3.2). Static deflection angle and resistive response to 10 to 50 mT was tested because that is the range of field strength we are able to generate and intend to test with. The upper limit of our magnetic coil for our future in vivo animal study is 54 mT due to amplifier current constraint.

The dynamic response of the magnetic actuator can also be measured using the strain gauge. Using our electromagnet, a sinusoidal magnetic field (<10 mT) was swept from 5 Hz to 1 kHz in 20 s. A function generator with output voltage at 1.5 V_{pp} and an amplifier was used to supply current to the electromagnet (Fig. 3.3). The

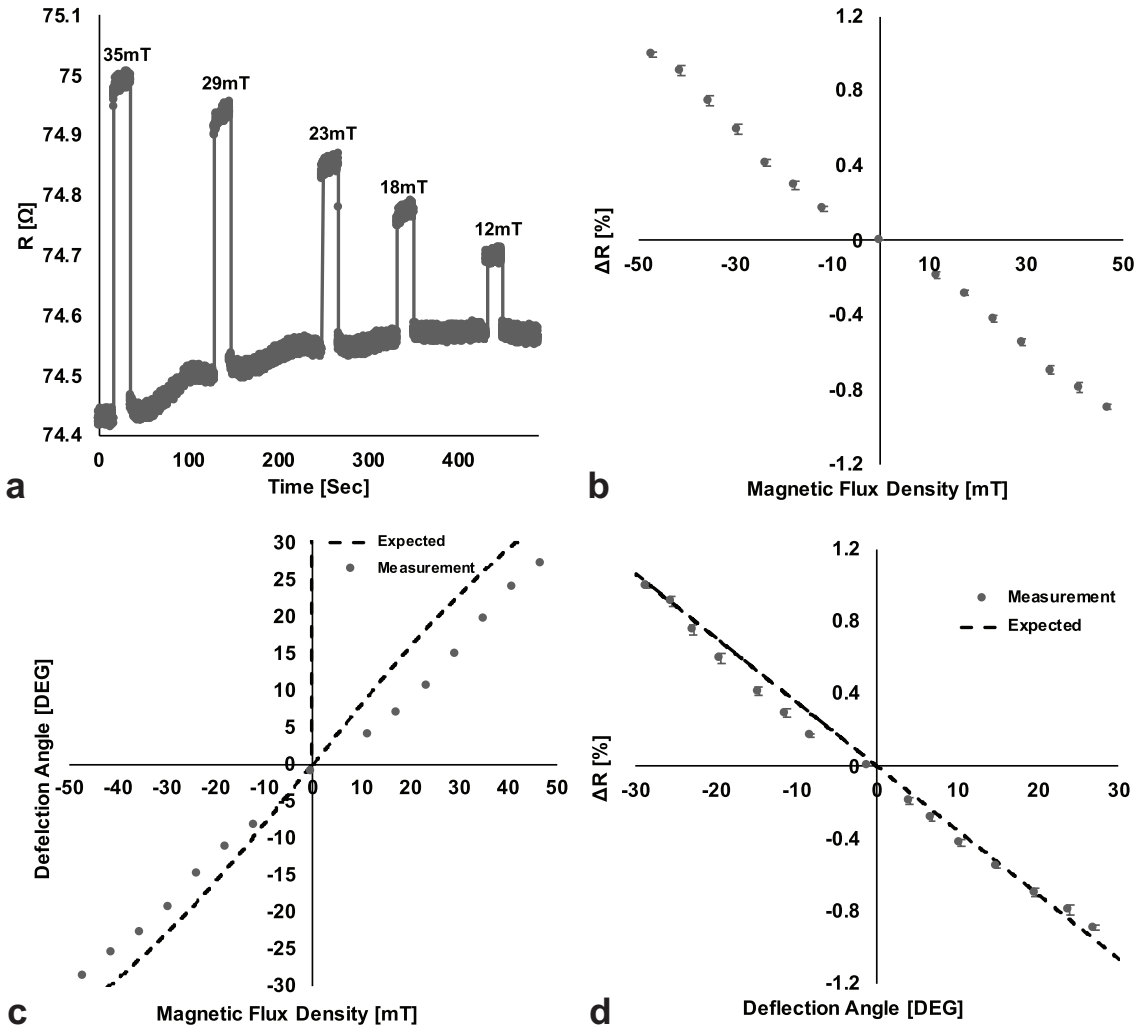

Fig. 3.2. Static characterization. (a) Resistance value under various pulsed magnetic flux density. (b) Percentage of resistance change as a function of actuation strength and actuation direction. Positive change indicates deflecting downwards and negative change indicates deflecting upwards ($n = 3$). (c) Deflection angle as a function of magnetic flux density (n = 3). Theoretical line calculated by torque balance [105, 132]. (d) Percentage of resistance change as a function of deflection angle ($n = 3$). Theoretic line indicates predicted value of resistance change of $G = 1.1$ for sample with L = 655 μm, w = 76 μm, t = 12 μm)

resistance was sampled at 6.48 kHz and the amplitude spectrum representing the relative deflection was converted into frequency response using Fourier transform. Fig. 3.4 demonstrates the dynamic responses of a cantilever in air and in deionized (DI) water. The results indicate our integrated strain gauge can detect critical characteristic of magnetic actuators such as resonant frequencies and quality factors.

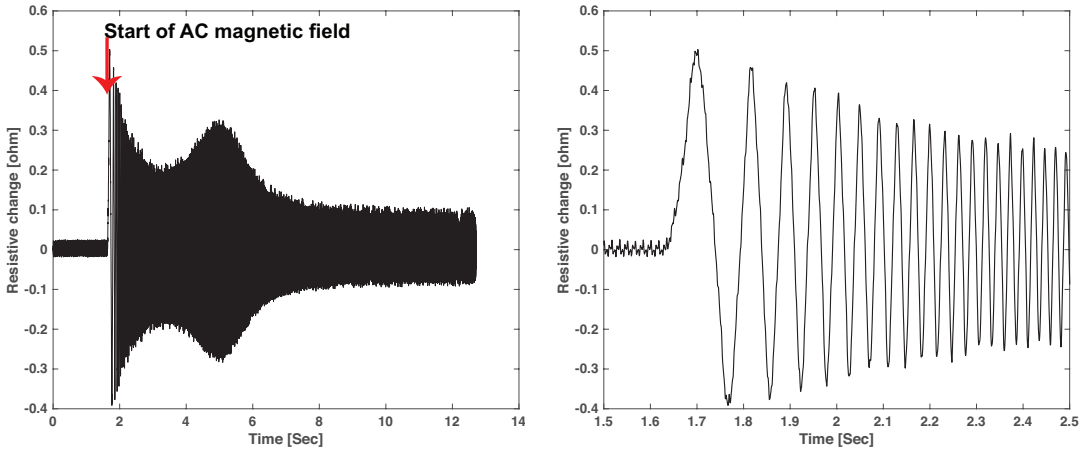

Fig. 3.3. A representative resistive response from time-varying magnetic field swept in freqeuncy.

3.3.2 *In Situ* Device Alignment and Positioning

The orientation of externally applied magnetic field relative to the position of the implanted device is critical in ensuring maximum device deflection. However, it is difficult to ascertain whether the device is fully deflecting once it is implanted. Even with live fluoroscopic imaging, the microscale device is too small to resolve. Here we demonstrate that the integrated strain gauge can provide a method to optimize device alignment with external magnetic field and to determine whether the device is fully

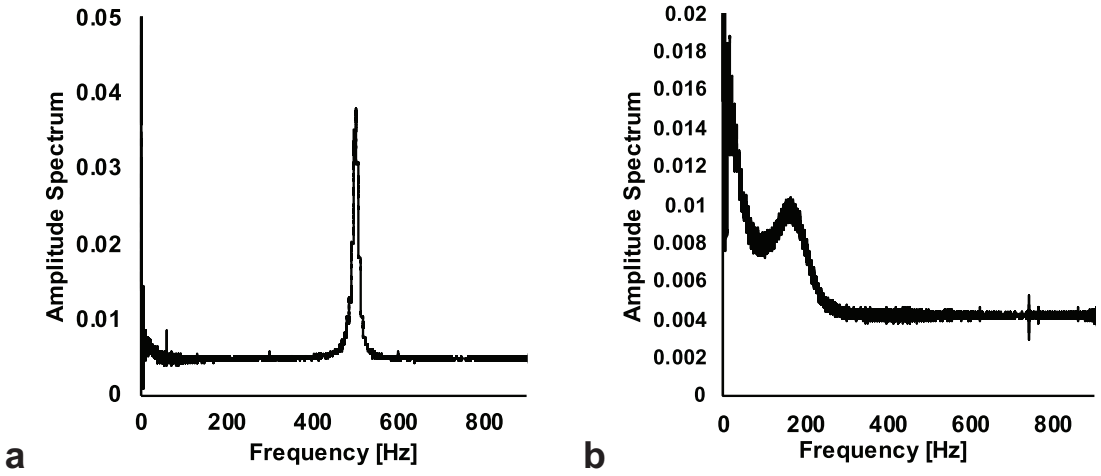

Fig. 3.4. Dynamic characterization. Representative frequency responses from the integrated strain gauge in a smart catheter (a) in air and (b) DI water.

deflecting. The relationship between misalignment angle θ and cantilever deflection ϕ can be described by balancing the mechanical (τ_{mech}) and the magnetic torque (τ_{mag}):

$$\tau_{mech} - \tau_{mag} = 0 \tag{3.3}$$

$$k_\phi - v_m M H \sin\left(\frac{\pi}{2} - \theta - \phi\right) = 0 \tag{3.4}$$

with the rotational stiffness $k_\phi = \frac{EI}{L}$, the volume of magnet v_m, the magnetization $M = 0.6\ T$ for Nickel, and the applied magnetic field strength H. Given the same amount of magnetic field H, deflection angle ϕ can be solved as a function of misalignment angle θ. The cantilever displacement will be smaller with greater misalignment. Experimentally, this relation can be measured in real time using our strain gauge. At the center of our electromagnet, a fully integrated smart catheter was taped at bottom of a beaker supported by a custom 3D printed test fixture that can tilt. The text fixture can be fixed at various misalignment angles (0–50°) with respect to the horizon (Fig. 3.5a). The beaker was filled with DI water to mimic cerebral spinal fluid environment. For each alignment angle, a magnetic field strength of 20 kA/m was pulsed for a least 3 s (Fig. 3.6). The change in resistance was recorded using a custom LabView DAQ system (NI PXI-1010) with 4 wire resistance measurement mode. Two pairs of probes were connected to two resistance terminals. One pair was used to supply current while another for sensing voltage. Using the previously characterized strain gauge calibration, the net deflection of our actuators were estimated (Fig. 3.5b). With this alignment information, the orientation of external magnetic coil can be adjusted to produce maximum deflection. In practice, the clinicians may be able to utilize this information during implantation surgery and actuation procedure to optimize the placement of device and the electromagnet.We envision that alignment is determined by active deflection of actuator from pulsed magnetic field and compare resistive changes ΔR obtained from different external coil placement angles. Once maximum pulsed resistive change is observed, coil placement is fixed and we claim optimum placement is achieved. Fig. 3.5b serves as general misalignment angle reference.

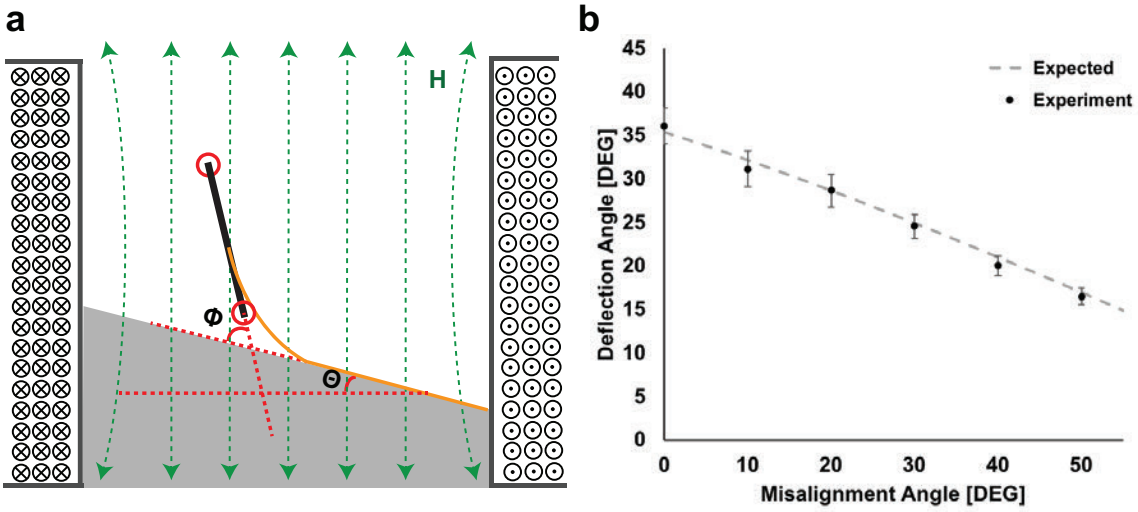

Fig. 3.5. (a) Illustration of device misalignment. If the device orientation is not perpendicular to the applied magnetic field, the misalignment angle θ can affect the device deflection ϕ. (b) Deflection angle as a function of misalignment. For a given magnetic field strength, the deflection angle ϕ decreases as a function of misalignment θ which can be used to ensure that the magnet is oriented properly during actuation (n = 3).Theoretical line calculated for sample with v_m = 0.003 mm^3, L = 405 μm, t = 12 μm and w = 47.5 μm

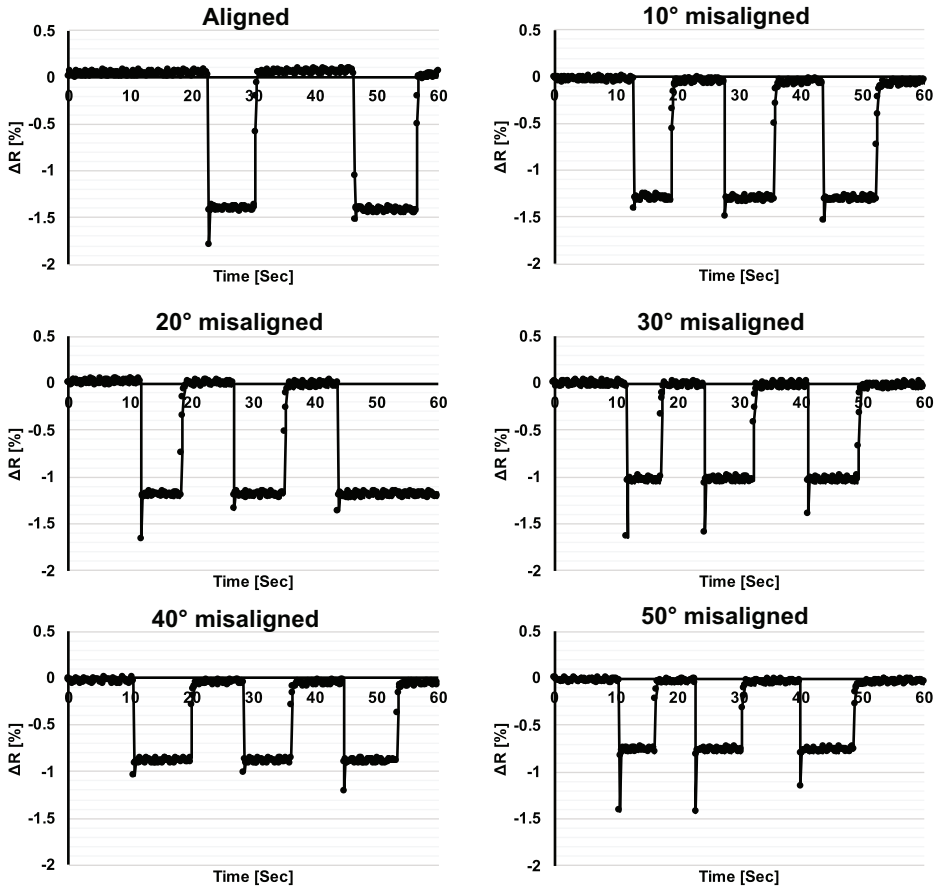

Fig. 3.6. Resistive change under varied misalignment angles from 0 to 50 degrees. Magnetic field with fixed amplitude was used to generate step responses for all cases.

3.3.3 Flow Rate Measurement

Microactuator can not only be deflected using the externally applied magnetic field but also be deflected passively due to flow of cerebrospinal fluid (CSF). When excessive CSF is being drained through the catheter pores, the drag force can bend the cantilever inward and the resistance change can be estimated by modeling the fluid drag $F = \frac{1}{2}\rho v^2 C_d A$ on a perpendicular thin plate, with the fluid density ρ, the fluid velocity v, the drag coefficient of the plate C_d, and the area of structural plate A. The stress at base of cantilever can be derived from assuming a point force is concentrated at tip. Piezoresistor is experiencing maximum stress, the resistance change can be described as

$$\Delta R = \frac{\rho v^2 C_d A R G L t}{4EI} \tag{3.5}$$

Gauge factor $G = 1.1$ determined from previous static response was used. The only unknown was the drag coefficient C_d. Bench-top experiments were carried out to characterize the flow rate-resistance relationship. In an evaporating dish, a smart catheter with integrated microactuator was immobilized and submerged in DI water. The open end of the catheter was connected to a S16 tubbing (Masterflex, Cole-palmer) driven by peristaltic pump, which pumped DI water into the catheter as shown in Fig. 3.7a. The volume flow rate was calibrated by measuring the mass of the pumped water. The pump was driven at various flow rates (2–15 ml/min with 1ml/min decrement) and the corresponding resistance change relative to the baseline values were measured (Fig. 3.7). CSF production rate was reported between 0.3ml/min to 0.7ml/min [112, 149].

3.3.4 Obstruction Detection and Removal

As mentioned in the introduction, one of the biggest clinical challenges for clinicians is to non-invasively determine whether the implanted catheter is failing due to obstruction. Here we demonstrated that by monitoring the dynamic responses of our

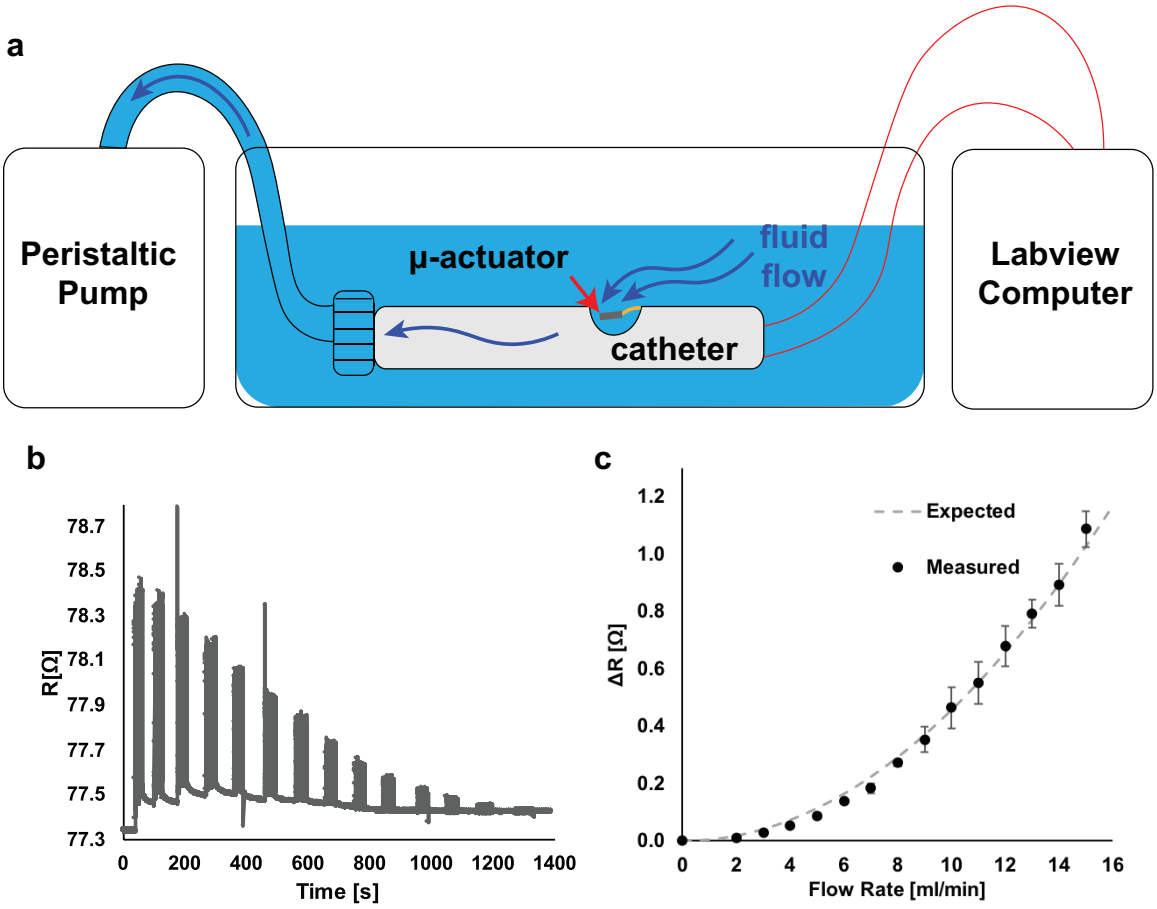

Fig. 3.7. (a) Schematic of flow rate measurement. The peristaltic pump draws the fluid into the catheter which deflects the microactuator. The strain gauge on the microactuators can be used to calculate the flow rate. (b) Example of continuous measurement of piezoresistor response at various flow rates. (c) Change in resistance as a function of flow rate. Note that the expected values were calculated using $G = 1.1$ and drag coefficient $C_d = 2$ (n = 3) for sample with L = 655 μm, w = 76 μm, t = 12 μm. Flow velocity v is calculated from flow rate (2-15ml/min) through the catheter with inner diameter ID of 0.9144 mm. Structural Plate area A is calculated from circle with diameter of 850 μm. Water density $\rho = 1000$ Kg/m^3 is used.

magnetic microactuators, it is possible to detect a presence of an obstruction at the inlet pore. Moreover, it is possible to mechanically remove obstruction by actuating our devices. After drawing blood sample from a euthanized pig, a blood clot was formed by dropping 2 ml of blood into a phosphate buffered solution. The baseline dynamic response of the device was measured as described. The blood clot mass was gently squeezed into the catheter pore to mimic a robust obstruction following which the dynamic response was measured again. With the blood clot obstructing the movement, the dynamic response was suppressed significantly. Next, a low frequency high amplitude actuation protocol was applied at 20 Hz at 25 KA/m for 3 min, which dislodged and removed the blood clot mass. Finally, the dynamic response was then captured again to demonstrate restoration of characteristic peaks (Fig. 3.8e). This results illustrate the possibility of using strain sensor and the dynamic actuator responses to detect the presence and absence of obstruction in the inlet pores of implantable catheters.

3.4 Discussions and Conclusions

Here we designed, fabricated, and tested flexible magnetic microactuators with integrated piezoresistive strain gauges to improve the functionality of chronically implantable catheters. We demonstrated that the integrated strain gauge may be used for a number of different purposes. By monitoring the resistance change as a function of microactuator deflection, we determined whether the catheter pores were aligned to provide maximum deflection. The resistance changed linearly with respect to the deflection range of $\pm 30^{\circ}$, which corresponded well with the expected values. We also demonstrated the fluid flow sensing capability which may be used to monitor the CSF flow rate *in situ*. Moreover, our strain-gauge integrated microactuators showed the capability to detect the presence of catheter pore obstruction.

The additional feature enabled by integrating the strain gauge on our actuator may eventually be useful in clinical practice. As previously mentioned, it is difficult

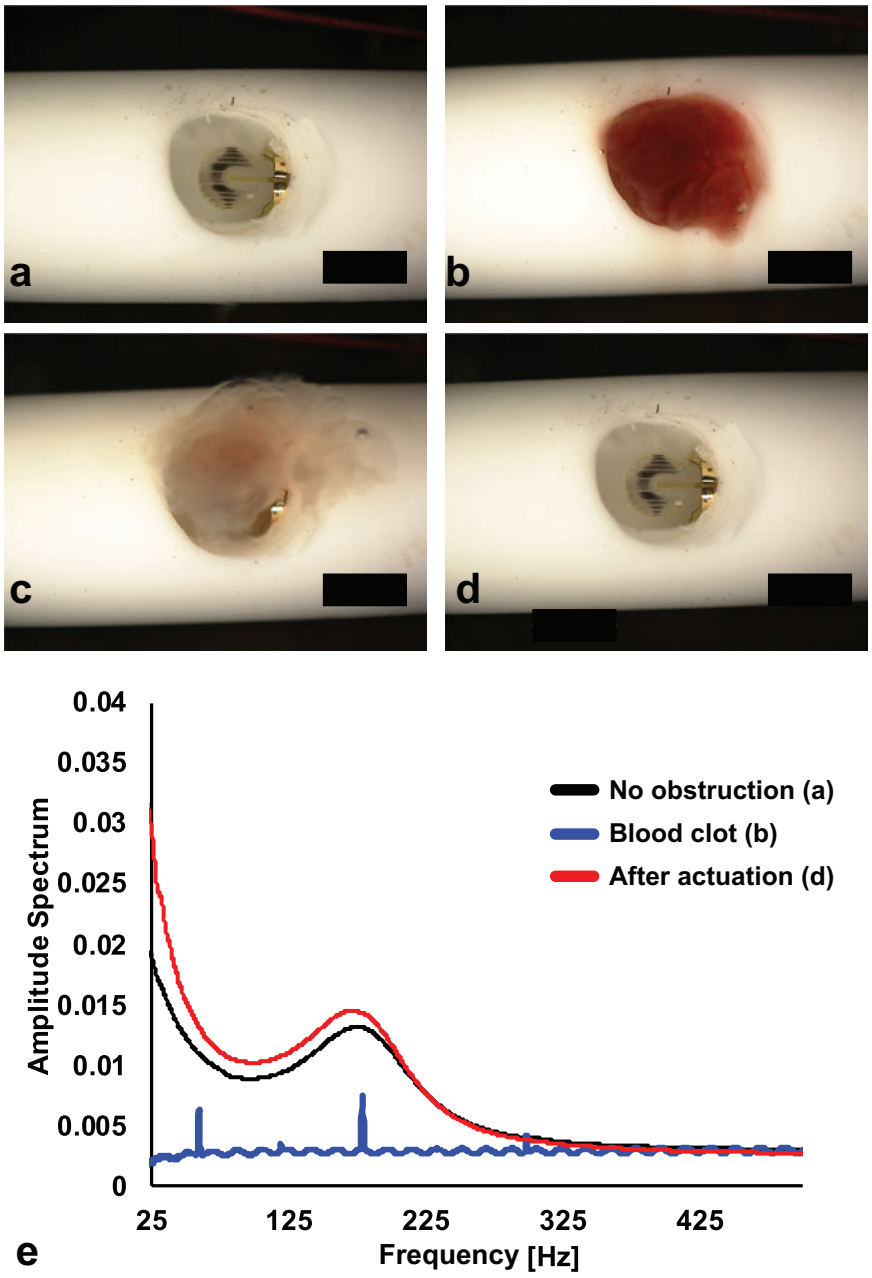

Fig. 3.8. Optical images of catheter pore before and after blood clot obstruction removal: (a) before blood clot occlusion, (b) occluded catheter pore, (c) during actuation, and (d) after the blood clot removal. (scale bar = 1 mm) (e) Corresponding frequency responses before and after blood clot obstruction. Note that when the blood clot is obstructing the inlet pore, the dynamic response is completely attenuated. Following large amplitude actuation and blood clot removal, the dynamic response is restored to show characteristic peaks.

to determine whether the microactuators are deflecting as intended once the catheter is implanted. These integrated sensor allows non-invasive *in situ* probing of microactuator status to ensure that the devices are functioning as expected. Moreover, the integrated sensor provides a method to ensure that the catheter is oriented property to provide maximum anti-biofouling capabilities. Most importantly, the new smart catheter provides a real-time monitoring of implant failure due to pore obstruction. By comparing the dynamic responses of the microactuators before and after obstruction removal, it is possible to use the microactuators to determine the presence of the obstruction, remove it, and show that the obstruction has cleared, which will ultimately reduce the need for frequent device replacement. As we move forward to *in vivo* evaluation of these implantable catheters, these additional features will be of great importance.

Nevertheless, there are additional work needed to fully embrace the integrated strain-gauge approach. Since the goal of magnetic microactuators are to prolong the lifetime of the implantable catheter, the long term reliability of the piezoresistive strain gauge sensor cannot be overlooked. The resistance baseline drift is a well-recognized issue in using piezoresistor-based strain gauges [150–153] due to temperature fluctuation, material aging and mechanical fatigue [108]. We also noted that some devices also show an increased baseline resistance over time (Fig. 3.7). The cause of base line drift is most likely due to mechanical creep in polymer and small deformation of Au contact pads over time. Viscoelastic material, such as polyimide, exhibit increased strain over time under abrupt constant stress [154,155]. In addition, the flexible nature of polymer thin film substrate makes Au contact pads susceptible to bend due to environmental impact. A similar claim was reported by [151]. For alignment, fault detection and deflection angle sensing, active magnetic field driven differential measurements are implemented and they are unaffected by baseline drifting effect. For a passive flow rate measurement, however, resistance drift may be a problem since an absolute resistance value is needed. Additional bonding between substrate and catheter sidewall may greatly reduce substrate deformation hence al-

leviate substrate deformation induced baseline shift. In future iterations, a reference resistor [156] or half Wheatstone bridge [157] should be incorporated to compensate or minimize additional unwanted adverse effect such as temperature variation. For this iteration, our priority is to demonstrate functionality and hence dummy resistors was not included in the design. Moreover, we will also need to characterize the long-term stability and mechanical integrity of the thin-film piezoresistor. Although we have previously demonstrated that our polyimide-based microactuators are robust enough to withstand up to 300 million actuation cycles [105], we need to ensure that the thin Au layer structure can also withstand large actuation cycles. Finally, we will need to incorporate wireless capability to measure the changes in resistance for the device to be truly useful in clinical settings. The current wired integration facilitates the bench-top proof-of-principle evaluations. However, the extended wire can be a point of mechanical failure as well as site of infection if transcutaneous. Thus, future work will include integration of passive wireless telemetry capabilities to fully enable our smart self-clearing and self-monitoring catheters.

4. RAPID REMOVAL OF BLOOD CLOT USING SELF-CLEARING CATHETERS FOR IMPROVED TREATMENT OF INTRAVENTRICULAR HEMORRHAGE AND POST-HEMORRHAGIC HYDROCEPHALUS

Maintaining patency of indwelling drainage devices is critical in preventing post-hemorrhagic hydrocephalus (PHH) following an intraventricular hemorrhage (IVH). The highly deadly condition may be curtailed if the blood can be removed rapidly from the brain. Surgeons using external drainage devices to remove blood often have to replace the ventricular catheter that is occluded with hematoma. Here we report a series of in vitro and in vivo evaluations to demonstrate that our self-clearing catheter can expedite removal of hematoma from the ventricle and improve the outcome after an IVH and PHH. Using an implantable magnetic microactuator, we created a self-clearing catheter that can generate large enough forces to break down obstructive hematoma by applying time-varying magnetic fields. In a bench-top evaluation, we show that the self-clearing catheters can last >7x longer than traditional catheter in a blood-circulating model (211 vs. 27 min). Moreover, we show that the self-clearing catheter can maintain a low pressure for longer periods than the control (239 vs. 79 min). Using an IVH porcine model, we demonstrate that our self-clearing catheters have longer survival than control catheters (80% vs. 0%) over the course of 6 weeks. The treated animals also had significantly smaller ventricle sizes after 1 week of implantation compared to the control animals with traditional catheters. These results suggests that self-clearing catheter may have therapeutic benefits in improving the outcomes of critical patients suffering from often deadly IVH.

4.1 Introduction

Brain hemorrhage is one of the most common and lethal forms of stroke affecting more than 2 million patients annually worldwide. In 45% of these cases, bleeding occurs inside the ventricles of the brain and leads to an intraventricular hemorrhage (IVH). When the blood clot (hematoma) forms and obstructs the circulation of cerebrospinal fluid (CSF), IVH can lead to an even deadlier condition (50-80% mortality) known as post-hemorrhagic hydrocephalus (PHH, 40% of IVH) [158, 159]. IVH is especially common in preterm pediatric patients with low birthweight and subsequent PHH can have devastating neurodevelopmental consequences [160].

A gold-standard in the treatment of IVH is rapid removal of hematoma using various interventional methods including open surgery, minimally-invasive catheter-based drainage, and thrombolytic agents to relieve the elevated intracranial pressure (ICP) [161, 162]. However, using anticoagulant on hemorrhagic patients is controversial due to the elevated risk of additional bleeding [163]. A recently completed large scale clinical trials for small molecule interventions (e.g., tissue plasminogen activator) have not demonstrated adequate benefit for IVH patients [164]. For most IVH patients, external ventricular drainage, ventricular reservoir devices, implanted shunt systems or neuroendoscopy are frequently used to remove hematoma [161, 165]. However, maintaining patency of the drainage devices is an enormous challenge as the ventricular catheters quickly become occluded with hematoma. Reducing the size of hematoma is a difficult challenge because the viscoelastic fibrin structure can often stiffen upon increased stress [166–168].

Catheter flushing often takes place in intensive care units but flushing alone often is ineffective in clearing the hematoma, which necessitates several neurosurgeries to replace failed drainage devices before the hemorrhage is finally cleared, which increases the risk of infection and other complications [169–171]. There are reports of using high-intensity focused ultrasound as a way to dissolve clots *in situ* [88, 89, 91, 138], however, the potential concern of off-target tissue damage in the brain still remains.

The obstruction issue of drainage devices has been well recognized for more than half a century. High failure rate of these important medical devices is an enormous issue in treating IVH, PHH, and other applications where chronic indwelling catheters are needed. Despite efforts to improve catheters with different biomaterials, anti-inflammatory and anti-biotic coatings, and architectural designs, many devices with novel features have been ineffective in clinics. A smart catheter that improves patient outcomes by resisting obstruction formation has largely been elusive.

Magnetic microactuators have previously shown to be effective in removing molecular and cellular scale biofouling materials on-demand using remote application of time-varying magnetic fields [99, 105, 172]. In this work, we demonstrate an alternative approach for rapidly removing localized thrombosis using large-deflection magnetic microactuators to maintain patency in implantable drainage devices. Typically, ventricular catheters have 16 or more inlet pores to ensure the drainage [173]. To facilitate the evaluation of our approach and to accelerate occlusion-related failures, we created single-pore ventricular catheters with and without magnetic microactuators. Using *in vitro* and *in vivo* experiments, here we show that these self-clearing catheters with magnetic microactuators can help reduce the size of obstructive hematoma, improve drainage device reliability, and increase the survival of IVH-induced animals.

4.2 Device design and fabrication

To fabricate the implantable magnetic microactuator for prevention of hematoma accumulation, we applied conventional surface micromachining techniques as described in the Methods section. Fig. 4.1a–f briefly shows the fabrication process. Fig. 4.1g highlights the two microactuator designs. The dimensions of each design is listed in Table 4.1.

The first design has a rectangular straight cantilever similar to what we have previously reported [105,106] but with increased nickel thickness.The new design features a serpentined flexure with tear-drop shaped ferromagnetic elements (Fig. 4.1g). The

serpentine flexure consists of 4 windings with 5, 400 μm-long straight segments connected by 4 arcs providing 100 μm gaps in between them. Similar serpentine flexures have been reported for making ultra low-frequency resonator and piezoelectric energy harvest devices [174–177]. The serpentine flexure provides a 6 times smaller bending stiffness and therefore enhanced deflection within limited footprint. In addition to improved beam design, the larger magnetic element aspect ratio provides additional magnetic torque compared to the first design despite having nearly identical volume because of geometric anisotropy (Table 4.1-4.2). A detailed description of the magnetic element dimensions and the analytical evaluation of magnetic torque is in the magnetic modeling and characterization section. The microfabricated thin-film microactuators were then integrated into a custom catheter to create a self-clearing ventricular catheter (Fig. 4.1h illustrates a typical actuation motion of a microactuator with serpentine flexure (Supplemental Video 1). In the presence of time and spatially varying magnetic field, the actuator deflects in and out of plane for a more dynamic hematoma removal (Supplemental Video 2).

4.3 Device characterization

Fig. 4.2-4.5 demonstrates the improvements of the new magnetic microactuator over convention straight beam design. We characterized the magnetic properties of the electroplated ferromagnetic elements using a magnetometer to calculate the magnetic torque assuming a field-dependent, non-saturated magnetization (Fig. 4.20). Fig. 4.2a-b show that the magnetic torque varies as a function of applied magnetic field angle θ and that maximum torque can be achieved at 40°. We saw as much as 75% improvement when the field angle θ equals to 40°.

We found that the new flexure design improved amount of displacement. The numerical analysis showed larger deflection and smaller stress on the serpentine flexure than the straight beam when a vertical point load was applied to its tip (Fig. 4.3). Fig. 4.4 shows varying degrees of deflection and corresponding maximum stress on

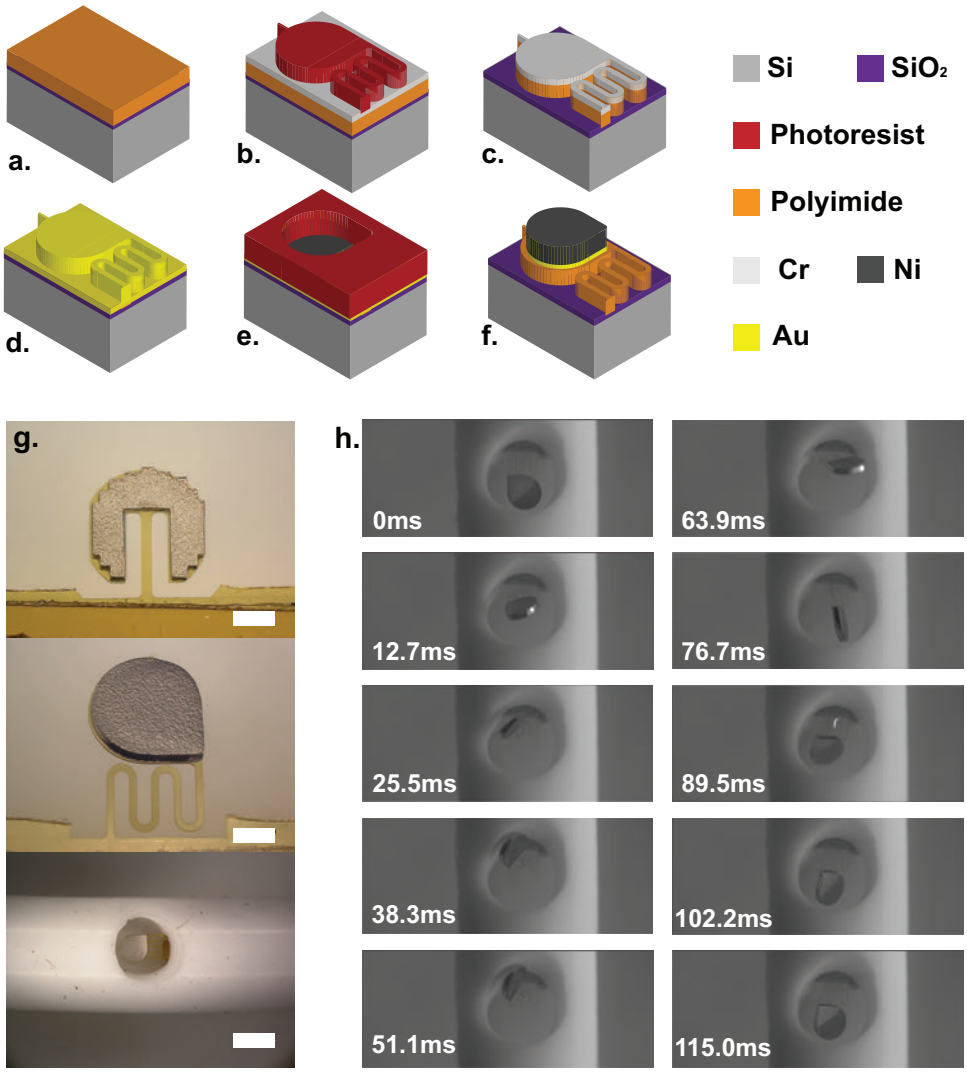

Fig. 4.1. Design and fabrication of self-clearing ventricular catheter. (a) Polyimide spin coat and curing. (b) Evaporation of Cr etching mask and define photoresist for actuator outline. (c) Wet etch of Cr and dry etch of polyimide. (d) Removal of of Cr and evaporation of Au as conduction layer. (e) application of photoresist and Ni electroplating. (f) removal of photoresist and remaining Au layer. (g) Optical images of fabricated magnetic actuator of straight type (top) and serpentine type (middle). Scale bars = 325μm. A catheter with integrated actuator (bottom). Scale bar = 1 mm. (h) A typical motion of actuation in deionized (DI) water for one actuation period.

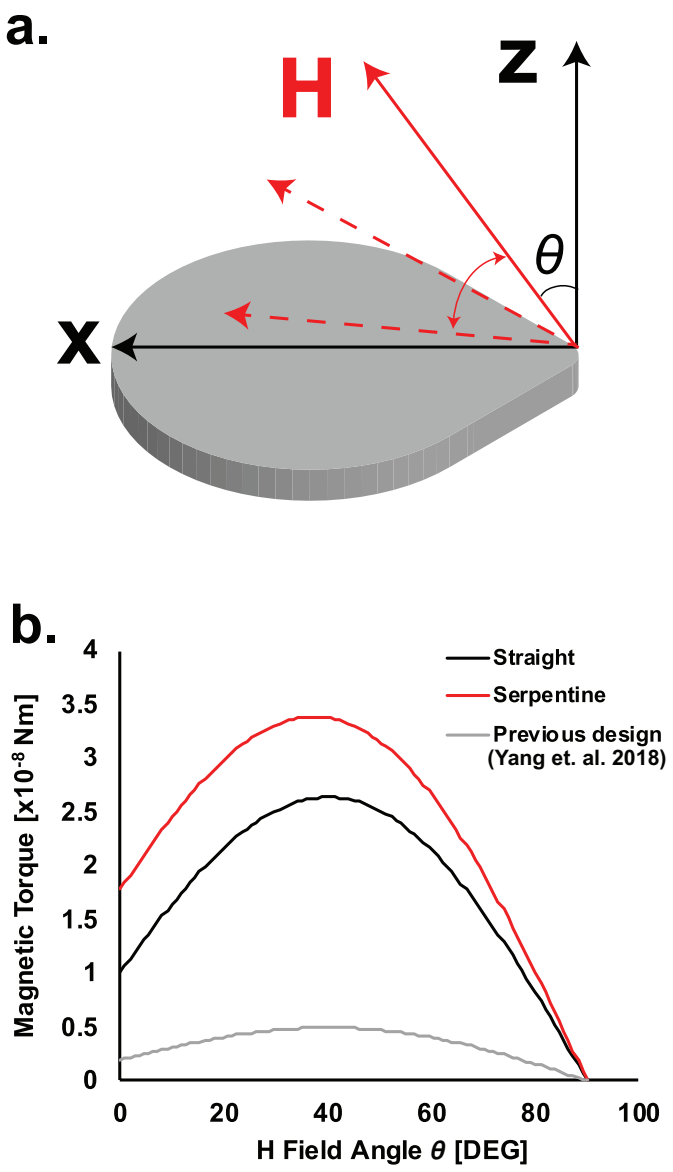

Fig. 4.2. Comparison of magnetic torque (a) Definition of coordinate system and magnetic field angle θ. (b) Calculated magnetic torque produced on ferromagnetic element of serpentine (red line) and straight actuator (black line) under 15 mT at different field angles.

the beam at various load range. We saw that the serpentine flexure provides twice as much displacement over the straight beam over the same loading condition. The maximum static stress calculated for serpentine flexure was 36 MPa at 0.1 mN, which is significantly lower than the tensile stress of this polyimide (131 MPa).

The 0.1 mN loading was chosen from magnetic resonant (MR) safety perspective [100]. A typical human whole body MR system produces a maximum spatial gradient between 10-50 mT/m [178–180]. Assuming the ferromagnetic element was fully saturated, 0.1 mN corresponds to the magnetic force produced from a gradient of 4 T/m, an order of magnitude greater than the physical constraint. Therefore, it is unlikely that our device will be damaged due to mechanical deformation in MR system.

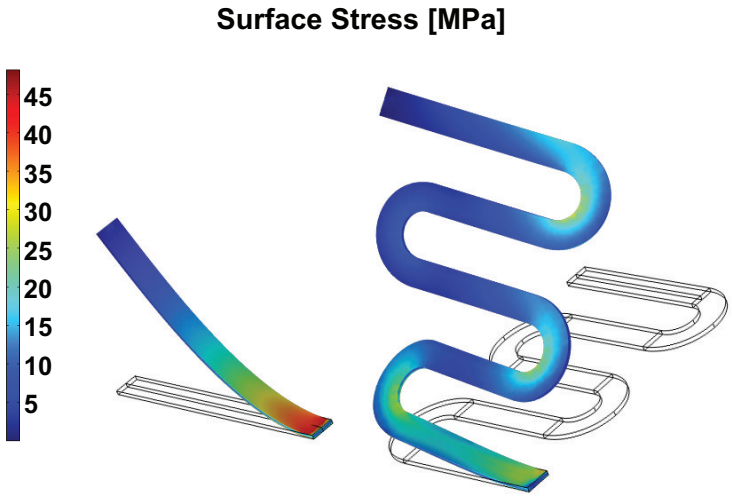

Fig. 4.3. Finite element analysis of stress distribution on cantilevers' surfaces under 0.1mN load at tip.

The improvements in magnetic torque and mechanical compliance of the flexure allow the new microactuator to achieve a greater deflection per given magnetic flux density (Fig. 4.5). Although the previous microactuators were effective against protein and cellular biofouling [98, 105], those were not effective against macroscopic hematoma. The microactuators were unable to maintain their motion when facing incoming hematoma at catheter inlet pore. Therefore, our primary objective was to

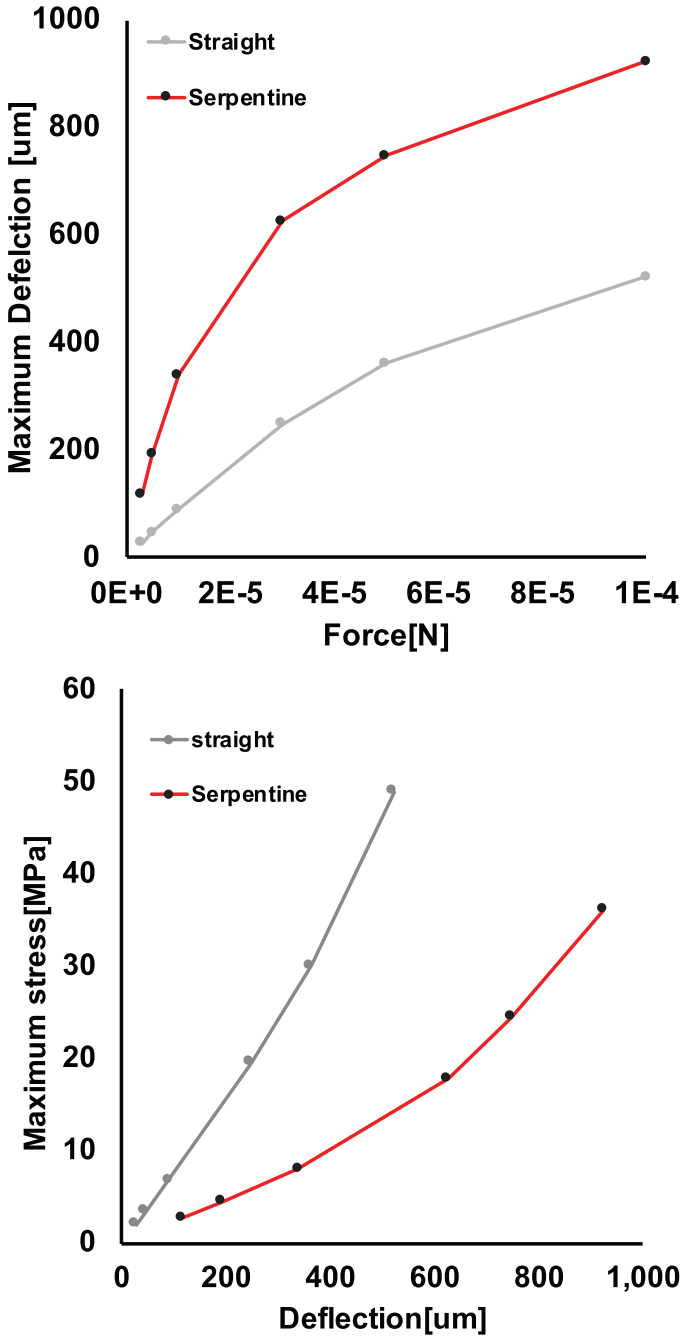

Fig. 4.4. Deflection and stress calculation. (a) Maximum calculated deflection under loading condition (0.01 to 0.1mN) for both cantilever type from finite element simulation. (b) Maximum calculated stress under various deflection condition for both cantilever type from finite element simulation.

increase the magnetic torque and rapid displacement to better remove a more robust thrombotic mass that plagues drainage devices in IVH patients. Our results show that we were able to achieve this goal. The new microactuator achieved >80° deflection with 15 mT compared to only 30° for the previous design.

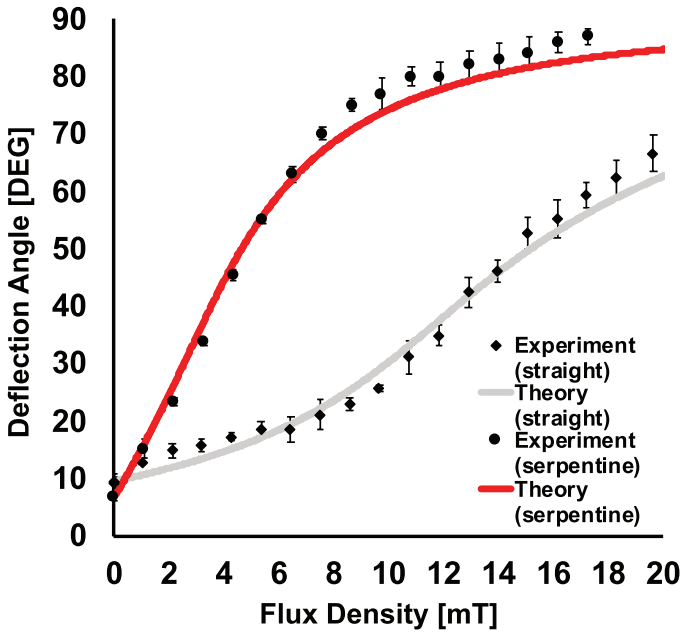

Fig. 4.5. Mechanical characterization of static response. Static deflection angle prediction and measurements for serpentine straight case. Data are expressed as mean ± standard deviation (n=3).

4.4 *In vitro* evaluation

To demonstrate blood-clot removal capabilities of self-clearing catheters, we developed an *in vitro* circulation system [181]. Although several groups have reported reduction of hematoma mass using a static condition [88,91], none have demonstrated an effective clot prevention capability in a continuous flow environment, which is more physiologically-relevant for our target application. Fig. 4.6 shows the experimental setup, which mimics a fixed-volume ventricle that circulates sanguineous phosphate buffered solution (PBS) as a CSF substitute.

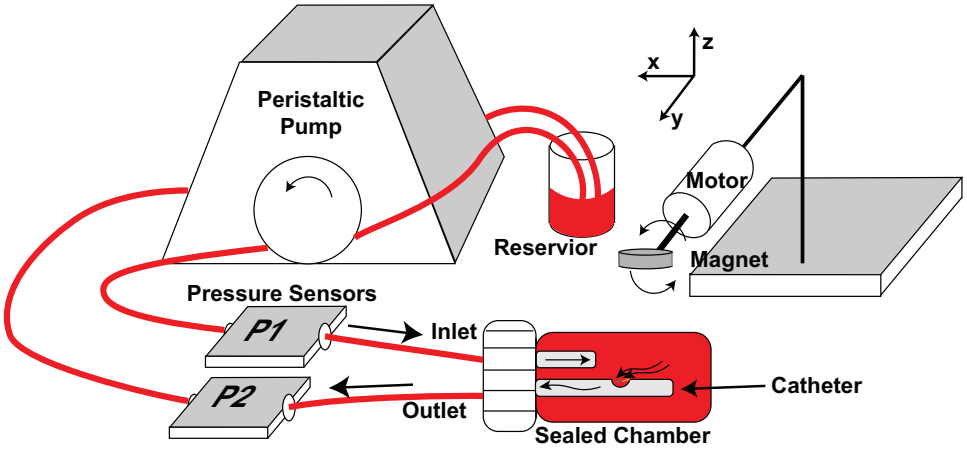

Fig. 4.6. Schematic of the *in vitro* bench-top blood circulation and magnetic actuation setup.

Using a peristaltic pump, we pumped diluted porcine blood (50:50 with PBS) out of the sealed chamber through different catheter designs (Fig. 4.7 top). The blood-PBS mixture ratio was determined experimental to produce hematoma within 4 h. As the fluid flowed the circulation system, we applied time-varying magnetic field on both control and self-clearing catheters (Fig. 4.23). We quantified the impact of magnetic microactuation by measuring differential pressure between the inlet and the outlet during the experiment. In general, the self-clearing catheters with integrated microactuators exhibited a smaller hematoma mass over their inlet pores compared to the control catheters (Fig. 4.7 bottom).

Fig. 4.8a-b show example differential pressure plot over the course of the experiments. Without any blood in circulation, the differential pressure ranged between 5–15 mmHg, which is comparable to the normal intraventricular pressure of a patient. However with blood, the control catheters exhibited an exceptionally high average pressure of 100 ± 111 mmHg whereas the self-clearing catheters had an average pressure of 11 ± 31 mmHg. In all 4 control catheters, we saw that the differential pressure remained above 40 mmHg at end of circulation period, indicating robust and sustained obstruction by a hematoma (Fig. 4.8a). Conversely, 7 out of 9 self-clearing catheters (3 straight and 6 serpentine devices) exhibited relatively lower pressure (<20

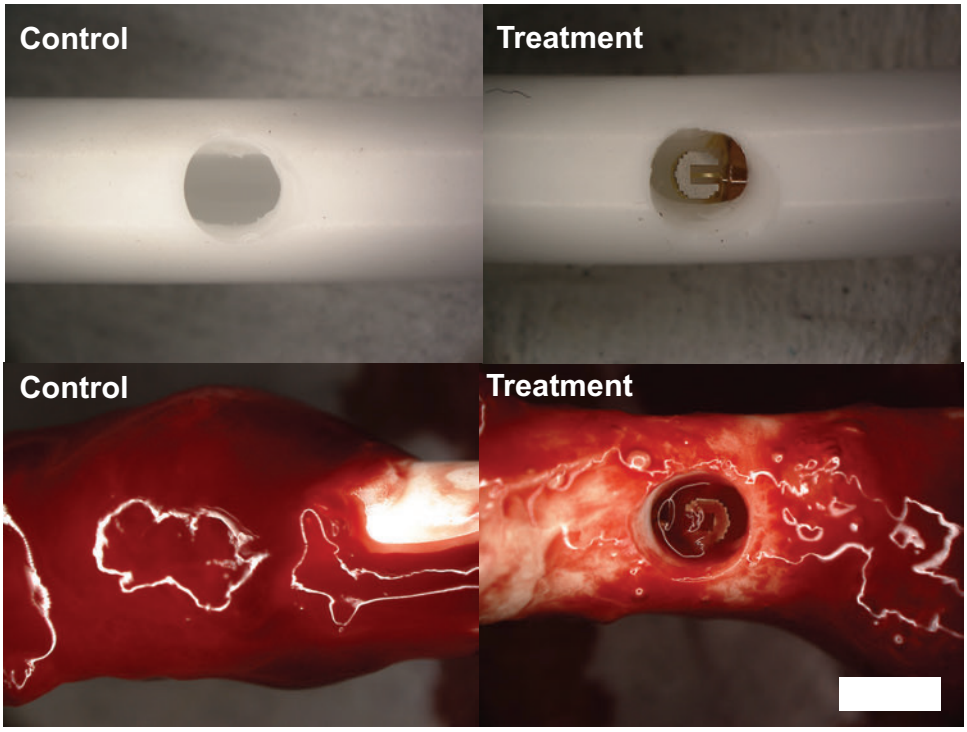

Fig. 4.7. *In vitro* A representative visual comparison of control vs. actuated self-clearing catheter at the beginning (top) and conclusion (bottom) of the experiment. Scale bar = 1.5 mm.

mmHg) at the end of the circulation (Fig. 4.8b). Compared to the control catheters, we also observed less frequent pressure spikes.

To further quantify the self-clearing catheter performance, we used the differential pressure measurements to calculated the time-to-occlusion (TTO) as defined by the time to reach a threshold pressure and the total time over the threshold pressure (TOT). The threshold pressure of 40 mmHg was determined because intracranial pressure (ICP) exceeding this value is considered life-threatening [182–184]. Fig. 4.9a-b compares the TTO and TOT for each condition. We postulate that TTO indicates how fast the drainage system show functional deterioration due to hematoma whereas TOT indicates resilience of the drainage system to combat blood-clot induced failure. For control catheters, the average TTO was 27 ± 18 min. For treatment cases, average TTO were delayed to 101 ± 121 min for straight devices and 211 ± 72 min for serpentine

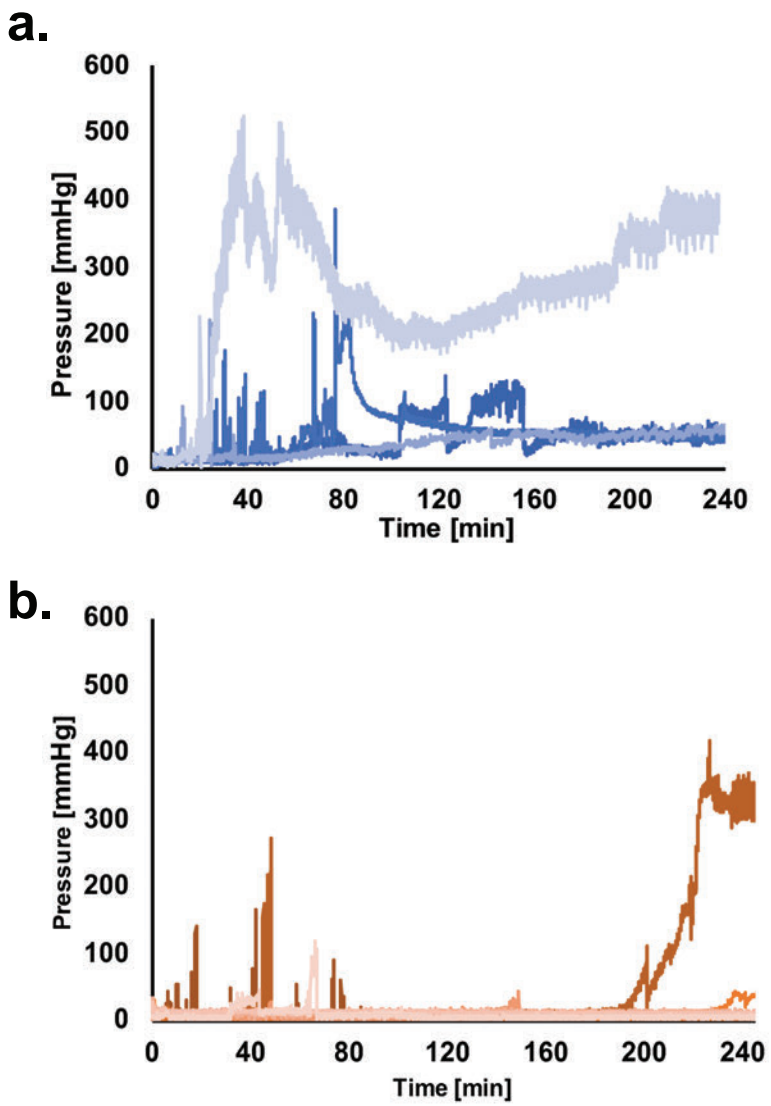

Fig. 4.8. *In vitro* pressure recordings. (a) Differential pressure (P2−P1) recording of all control catheters (n=4). (b) Differential pressure (P2−P1) recording of all self-clearing catheters (n=9). The figure includes data from 3 straight and 6 serpentine devices.

devices. The average TOT for control devices were 161 min. In comparison, average TOT was 11 min for straight devices and 0.3 min for serpentine devices.

These results demonstrate that our self-clearing catheters can significantly delay occlusion due to hematoma and improve device reliability. Moreover, these results confirmed our hypothesis that the larger actuation deflection afforded by the serpen-

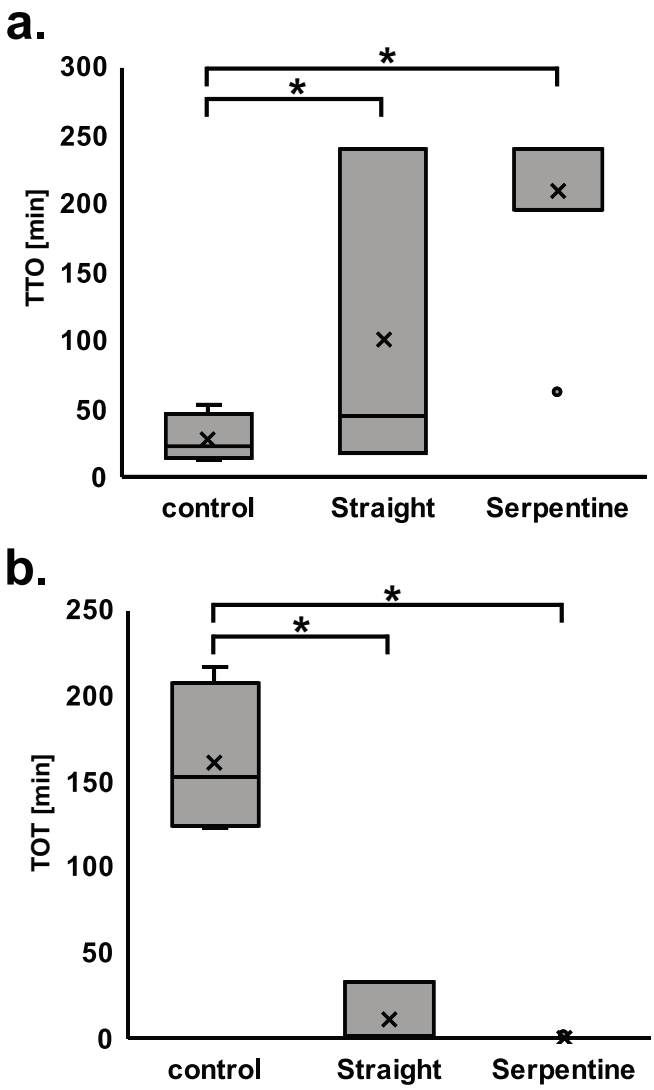

Fig. 4.9. *In vitro* Pressure analysis results. (a) Comparison of time-to-occlusion (TTO) to reach 40 mmHg between control catheter and self-clearing catheters. There were two versions of self-clearing catheters with either straight vs. serpentine flexure microactuators. One-way ANOVA with Tukey post-hoc analysis showed overall statistical significance between groups. Individual comparison and significance ($p < 0.01$) is indicated with *. (b) Comparison of the total time over the threshold (TOT). One-way ANOVA with Tukey post-hoc analysis confirmed statistical significance between groups. Individual comparison and significance ($p < 0.01$) is indicated with *.

tine flexure design can improve blood-clot removal capabilities. We suspect that the rapid translational motion of our microactuators causes localized shear at the catheter inlet, which exceed the threshold above which hematoma becomes incapable to attach and accumulate on catheter surface [185–187]. As a future work, we may be able to use numerical evaluation to estimate the amount of shear stress our microactuators generate in a circulating flow environment.

4.5 *In vivo* evaluation

To verify the results from our *in vitro* experiment, we developed a porcine model of IVH and evaluated the impact of self-clearing catheters *in vivo* (Fig. 4.10 and 4.14). Initially, we performed preliminary studies with 6 pigs to determine the amount of blood to be injected to cause large hematoma in the ventricle and sustained intracranial hypertension (Fig. 4.15). As a result of these studies, we identified 10 ml of blood admixed with 140 units of thrombin immediately prior to injection as a reliable way to cause IVH and subsequent PHH. The blood and thrombin was injected into the right lateral ventricle in 3 equal aliquots.

A total of 13 pigs were used for the evaluation. The median weight was 28.0±3.9 kg. The baseline ICP was 11±5.2 mmHg. As the blood-thrombin injection was paused whenever ICP was ≥50 mmHg, injection was performed over 2 to 15 min (median, 8 min). During injection of the third and final aliquot of blood, ICP would typically immediately increase above 50 mmHg with each injection of about 1 ml, then quickly fall (Fig. 4.16). The ventricular catheter was placed 7.5±7.0 min after the blood-thrombin injection was completed. ICPs reached a high but variable peak, fell quickly initially, then slowly declined to reach a plateau of around 13±4 mmHg. The ventricular catheter was connected to a one-way valve and peritoneal catheter to form a ventriculoperitoneal (VP) shunt.

In all pigs, we used post-operative computed tomography (CT) to confirm accurate intraventricular injection of blood and air. The post-shunting CT also confirmed

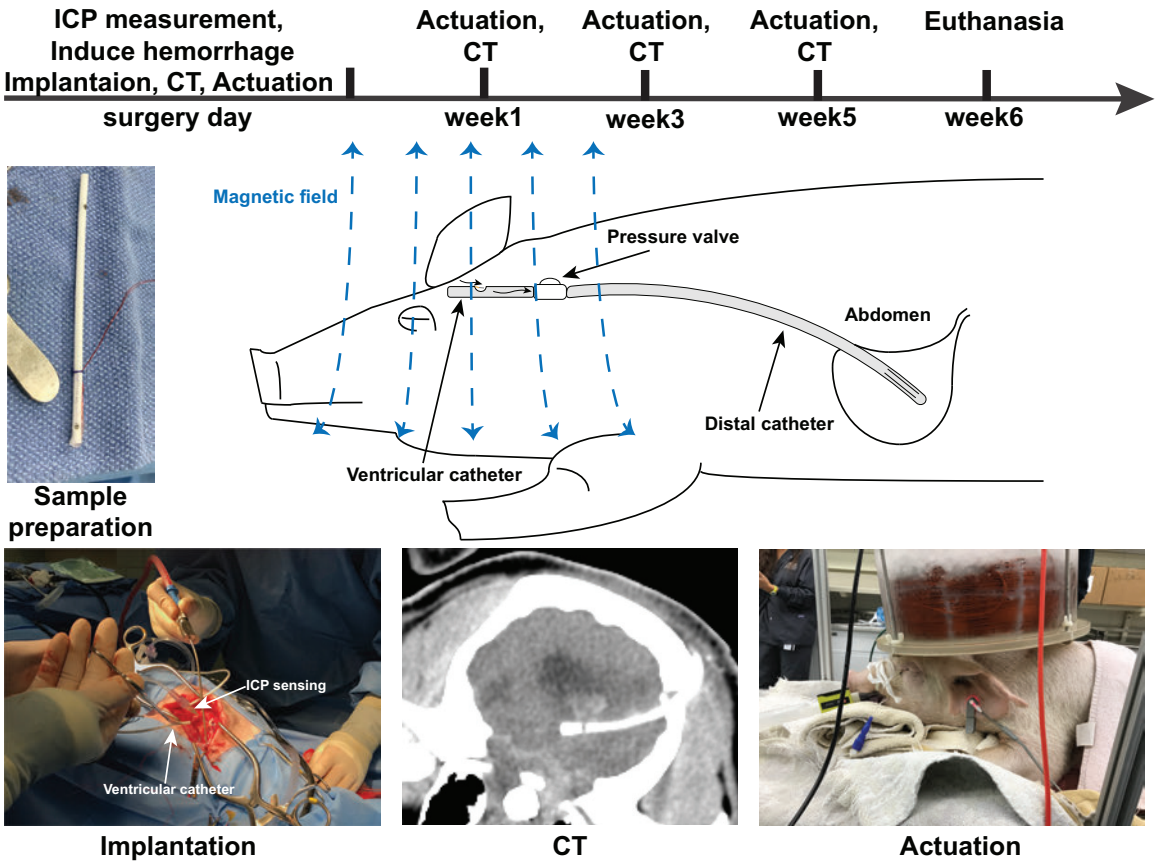

Fig. 4.10. *In vivo* experimental timeline. The entire study is designed to lasts 6 weeks. On surgery day, we induced IVH and implanted a VP shunt. After completion of surgical procedure, CT was performed to confirm ventricular catheter placement. Magnetic actuation (30 min) was performed for the Treated group immediately afterwards. At weeks 1, 3, and 5, each surviving animal was subjected to 30 min of magnetic field and CT scans. All surviving animals were terminated at week 6 for explantation and necropsy.

the correct location of the ventricular catheter. In 1 Control and 1 Treatment pig, we determined that the only inlet pore had passed through the lateral ventricle and into the brain parenchyma. In both of these pigs, we performed a brief second surgery to retract the ventricular catheter and the subsequent CT confirmed the correct ventricular placement of the inlet pore.

All 6 Control pigs suffered sudden neurological decline and were found to have shunts obstructed with hematoma at necropsy.

The sudden neurological decline in the Control pigs occurred 12 h to 5 days post-operatively (median, 3 days). Four of these animals became moribund within hours of the first sign of deterioration, and were euthanized. Post-mortem CT revealed marked enlargement of the ventricles since the post-operative CT, transtentorial with or without cerebellar herniations, and continued correct ventricular location of the ventricular catheter without shunt displacement (Fig. 4.11a).). The other 2 pigs showed sudden, severe but non-fatal neurological decline. The ventricles were markedly larger on the next CT, and for the rest of the study. All explanted VP shunts in the control group showed evidence of hematoma inside their lumen (Fig. 4.17). There were a total of 8 hematomas in these 6 VP shunts (3 ventricular catheter, 3 valvular, 2 distal catheter).

On the contrary, only 1 of 7 Treatment pigs suffered a neurological decline and was found to have a complete shunt obstruction with hematoma at necropsy. The animal deteriorated 12 h post-operatively, rapidly became moribund and was euthanized. This was the pig that had had a second surgery to slightly retract the ventricular catheter, resulting in delayed actuation. Upon post-mortem examination, we found further enlargement of the ventricles and persistence of intraventricular hematoma. Hematoma blocking the push connector (inlet for the valve) was found at necropsy (Fig. 4.18a). The valve itself was filled with sanguineous CSF but was not obstructed. This was the only fatal hematoma in the 7 VP shunts of the Treatment pigs. The ventricular catheters, valves, and the distal catheters were otherwise patent without any evidence of obstructive hematoma (Fig. 4.18b). These observations suggest that

magnetic actuation may be able to preserve the patency of downstream drainage path despite being at the proximal end of the ventricular catheter.

Infection One Control pig suffered from non-fatal shunt obstruction with hematoma at day 4, followed by dehiscence of the wound edges, post-operative infection, and euthanasia. Two Treatment pigs developed fatal infection. One was euthanized at day 7 for peri-operative infection. The other rubbed his head on cage bars post-operatively. The skin edges dehisced and were surgically re-closed at day 5 and again at day 7. Twelve days post-operatively his appetite decreased and 13 days post-operatively he was severely depressed, displayed nystagmus and was euthanized.

In all 3 infected pigs, ventriculomegaly was seen at post-mortem CT, and during necropsy we observed purulent discharge centered around the valve and surgical site, and tracked down the ventricular catheter into the brain. In the two Treatment pigs, the purulent discharge obstructed the inlet pore. In the Control pig, there was also hematoma obstructing the lumen of the ventricular catheter. After two infections in the first seven surgeries, we administered two peri-operative doses of florfenicol to each animal and added a subcutaneous muscle suture layer.

Ventricular volume The post-operative CT in our animals showed significantly larger ventricles than prior to surgery in both groups ($p = 0.002$, Fig. 4.11a). By week 1, all air had been resorbed. In the Treatment group, all hematoma had been resorbed and ventricular size had non-significantly decreased. In the Control group, there had been further enlargement of the ventricles and in some animals hematoma persisted.

Figure 4.11b shows the change in ventricular volume until 1 week post-implantation. Two-way ANOVA showed that statistical significance for both the device type and time. Specifically, the ventricular volume in the Control animals was significantly larger than in the Treatment group ($p < 0.001$). Moreover, the ventricular volume significantly increased before and after IVH and after a week of recovery ($p < 0.001$).

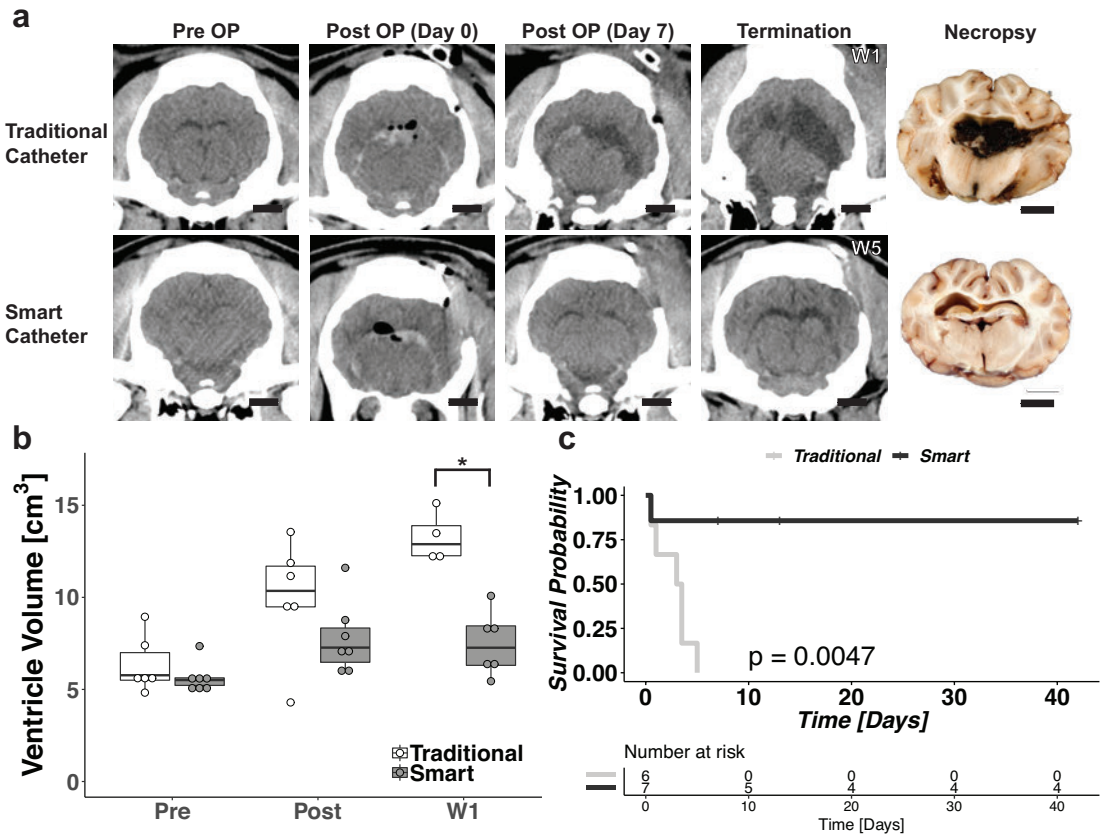

Fig. 4.11. *In vivo* evaluation results. (a) Comparison of CT scans over the course of implantation for animals with traditional catheters (Control) and smart self-clearing catheters (Treated). Note the difference in ventricular volume before and after the surgery. There are signs of air pockets following the surgery (Post Op). After a week, the air pockets are resorbed but there is a significant evidence of ventriculomegaly and hematoma in Control animals. The CT scan of the Control animal show significantly larger ventricle filled with hematoma compared to the Treatment animal. The photograph at necropsy also show the enlarged ventricles. (b) Box plot of ventricle volume until week 1. The extended ventricle volume plot is available in SI Fig. 10. ANOVA indicated significant difference in ventricle volume when treated with smart self-clearing catheters. Control animals with traditional catheters had significant increase in ventricle volume by W1 ($p < 0.001$). (c) Kaplan-Meier survival plot with corresponding risk table. By week 1, the traditional shunt systems in all Control animals had failed where as 80% of the shunt systems with self-clearing catheters remained obstruction-free and neurologically sound with biweekly actuation. Fig. 4.13 shows the survival plot when infections are counted as failures.

Pairwise comparison showed that the by week 1, there was a significant difference in ventricular volume between the Control and the Treatment group ($p < 0.001$).

The data from W3 and W5 was omitted for statistical comparison because all Control shunts failed after week 1. The change in ventricle volume over the entire implantation period are shown in Fig. 4.12. Although the Treatment animals survived longer with our self-clearing catheters, the ventricle volume continued to increase, which may highlights the limitation of our study. This trend suggests that the the self-clearing catheters are prolonging the functional lifetime but we may need to increase the actuation duty cycle to optimize treatment.

Kaplan-Meier survival analysis We performed Kaplan-Meier analysis to evaluate the survivability of the shunt system due to hematoma, censoring death of pigs due to any other reason including anesthesia complication and infection. (Fig. 4.11c). The median shunt survival in the Treatment group was 42 days and the median shunt survival in the Control group was 3 days. This difference was statistically significant ($p = 0.0047$), which further supports our hypothesis that the self-clearing ventricular catheters are more reliable and capable than existing drainage devices. We repeated Kaplan-Meier analysis considering infection as a shunt failure, but the difference still remained statistically significant and the p-value unchanged ($p = 0.0047$, Fig. 4.13), which further supports our hypothesis that the self-clearing catheters may improve the outcomes of IVH and PHH patients.

4.6 Discussion

It is important to note that the prototype drainage devices we tested are at much higher risk of failure than a standard VP shunt. Conventional ventricular catheters typically contain 16 or more inlet pores (3 to 4 rows of 4 to 8 inlet pores) [129]. The catheter we used had a single inlet pore to accelerate occlusion. As such, an occlusion of this lone inlet pore would have led to a complete shunt failure, a circumstance very different to a conventional VP shunt. The single inlet pore also increased the

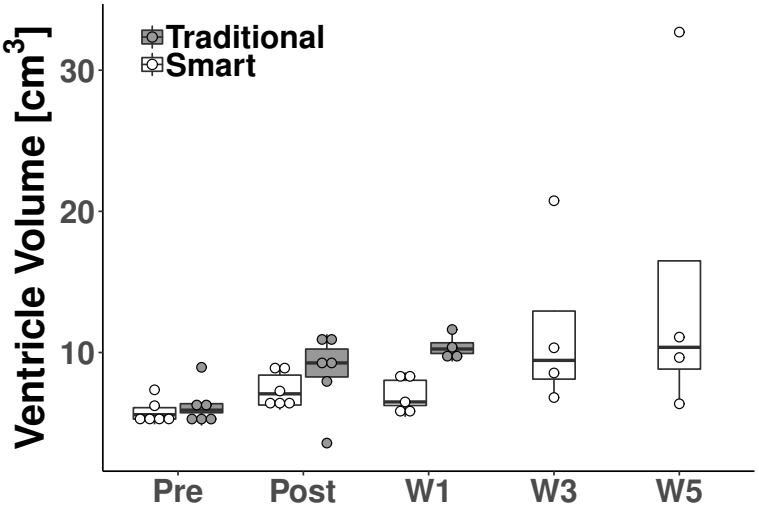

Fig. 4.12. Box plot of ventricle volume for the entire duration of chronic experiment. Note that the ventricle volume continued to increase in Treatment group, which may suggest a more frequent actuation may be needed over an extended period.

chance of inadequate surgical placement: the rows of inlet pores in conventional catheters maximize the likelihood that multiple inlet pores will be located in the lateral ventricle. In one Treatment pig, the post-operative CT indicated that the single inlet pore was too deep (passing through the ventricle and into brain tissue on the other side) and led to additional surgery and most importantly delayed actuation. All other Treatment shunts were first actuated soon after placement, and subsequently remained free of hematoma obstruction throughout the 6-week study. This Treatment shunt was not actuated until after a second surgery to retract the ventricular catheter, and was fatally obstructed in less than 24 h. Upon explantation, we found that the hematoma had passed the microactuator within the tip of the ventricular catheter and was at the junction of the ventricular catheter and valve, suggesting the first actuation may not have occurred until after overwhelming hemorrhage had already passed the actuator.

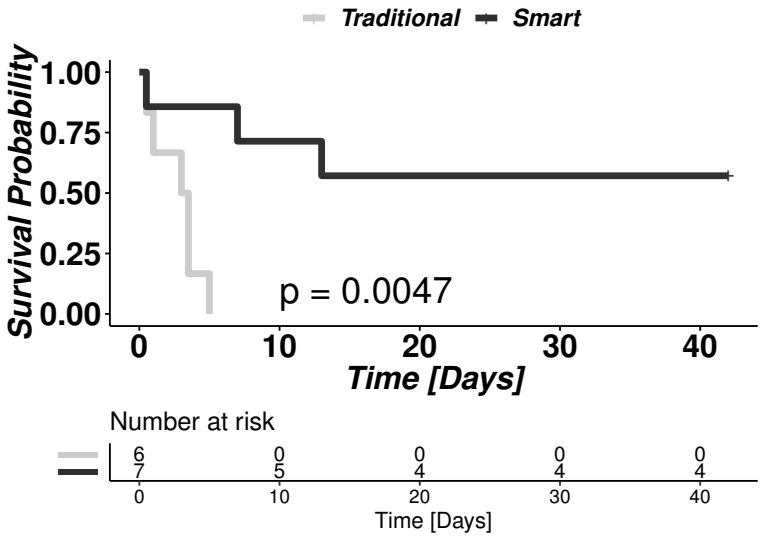

Fig. 4.13. Kaplan-Meier survival plot with corresponding risk table when infections are counted as failures. By week 1, the traditional shunt systems in Control animals had failed where as more than 50% of the shunt systems with self-clearing catheters remained hematoma-free with biweekly actuation. The p-value did not change and the difference remained statistically significant.

There was additional risk of failure as the catheter was placed directly into the ventricular hematoma, through the tract used for injection of blood, being inserted immediately after the injection was completed. The blood was mixed with the coagulant agent thrombin. A mixture of CSF, hemorrhage, and thrombin therefore immediately entered the shunt system and began coagulating. Additionally, we used low opening pressures valves (2.2 mmHg). The typically used valve in VP shunt surgery has a medium opening pressure (6–7 mmHg), within the range for normal ventricular pressure of 5–15 mmHg. The low opening pressure would have increased the passage of hemorrhagic CSF through the VP shunt, as the coagulating fluid would have taken the path of least resistance rather than negotiate the ventricular system. Hemorrhage present within the ventricular system (e.g. foramen of Munro) would have been able to form a permanent thrombus, rather than being dislodged by CSF flow.

Our model recreated the forms of hydrocephalus most prone to failure in human patients. Obstructive hydrocephalus, as in our model, is at the highest risk and suffers shunt failure significantly more commonly than communicative or normal-pressure hydrocephalus [188]. Cerebral hemorrhage and post-traumatic hydrocephalus are also at significantly higher risk of shunt failure than idiopathic hydrocephalus [188]. Additionally, the injection of blood provides a substrate for bacterial growth. Neonates with PHH suffer from shunt failure due to infection in as many as 71% of cases [189]. Although our microactuators did not prevent failure due to infection, the use of antibiotic-impregnated catheters is associated with significantly less post-operative infections [189]. A combination of microactuators and antibiotic-impregnated catheters may be used to potentially overcome the most common modes of shunt failures.

4.7 Materials and Methods

4.7.1 Device fabrication

The microactuators were fabricated in a standard cleanroom environment. Starting from a 100 mm p-type single-side polished silicon wafer (Silicon Quest, San Jose, CA), 50 nm of silicon dioxide was deposited by plasma enhanced chemical vapor deposition (Axic, Milpitas, CA) to function as a release layer. Next, a layer of polyimide PI-2525, HD Microsystem, Parlin, NJ) was spun coated at 1750 rpm and cured in nitrogen oven up to 350 °C to create a final thickness of 11 μm. A 50-nm-thick Cr was evaporated (Airco E-Beam Evaporator, Livermore, CA) as the etch mask for the polymer layer. Cr mask was photo-patterned using AZ9260 (Microchemicals, Germany) and etched using a Cr etchant (Cr-16, KMG, Fort Worth, TX). The polyimide structural layer was etched using O_2 plasma at 20 sccm, 50 mTorr and 150 W RF power (Advanced Oxide Etcher, Surface Technology System, Newport, UK). Cr mask was then removed using Cr-16.

Next, 100 nm of Au was sputtered (PVD, Wilmington, MA) globally as a conduction layer and 200-μm-thick electroplating mold was photo-patterned using a negative

photoresist (BPN-65A, Rohm Haas, Marlborough, MA). The nickel ferromagnetic elements were in 2L plating solution maintained at 60 °C with 40 mA direct current for 4 h. The plating solution contained 1 M nickel sulfamate, 0.4 M boric acid and 10 g sodium dodecyl sulfate. The electroplated elements varied from 80–130 μm in thickness depending on the actuator geometry. Afterwards, the exposed Au conduction layer was stripped using a wet etchant (GE8148, Transene, Danvers, MA). The microactuators were released from the wafer using a buffered oxide etchant (Fisher Scientific, Waltham, MA). To create the self-clearing catheter, the released sample were rolled and inserted into a catheter lumen (Model G0664, Cook Medical) as previously described [105].

4.7.2 Finite element analysis

COMSOL Multiphysics (V5.0, COMSOL, Inc., Burlington, MA, USA) was used for the finite element analysis of device deflection and stress distribution. Each device design was configured to have the material property of polyimide with a density of 1300 kg/m^3, Young's modulus of 2.45 GPa and poison ratio of 0.3. Using the solid mechanics module, each flexure was fixed on one end and a vertical point load ranging from 1-100 μN were applied to the free end to evaluate the static deflection and the stress distribution. Lagrange strain was used to account for the large flexure deformation.

4.7.3 Static response

The microactuators were positioned along the long axis of a bespoke solenoid electromagnet (cylindrical permalloy core, 1-in-diameter and 6-in-tall with 300 turns) and down to the edge of a glass slide. The distance between the sample and the electromagnet surface was kept at 7 mm to minimize magnetic field spacial gradient (<0.1 T/m) while maintaining adequate amount of parallel magnetic field strength. A DC power source (PWS 2326, Tektronix, Beaverton, Oregon) was used to supplied the

current to the electromagnet. The amount of magnetic flux density at the position of actuators were measured using gaussmeter (8010, F.W. Bell, Milwaukie, OR). During actuation, the electromagnet along with actuator positioning glass slides were placed horizontally and the amount of deflection angle was optically measured using a digital SLR camera (Canon 50D, Huntington, NY). The magnetic flux density was varied from 0–22 mT for straight beamed device and from 0 mT to 17 mT for serpentine device.

4.7.4 *In vitro* evaluation

A 50 ml glass bottle (Duran, Fisher Scientific, Waltham, MA) was used mimic the ventricular chamber. The bottle was sealed using a screw cap with two through holes allowing placement of the inlet and outlet tubing(L/S 14, Masterflex, Cole-Parmer). A piece of central venous catheter (Model G0664, Cook Medical) was attached to the outlet inside the glass bottle chamber. The through holes on the screw cap was sealed using a silicone adhesive to fix the tubings in place. A variable speed peristaltic pump (7523-50, Masterflex, Cole Parmer) was used to drive fluid into the chamber at 1.4 ml/min, about twice the rate of average cerebral spinal fluid production in humans [112, 149, 190]. Two pressure sensors (PRESS-S-00, PendoTech, Princeton, NJ) were connected to the inlet and the outlet tubes.

A mixture of porcine blood and 1X PBS (Fisher Scientific, Waltham, MA) at 50:50 vol was used to mimic hemorrhagic cerebrospinal fluid. A fresh blood euthanized pigs was mixed with 10 USP units of heparin/ml and stored in a refrigerator at 4 °C for 1 week prior to the experiment. At the time of testing, protamine sulfate (Fisher Scientific, Waltham, MA) was added (10 mg per 100 USP heparin) to reverse the effects of anti-coagulant and to facilitate blood clot formation [191]. Since conventional catheter occlusion is unpredictable with wide range of time to failure [5, 192], a layer of fibrin matrix gel was applied on the catheter surface surrounding the inlet pore to further promote blood clots attachment. The fibrin gel was made from a mix-

ture of fibrinogen (38 mg/ml) and thrombin (37 mg/ml) (Thermo Fisher Scientific, Waltham, MA) [193–195].

Each device was subjected to 4 h of circulation in the circulating setup during which the differential pressure was recorded continuously (12 samples/min). For Control group, single-pore catheters without any microactuators were tested ($n = 4$). For Treatment groups, self-clearing catheters with either straight ($n = 3$) and serpentine flexure designs were tested ($n = 6$). During each experiment, the time-varying magnetic field was applied using a permanent magnet (McMaster-Carr, Elmhurst, IL) affixed to a DC motor from 20 mm away spinning at 8 Hz. The magnetic performance of this motorized setup is shown in Fig. 4.23. Using the differential pressure recording, the time to reach a threshold pressure (i.e., time to occlusion, TTO) and the time over a threshold pressure (TOT, 40 mmHg) was calculated. The TTO and TOT for different conditions were compared using one-way ANOVA with Tukey's HSD post-hoc analyses with $p < 0.05$ as statistical significance.

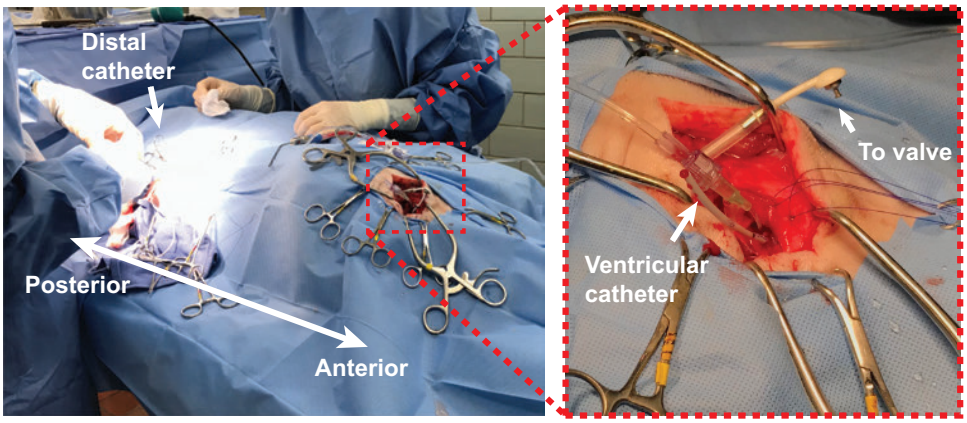

Fig. 4.14. Sterile surgical setup for the intraventricular hemorrhage and the implantation of a shunt system in a porcine model. Inset: A zoomed image of the surgical site showing the ventricular catheter prior to being connected to a pressure valve.

4.7.5 *In vivo* evaluation

For the *in vivo* evaluation, 13 cross-bred domestic swines weighing 25.0–31.6 kg were used. Each pig was pre-medicated with 0.2 mg/kg midazolam (Hikma Pharmaceuticals USA Inc, Eatontown, NJ) and 0.03 mg/kg dexmedetomidine (Zoetis US, Parsippany, NJ, USA) and induced with isoflurane delivered by face mask until tracheal intubation was possible. Anesthesia was continued with isoflurane delivered in 100% oxygen. Mechanical ventilation, pulse oximetry, capnography, indirect blood pressure measurement, temperature measurement, left jugular central line placement and intravenous fluid therapy (10 mL/kg/hr) were performed. Analgesia was provided by pre-operative transdermal application of 2.7 mg/kg fentanyl solution (4 day expected activity) (Elanco Geenfield, IN). Intramuscular injection of 5 mg/Kg ceftiofur (7 day expected activity) was used for antibiotic treatment.

To induce intraventricular hemorrhage, a right side subtemporal craniectomy was performed using standard aseptic technique. To measure intraventricular ICP, a 1.25-inch 18-gauge intravenous cannula was directed through intact dura mater into the right lateral ventricle. Correct ventricular location was confirmed by drainage of CSF. Non-compliant tubing (pre-filled with saline) was connected tightly and attached to a transducer and monitor. To inject the blood-thrombin mixture, a second 1.25-inch 18-gauge intravenous cannula was then placed into the lateral ventricle, more rostrally. Drainage of CSF again confirmed accurate placement. A total of 10 ml of autologous blood and 140 units thrombin was injected through this cannula as determined using preliminary studies. Blood was drawn from the jugular catheter using sterile technique in 3 equal aliquots. Each aliquot was briefly agitated with thrombin in a syringe and then injected. Each time ICP rose above 50 mmHg, injection was paused until ICP was <50 mmHg. This second cannula was then withdrawn.

The puncture hole in the dura mater was slightly enlarged with a #11 scalpel blade, and the ventricular catheter was inserted through the tract that had been used for blood injection. In 6 pigs, a Control VP shunt was placed. The ventricular

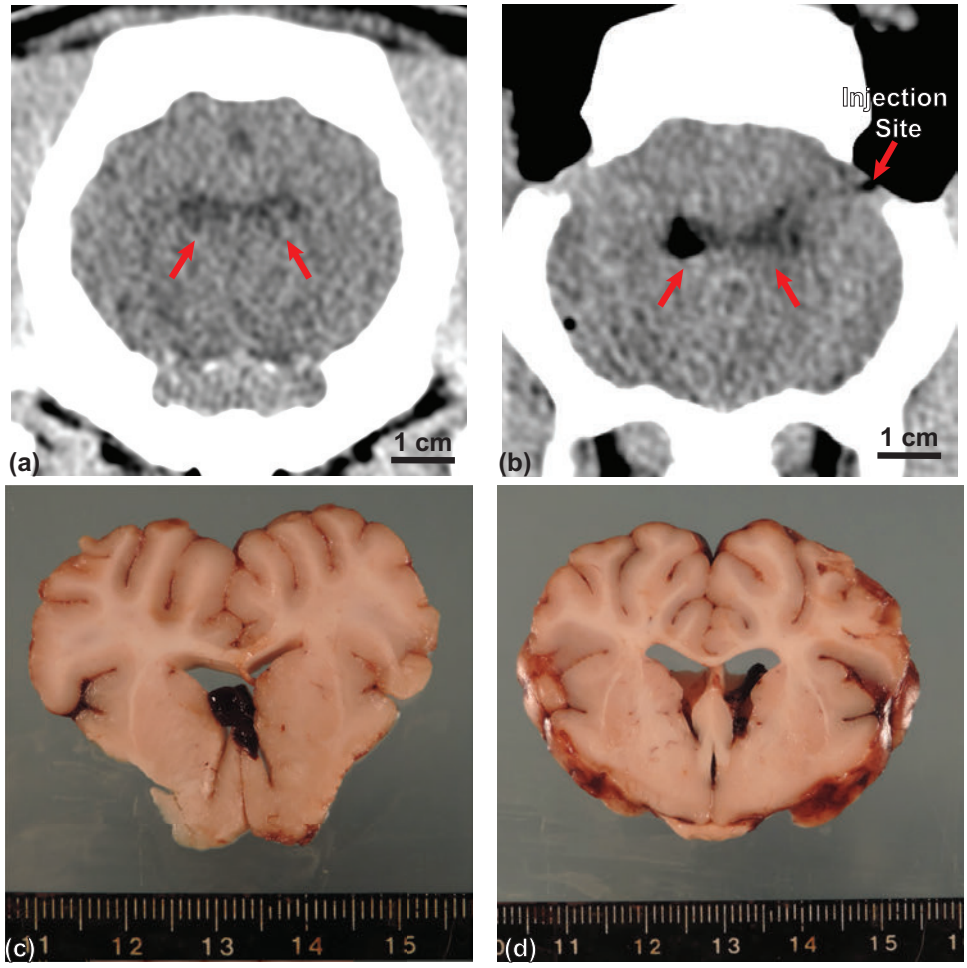

Fig. 4.15. Induction of intraventricular hemorrhage. The (a) pre- and (b) post-operative CT scans of the animal that shows grossly enlarged ventricle. Note the visible tract into the right lateral ventricle that was used to inject autologous blood. (c) Post-mortem sections of cerebral cortex showing enlarged right ventricle. Note the deviated septum pellucidum and the presence of large hematoma in the right ventricle. (d) Bilateral enlargement in the body and the temporal horn of lateral ventricles. Note the hemorrhage present in the left ventricle and in the cerebral aqueduct.

catheter was custom-made for this study using a modified central venous access device (Cook Model G0664, Bloomington, IN), with only one single inlet pore. In 7 pigs, a Treatment shunt was placed. The custom-made ventricular catheter had a single inlet pore and a microactuator placed at the inlet pore [105]. Correct ventricular location

was confirmed by rapid drainage of sanguineous CSF. ICP recording was continued until 30 min after placement of the ventricular catheter.

The ventricular catheter was anchored to the skull by a pre-placed polydioxanone suture (Ethicon, Somerville, NJ) through the periosteum and loose fascia. It was connected to a pre-placed low-pressure valve (Integra Lifesciences, Plainsboro, NJ) and distal catheter which had been filled with saline, creating a VP shunt. The valve was anchored to the periosteal tissue of the posterior skull by a suture that encircled the connection of the ventricular catheter to the valve. The valve was pumped, and functionality of the VP shunt was confirmed by sanguineous CSF entering the valve and saline escaping from the distal catheter. The distal catheter was placed in the peritoneal cavity and the paracostal incision closed. The fascia of the temporalis muscle was closed with a simple continuous polydioxanone suture.. The skin was closed with simple continuous subcuticular and intradermal poliglecaprone sutures (Ethicon), followed by the application of skin glue.

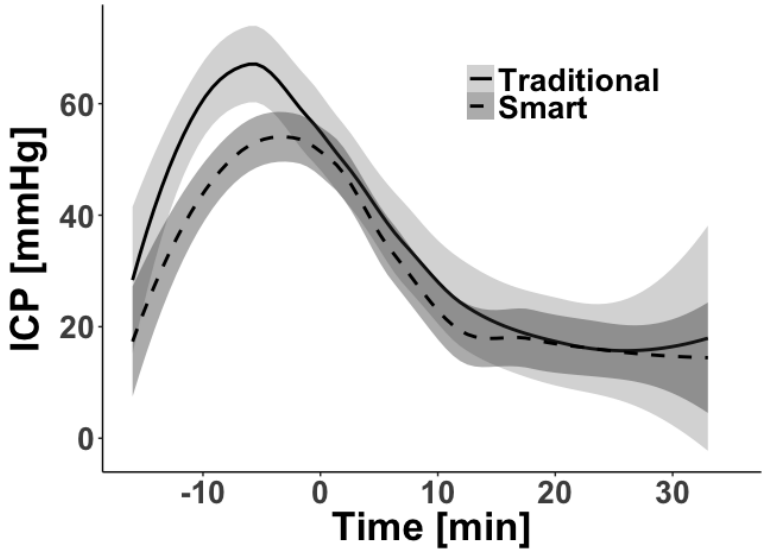

Fig. 4.16. Measurement of intracranial pressure (ICP) during injection of autologous blood. To induce intraventricular hemorrhage, 10 ml of autologous blood was injected. Time = 0 indicates the point when the entire volume was injected. Note that the ICP remained abnormally high regardless of which catheter type was used.

Computed tomography was performed prior to and immediately following surgery (day 0). In the Treatment group, actuation was performed immediately after post-operative CT for 30 minutes using a bespoke electromagnet (Fig. 4.27). Pigs were then recovered from anesthesia. Repeat CT was performed at weeks 1, 3, and 5. Pigs were again premedicated with 0.2 mg/kg midazolam and 0.03 mg/kg dexmedetomidine, then had oxygen and isoflurane delivered by face mask throughout the CT. In the Treatment group, repeat actuation was performed immediately after each CT. The first CT was 5 to 7 days post-operatively, so that the first actuation was performed at day 5 or 6 in the Treatment group.

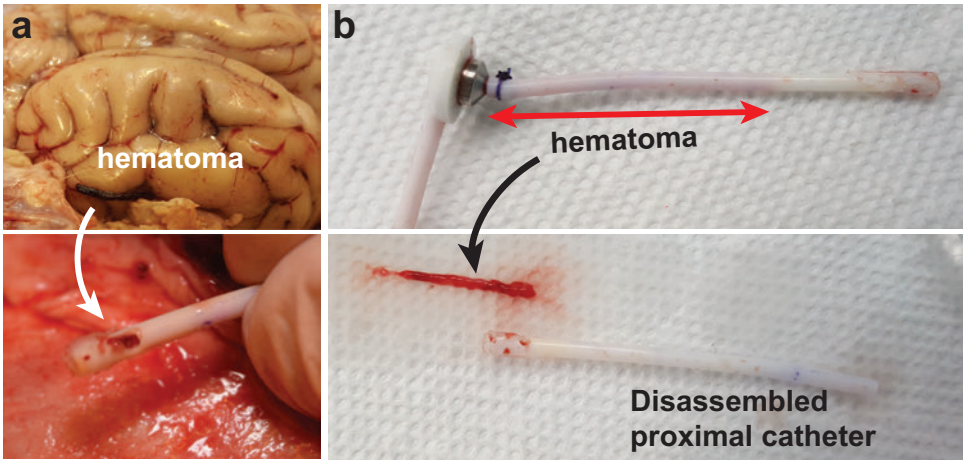

Fig. 4.17. Photographs of explanted failed control catheters. (a) The explanted control ventricular catheter showed complete blockage in its inlet poor with hematoma. When pulled out of the brain, a long track of blood clot was pulled out from the catheter. (b) When the shunt system was dissembled, a fresh hematoma was found, which suggests that this device was completely occluded.

The size of ventricles were measured using a DICOM viewer (Osirix Lite 10.0.1, Pixmeo SARL Bernex, Switzerland). The ventricle (i.e., region of interest) from each CT scan was outlined manually by three measurers. The volume of outlined region of interest was calculated by the DICOM viewer and compared (Fig. 4.19). One-way ANOVA with Tukey's HSD post-hoc analysis showed no statistical significance between the three measurers ($p = 0.095$). To compare the difference in ventricle

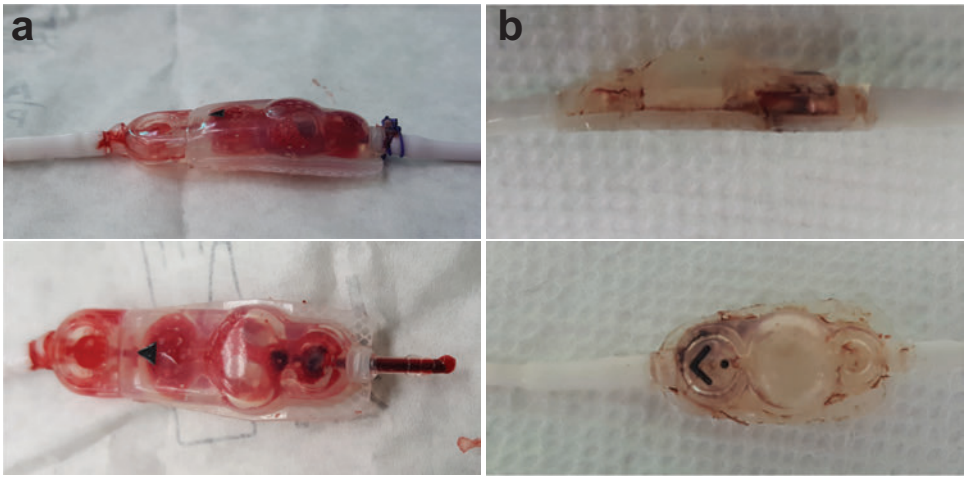

Fig. 4.18. Explanted pressure valves for treated groups. (a) Photograph of the explanted pressure valve from the Treatment animal that perished on the day of surgery. We found that the push connector portion was blocked with hematoma. This animal had a revision surgery due to initial mis-position of the catheter into the cortex. (b) Photograph of an explanted pressure valve from a Treatment animal that survived the entire 6 week duration. We saw that the valve was patent without any evidence of large hematoma.

volumes in Treatment vs. Control group, two-way ANOVA was performed to see the effects of time and the type of catheters. A post-hoc pairwise comparisons were made using Tukey's HSD test.

Kaplan-Meier analysis of shunt survival was used to compare Treatment and Control groups. Obstruction of the shunt by hematoma was considered an event. Both for fatal shunt obstructions and for non-fatal shunt obstructions causing neurological decline, increasing size of the lateral ventricles on CT and confirmation of shunt obstruction by hematoma at necropsy when pigs were sacrificed at day 42. Death of the pig due to any other reasons (e.g., anesthesia complication, infection) was censored.

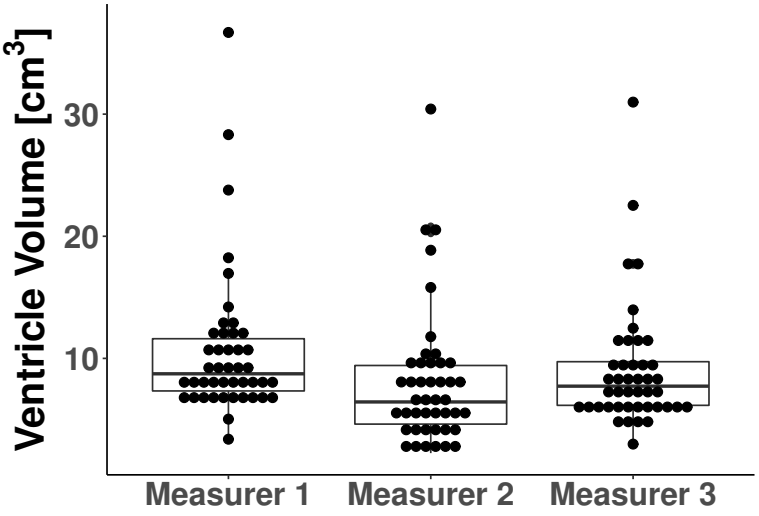

Fig. 4.19. Comparison of ventricle volume measured by three separate measurer. One-way ANOVA indicated no significant differences between the three individuals ($p = 0.095$)

Table 4.1.
Design dimensions

Type	Straight	Serpentine
Beam length [μm]	600	3000
Beam width [μm]	75	55
Beam thickness [μm]	11	11
Tip volume [$\times 10^{-3}$mm^3]	46	40
Ni thickness [μm]	130	80
Ni long axis [μm]	775	905
Aspect ratio	5.9	11.3

4.8 Magnetic modeling and characterization

4.8.1 Analytical modeling of static response

Magnetic properties characterization After magnetic actuators were fabricated, the magnetic properties of electroplated nickel were evaluated using a SQUID magneto

Table 4.2.
Dimensions as measured (Data expressed as mean ± s.d., n=3)

Type	Straight	Serpentine
Beam length [μm]	595±1.5	2676±18
Beam width [μm]	74.7±0.4	56.8±1.1
Beam thickness [μm]	11.25±0.08	11.16±0.06
Tip volume [$\times 10^{-3}$mm^3]	46±2.4	43±1.6
Aspect ratio	5.9±0.29	10.6±0.38

meter (MPMS-3, Quantum Design, Inc., San Diego, CA, USA). Saturation magnetization, coercivity, remanence, susceptibility and overall hysteresis of the electroplated nickel elements were used to predict magnetic torque produced and to provide guidance for optimizing the applied magnetic field. A sample of serpentine flexure device was cut so that only nickel structure and cantilever remained. The long axis of the sample was aligned to the moving direction of the test stage and the external magnetic field direction. For measuring saturation, the sample was tested from -1 to 1 T. High field saturation loop indicated that the electroplated nickel saturates at 200 KA/m with saturation magnetization of 0.75 T (Fig. 4.20a). A low field hysteresis loop was also captured from -30 to 30 kA/m to get a better resolution on critical points across axes. Minimum hysteresis was observed and Fig. 4.20b shows the coercivity of 2 KA/m and remanence of 0.037 T. The magnetization varied almost linearly with respect to the field strength at low field range. The magnetic susceptibility (χ) was 11.3.

The AC susceptibility was tested to characterize how well the magnet responds with the external sinusoidal excitation. At 0 T DC bias, the sample was exposed to 1 mT sinusoidal magnetic filed. The driving frequency varied from 7 to 550 Hz and the corresponding AC susceptibility (χ', χ'' [emu/Oe]) was measured. The magnitude (M/H, unit-less) and the phase angle (degrees) were then converted. The results in-

dicated less than 2% variation in susceptibility and less than 0.7° phase lag across the tested frequency range. This suggests that the direction of magnetization turns almost instantaneously with respect to the external sinusoidal signal while the magnitude of magnetization remains constant within our actuation frequency (<100 Hz).

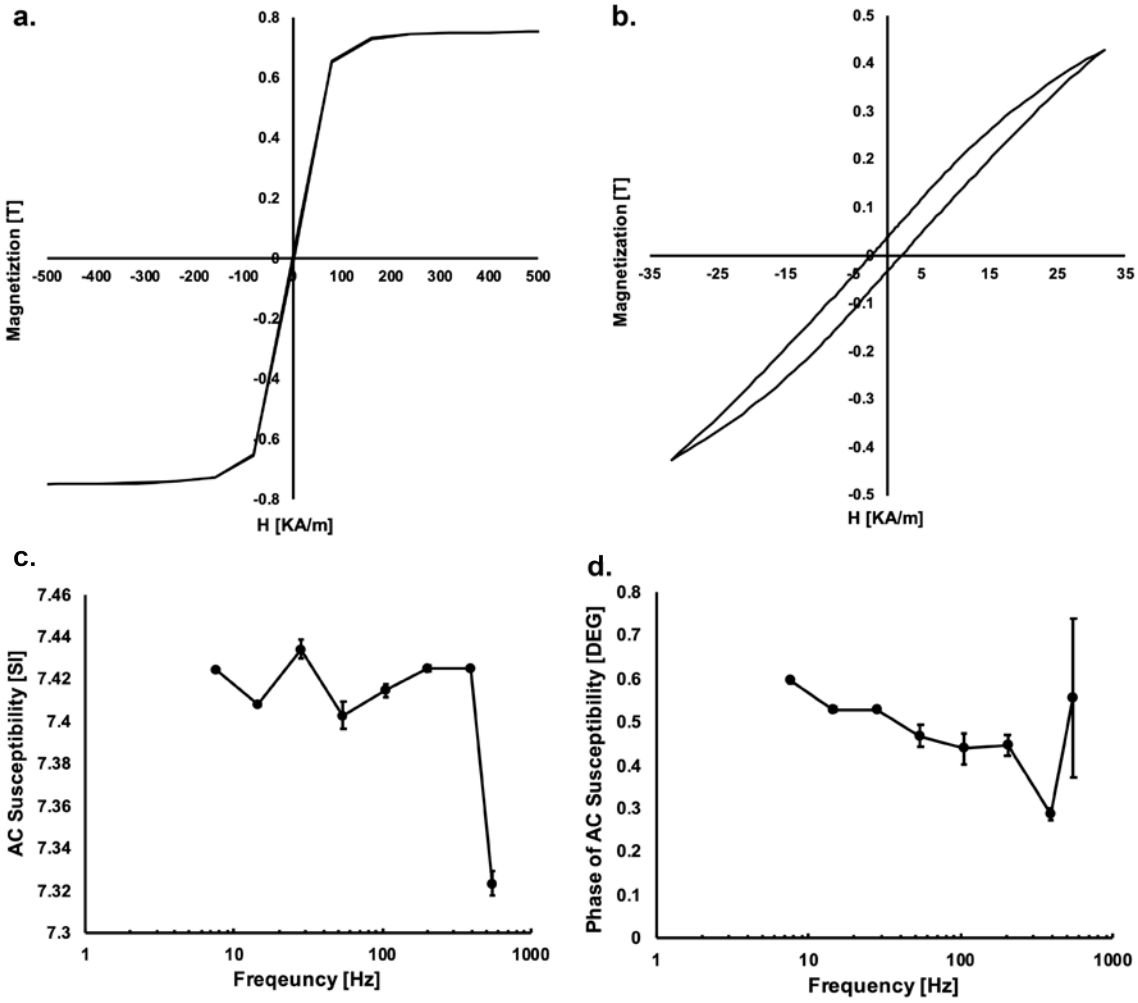

Fig. 4.20. Magnetic characterization of electroplated nickel. (a) M-H loop within high field range. (b) M-H loop within low field range. (c) Magnitude of AC magnetic susceptibility from 7 to 550 Hz. d. Phase of AC magnetic susceptibility from 7 to 550 Hz.

Magnetostatic torque In the presence of uniform magnetic field, magnetic material experiences magnetic torque given by $\vec{\tau_m} = \mu_0 v \vec{M} \times \vec{H}$ where $\vec{M}$ is magnetization, μ_0 is magnetic permeability of free space, v is volume and $\vec{H}$ is external magnetic field. For hard magnetic material (i.e., permanent magnet), the magnetic torque can easily be estimated by applying the saturation magnetization value if the variation of external field is within coercivity. Ferromagnetic material such as electroplated nickel, however, is magnetically soft. Both the direction and the magnitude of magnetization vary as a function of the applied magnetic field amplitude and the magnetic anisotropy. An improved model based on Judy [102] and Abbott [196] is therefore developed to better describe the magnetic torque and the motion of magnetic actuator with polyimide flexure. If a uniform magnetic field H_a is applied along one axis, the internal magnetic field H experiences by nickel is given by $H = H_a - N_d M$. Demagnetization factor N_d describes how strong the internal field is reduced along the given axis due to the geometric anisotropy [197]. The demagnetization factors have been solved analytically for ellipsoid geometry and the values for other geometries have been extensively studied [198–201]. Here, the demagnetization factor of an oblate spheroid was used. The value of N_d depends on the aspect ratio between lengths of long axis and thickness (Table 4.2) With a higher aspect ratio, we can expect the N_d become larger for the specified axis. Introducing the magnetic susceptibility $\chi = \frac{M}{H}$ and acknowledging the fact that M reaches to magnetic remanence M_r when H_a is removed, the magnetization has the form of:

$$M = \frac{\chi}{1 + \chi N_d} H_a + M_r. \tag{4.1}$$

In 3 dimensional cartesian coordinates, magnetic torque is therefore described by:

$$\vec{\tau_m} = \mu_0 v \begin{bmatrix} \frac{\chi}{1+\chi N_x} H_x + M_r \\ \frac{\chi}{1+\chi N_y} H_y + M_r \\ \frac{\chi}{1+\chi N_z} H_z + M_r \end{bmatrix} \times \begin{bmatrix} H_x \\ H_y \\ H_z \end{bmatrix} \tag{4.2}$$

During magnetic actuation the applied field was positioned in a way that there was no horizontal component perpendicular to the length of cantilever (Fig. 4.2, Fig.

4.6). Only x and z components of magnetization remain and the angle between the net magnetic field H and the shortest axis of the magnet is θ. Assuming the sample is previously magnetized along the long axis x and M_r remains only along x direction, then the magnetic torque can be calculated by:

$$\vec{\tau_m} = \mu_0 v \begin{vmatrix} \hat{a_x} & \hat{a_y} & \hat{a_z} \\ \frac{\chi H sin\theta}{1+N_x\chi} + M_r & 0 & \frac{\chi H cos\theta}{1+N_z\chi} \\ Hsin\theta & 0 & Hcos\theta \end{vmatrix} \tag{4.3}$$

$$\vec{\tau_m} = \mu_0 v(-\frac{\chi H^2 sin\theta cos\theta}{1+N_x\chi} - M_r H cos\theta + \frac{\chi H^2 sin\theta cos\theta}{1+N_z\chi})\hat{a_y} \tag{4.4}$$

and the rotation produced by mechanical torque is along y axis as shown in equation 4.4. Notable differences between this model and model from [102, 196] are the inclusion of observed magnetic remanence and the finite susceptibility. This mathematical model suits our application for the case when the device operates at linear region in the hysteresis loop.

Static deflection angle of polyimide-based magnetic actuator can be calculated by balancing the magnetic torque from the ferromagnetic element and mechanical torque from the flexure [99]. Considering a magnetic field fixed in z direction and structural plate is only rotating along x-z plane, the relation $\tau_k = k\theta$ was previously used for predicting amount of mechanical torque required to produced transverse bending angle θ of a straight beam with rectangular cross section [105, 117]. A modified relation is used to account for an initial angle θ_i produced from residual stress of a polyimide film from thermal curing [202].

$$\tau_k = k(\theta + \theta_i); k = \frac{Ewt^3}{12L} \tag{4.5}$$

E is modulous of elasticity of polyimide, w, L, t are cantilever width, length and thickness respectively. By equating equation 4.4 and equation 4.5, static deflection angle θ as a function of magnetic field strength H in z direction is calculated. Fig. 4.21 shows improvement of predicted static deflection from the new torque model.

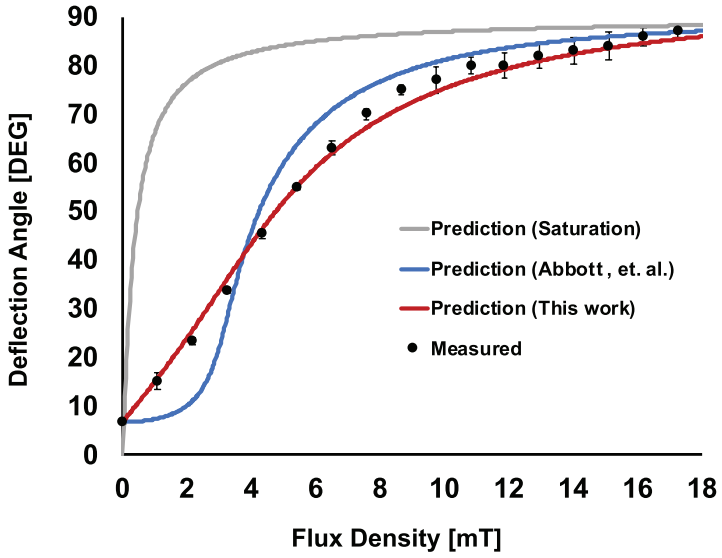

Fig. 4.21. Measured static deflection angle in comparison to predictions from saturation estimation, model from Abbot et al. and this work.

4.8.2 Dynamic response of magnetic actuator

AC mechanical response of magnetic actuator with serpentine cantilever was characterized to determine the optimum actuation frequency. The device was fixed in a transparent evaporation dish filled with DI water. A bespoke electromagnet was placed above the device for supplying time-varying sinusoidal magnetic field. A high speed camera (Chronos 1.4, Kron Technologies, Inc. Barnaby, BC, Canada) was positioned horizontally to image and record vertical deflection of the ferromagnetic element (Fig. 4.22a). Actuation frequencies from 3.5 to 60 Hz were applied and for each frequency the magnitude of vertical H field was adjusted at 15 mT, the amount

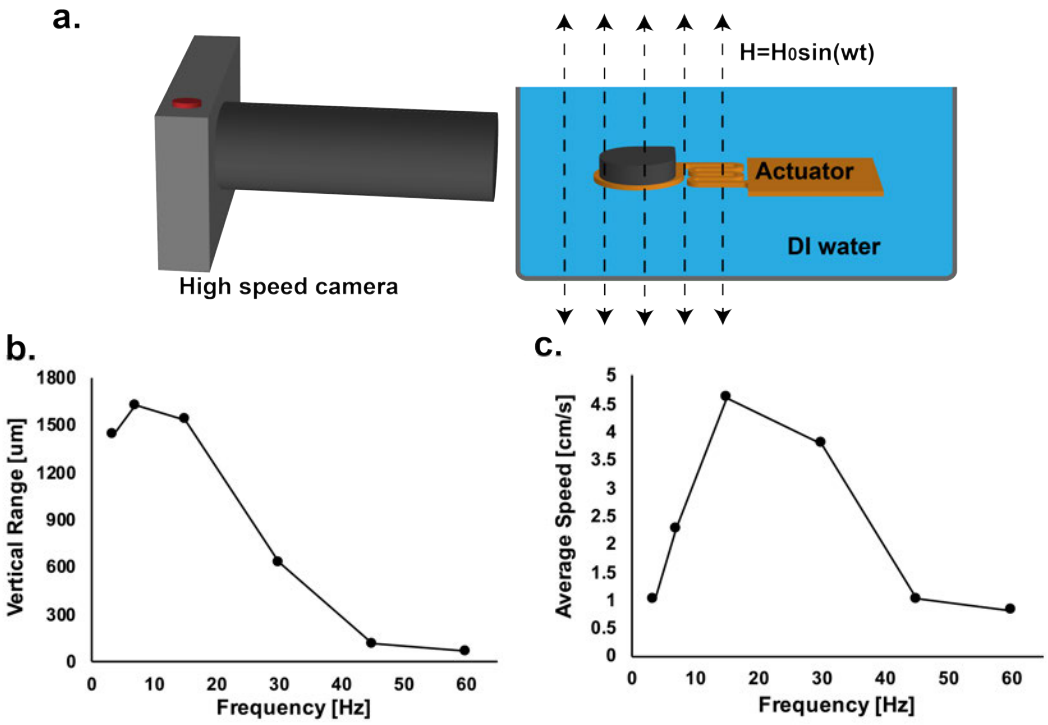

Fig. 4.22. (a) Schematic illustration of dynamic response of the serpentine actuator in DI water. (b) Vertical deflection range as a function of frequency. (c) Average speed at outer edge of the actuator as a function of frequency.

determined from the DC analysis. High speed footages were analyzed for each actuation frequency frame by frame. Position of the outer edge of the ferromagnetic element on the actuator was measured. The vertical deflection range was calculated by subtracting a highest and a lowest point ever reached by the actuator. The results indicate a response similar to behavior of a low pass filter. Deflection range maintained at around 1.7 mm until 15 Hz and then quickly reduced to 60 μm at 60 Hz due to liquid damping (Fig. 4.22b-c). The average speed during one actuation cycle was also calculated for each frequency. A peak speed of 4.5 cm/s was produced between 10 to 15 Hz. In order to produce large deflection and maintain high speed at the same time, an actuation frequency of 15 Hz or smaller should be considered.

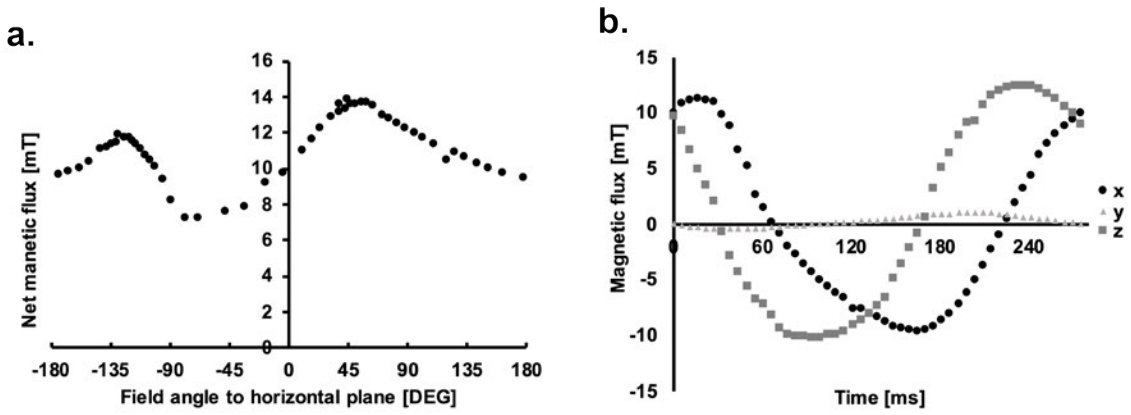

Fig. 4.23. Magnetic field characterization for *in vitro* experiment. (a) Net magnet flux density actuator experienced at each angle to horizontal plane. (b) Magnetic flux density actuator experienced in 3 axis from one period of revolution.

4.8.3 Magnetic flux density during the *in vitro* experiment

A spacial and time varying magnetic field generation setup was made to deliver maximum torque for each actuation cycle. Typically, a multi-coil system is used to provide such H pattern in AC. However, since our frequency of interest is under 100 Hz, a spinning neodymium magnet was utilized for its simplicity. A one-inch wide, half-inch-thick circular neodymium disk magnet was housed inside a 3D printed fixture connected to a driving shaft driven with a DC motor (Fig. 4.6). The neodymium magnet was oriented in a way that H field was minimum in the y-axis. The direction of H changed in a circular fashion in x-z plane each cycle. Each actuator was placed approximately 3.5 cm below and 2 cm away from the Nd magnet such that the maximum magnetic flux density was 14 mT (Fig. 4.23). The effective frequency of 8 Hz (240 rpm from motor) was selected for maximum deflection range and motor stability.

4.8.4 Electromagnet for the *in vivo* experiment

In order to deliver required amount of magnetic field to actuators at ventricle of animals, an electromagnet was designed and fabricated. Typically, a super conductor is used for generating magnetic field for penetrating human body because magnetic field attenuates as distance squared. However, adopting a superconductor with helium cooling is outside the budget and scope of the study. Therefore, multiple windings of copper wires was utilized to pack current NI in unit volume for increased field generation. A multilayer air core solenoid layout was chosen because of its ability to generate relatively uniform field strength within the cylinder. Fig. 4.24 shows a schematic of such electromagnet in relative to animal head. The first orientation has the head inside the coil so that maximum strength is experienced in parallel direction. The second orientation has the coil suspended on top of the head for a reduced field delivery at vertical orientation. The solenoid needs to have radius larger than 10 cm in order to fit a head inside and length of solenoid should be less than 40 cm for easy handling at surgery prep room environment. A Matlab script was written to optimize the coil dimension for maximizing field strength while reducing power consumption and weight as much as possible. The final coil dimension is concluded in Table 4.3. For the vertical orientation, a minimum of 12 KA/m (15 mT) must be achieved at 5 cm away from the bottom of the coil for actuation. To better predict the field distribution outside the solenoid the following calculation was made.

Analytical expression for field at any location from a single current loop is given by [203]:

$$B_x = \frac{Cxz}{2\alpha^2\beta\rho^2}[(a^2 + r^2)E(k^2) - \alpha^2 K(k^2)] \tag{4.6}$$

$$B_y = \frac{y}{x}B_x \tag{4.7}$$

$$B_z = \frac{C}{2\alpha^2\beta}[(a^2 - r^2)E(k^2) + \alpha^2 K(k^2)] \tag{4.8}$$

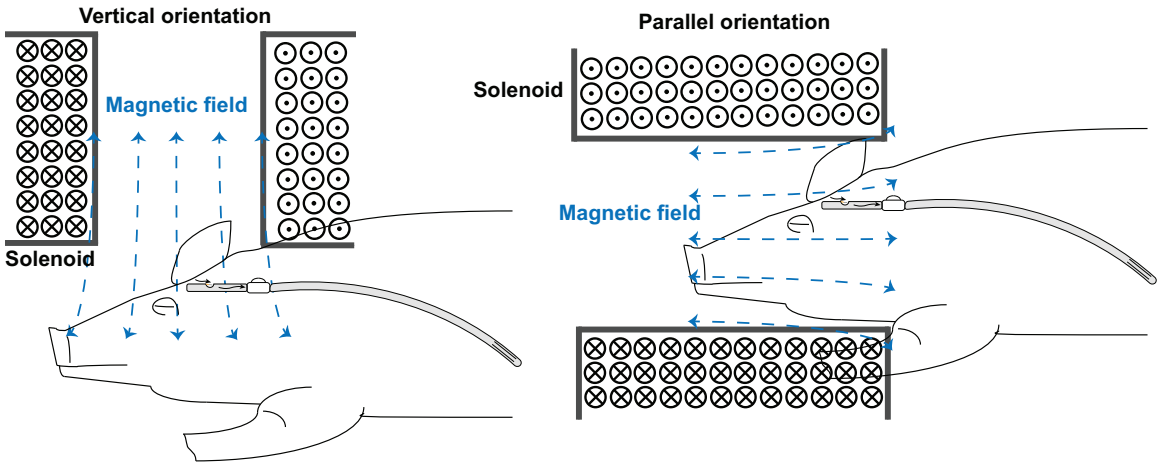

Fig. 4.24. An illustration showing two possible orientation of solenoid coil in relative to animal head.

B_x, B_y and B_z are magnetic flux density components at location (x,y,z) in a cartesian coordinate originated at center of the current loop with supplied current I. The circular loop has radius a. The following substitutions are used: $\rho^2 = x^2+y^2, r^2 = x^2+y^2+z^2, \alpha^2 = a^2+r^2-2a\rho, \beta^2 = a^2+r^2+2a\rho, k^2 = 1-\alpha^2/\beta^2, C = \frac{\mu_0 I}{\pi}$ and $\mu 0$ is magnetic permeability of free space. K, E are complete elliptical integral of the first and second kind respectively. A multilayer air core solenoid coil can be approximated as multiples of single loop stacked together. The field distribution can be solved analytically given size, and spacing the of each turn. A Matlab script was written to calculate the field for better visualization of the distribution.

The point of interest is at the center of solenoid axis because the field is more uniformly distributed compare to edges. For the *in vivo* study, we determined to use the vertical orientation with the coil suspended on top of head because of catheter placement orientation (parallel) and for ease of adjustment. The coil was placed as near to heads as possible as indicated in Fig. 4.27. Magnetic field calculation shows 17 KA/m (21 mT) can be produced at 5 cm away from bottom of coil along center axis (Fig. 4.26, Fig. 4.25), which meets actuation requirement.

Table 4.3.
Coil dimension for *in vivo* experiment

Parameter	Values
Conductor thickness	AWG 12
Inner diameter of solenoid	10 cm
Outer diameter of solenoid	14 cm
Height of solenoid	11 cm
Number of turns	518
Number of layers	14
Current	17 A
Weight	5 Kg

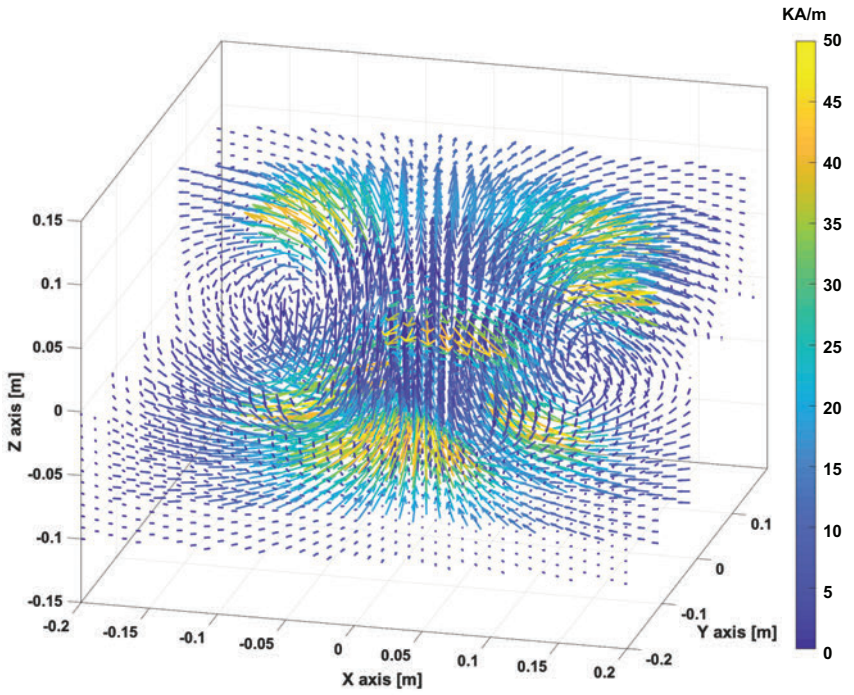

Fig. 4.25. Magnetic field line distribution of the electromagnetic coil at I = 17 A.

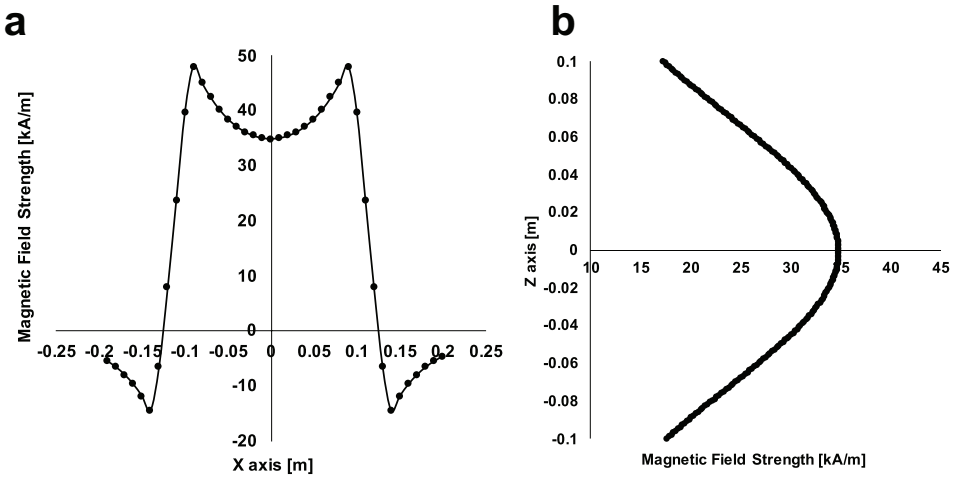

Fig. 4.26. (a) Magnetic field strength distribution along the z-axis. (b) Magnetic field strength distribution along x axis at midway from the top and bottom and midway to a side.

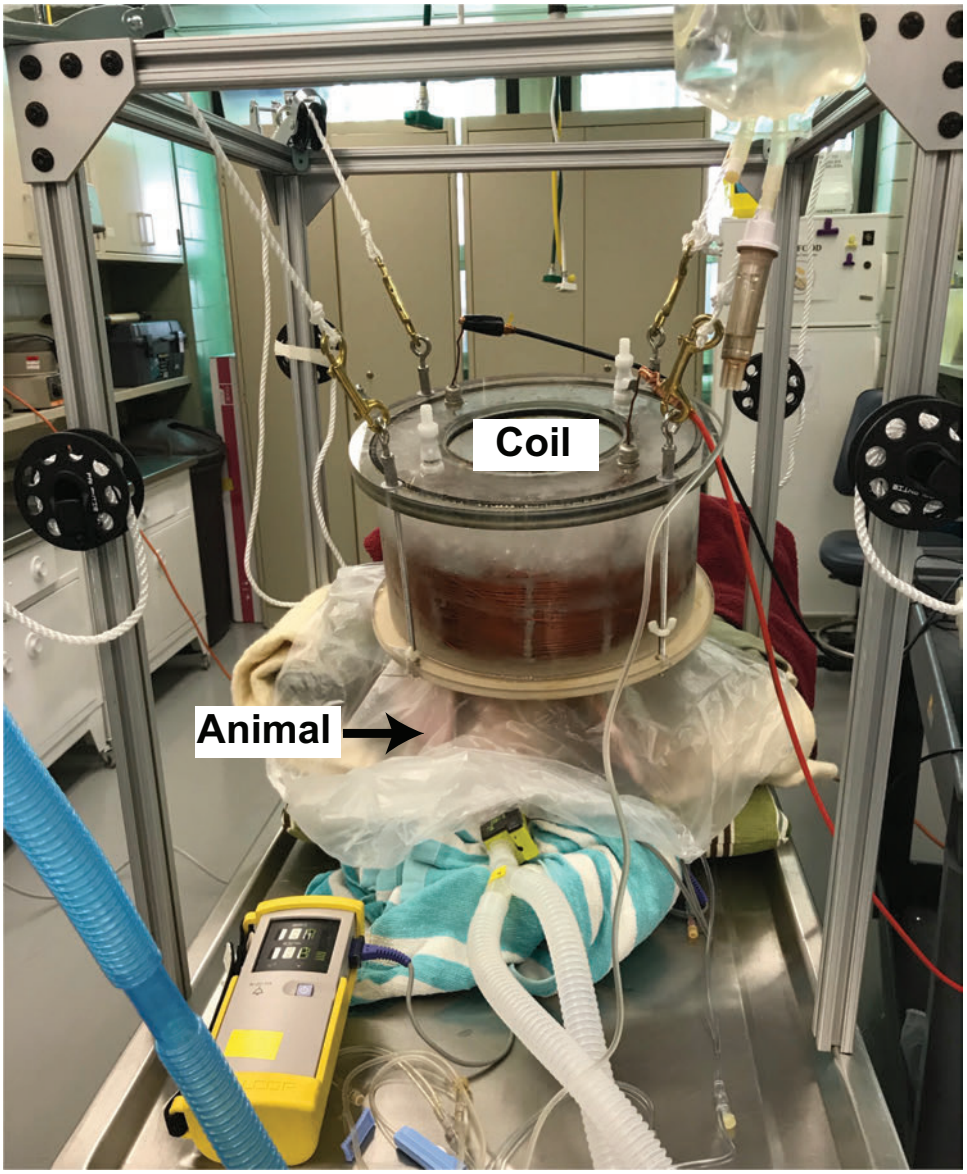

Fig. 4.27. Electromagnet in use for actuation.

5. CONCLUSION AND FUTURE WORK

5.1 Summary

This work presents a clinically translatable engineering approach to prolong hydrocephalus shunt life time in patient. Shunting is the most common hydrocephalus treatment method. A chronically implanted catheter system is typically used to regulate excessive CSF accumulation in ventricle of brain. Biofouling related cellular buildup at inlet holes of ventricular catheter frequently cause CSF drainage failure. Up to 40% of patients experience shunt failure and undergo additional revision surgeries. Hydrocephalus patients and neurosurgeons bear enormous burden because of the failure. To solve the problem, magnetic microactuators were previously proposed to actively remove occlusion at inlet pore wirelessly by mechanical torque and shear stress generation. Using polyimide substrate, a flexible magnetic microactuator was successfully designed and fabricated. A complete device integration at the inlet hole of ventricular catheter was achieved for the first time. An original 'smart shunt' prototype that resists occlusion without surgical intervention was presented. A series of in vitro and in vivo evaluation was conducted using the smart shunt. We made several engineering advancements to incorporate new functionalities and to improve actuation performance. Encouraging results from bench-top and animal studies suggest that the smart shunt with integrated magnetic actuators may be an answer to the longstanding and unresolved shunt failure issue.

Fabrication and integration A novel fabrication sequence was developed using polyimide substrate. The device features a single cantilever with a circular tip mass structure on which ferromagnetic element nickel was electroplated. The actuators remained in good physical appearance without structural damage following a gentle

release process. The flexible nature of polymer substrate allowed a precise fit into the curvature of inner lumen of a catheter. The magnetic actuator was securely attached under catheter inlet pore and subject to 5 ml/s of liquid flushing without positional shift. The polyimide-based thin film actuator exhibits over 45 degrees of angular deflection in static magnetic field for large shear stress production. The range of motion followed theoretical estimation. A primary resonant frequency around 450 Hz and 100 Hz was determined in air and water environment respectively. An improved theoretical estimation for resonant frequency was developed by accounting for distributed mass at structural plate. The precise mathematical model will be beneficial to future parametric design of magnetic actuators.

Mechanical fatigue The ultimate goal is to prolong lifetime of hydrocephalus shunt, therefore it is necessary to ensure that mechanical performance of polymer based magnetic microactuators does not deteriorate after extended use. The device operates dynamically in flexural direction from time varying magnetic field. Thus, mechanical fatigue behavior was evaluated. A group of device was continuously actuated at resonant frequency for 300 million cycles in saline solution kept at 37 °C. 300 millions cycles is equivalent to 30 minutes of actuation every week for 30 years. The resonant frequencies were measured and compared periodically during the experiment to determine cantilever stiffness variations. At end of test no fractures were found. The results indicate minimum resonant frequency shift (<5%) which suggests good mechanical reliability.

Protein removal Serum protein is the first kind of biofilm that attach to implant surface and initiate a series of biofouling cascade [28]. We hypothesize that if serum protein can be periodically removed off an implant surface, the fouling process may be delayed. Therefore, we examined protein clearance capability. A group of devices was coated with bovine serum albumin FITC (BSA-FITC), a type of fluorescent protein. The fluorescent intensity was quantified to estimate amount of protein present on actuator. The devices were subject to magnetic actuation after coating. Fluorescent

intensity was imaged before and after actuation treatment. We demonstrated significant (90%) fluorescent intensity decrease on actuator surface, suggesting excellent serum protein removal efficacy.

Piezoresistive multi-functional sensing Once smart shunt is implanted inside ventricle of brain, it is challenging to examine the actuator behavior optically. In order to monitor the actuator motion electrically, an additional layer of resistive sensing material was integrated to the cantilever to detect the strain cantilever produced from actuation. A thin layer of gold (50 nm) at base of cantilever was deposited followed by additional polyimide encapsulation. Resistance varied as a function of deflection magnitude and direction. Sensitivity of 0.035%/Deg within $-30°$ to $30°$ was observed. Static deflection angles and dynamic responses were successfully measured and converted from resistive readout. Additional functionalities such as magnetic field misalignment sensing, occlusion detection at inlet hole and flow rate sensing were demonstrated.

In vitro dynamic blood clot resistance evaluation Conventional catheter occlusion is unpredictable with wide range of time to failure [5,192]. A in vitro dynamic fluid circulatory setup was developed to reliably produce obstruction from blood clot within a controlled time frame (<4 h). In order to resist occlusion and allow better fluid transportation in the circulatory system, an improved actuator device was developed. The new design features a serpentine cantilever flexure with an increased nickel thickness. As a result, the new actuators produce a significantly more torque (8 times) and deflection angle ($85°$ at 15 mT) comparing to previous design in Chapter 2. We also developed an improved theoretical model to accurately predict magnetic torque for electroplated nickel. Catheters with or without the actuators were compared in the in vitro experiment. Fatal obstruction happened less frequently with magnetic actuation. The system began to clot at a much delayed time (27 vs. 211 min).

In vivo survivability evaluation Finally we presents our first ever attempt to evaluate magnetic actuator on animals. An intraventricular hemorrhage porcine model was used to quickly produce post hemorrhagic hydrocephalus during surgery. The model exhibited an extremely high shunt failure rate (100%,within 7 days) for control group without integrated magnetic actuators. In the contrary, the smart shunt showed much better shunt failure (20%) at end of 42 days using periodic magnetic actuation treatment. The treatment animals also had significantly smaller ventricle volumes.

5.2 Future work

This research features an engineering effort to integrate MEMS actuator into existing medical device for improved clinical efficacy. Despite substantial advancements there is still room for improvements. Discussion from the perspectives of performance and reliability is described here.

Combining passive and active anti-fouling methods This work evaluated the ability to combat biofouling by sole use of mechanical energy. Fouling from a handful of material, such as muscle cells, BSA and blood clot can be curtailed by torque or shear stress generation. It is important to realize that magnetic actuation does not destroy biofilm but rather disperse and redistribute a localized aggregation elsewhere in the drainage path. If biofilm quickly progress to a massive amount in between two successive actuation treatments, obstruction may eventually happen regardless of subsequent magnetic actuation. Therefore, it is necessary to combine actuation with advanced surface materials or topographies as mentioned in Chapter 1 to lower the rate of biofilm attachment for a maximum anti-fouling outcome.

Magnetic materials To further increase amount of torque from magnetic actuator for improved actuator impact, new magnetic materials with larger remanence, sus-

ceptibility and saturation should be explored. Compatibility with fabrication process and biocompatibility should also be considered.

Wireless sensing of cantilever deflection The gold resistive sensor described in this work requires a wired connection, which defeats the purpose of wireless magnetic operation. For future development towards clinical practices, a wireless sensing capability is necessary. A potential challenge is transmitting signal to deep brain space without implanted battery and complex circuitry. A potential solution is placing wireless transceiver at distal catheter on the side near neck. In this way transmission distance from outer sensing apparatus is greatly reduced.

Optimization of actuation There are two aspects to optimize. First, dynamic motion of actuator in liquid needs to be further studied.The static behavior and resonant frequency in air are examined in this work, however the understanding of dynamic motion is still at a crude state, especially for the case of large deflection. The magnetic actuator is a system that couples magnetic problem, solid mechanic problem and hydrodynamic problem. The magnetic problem determines how magnetic material responds to excitation waveform. The solid mechanic problem describes the energy stores and releases from the beam. The hydrodynamic problem provides how much friction the system experiences, which in turn requires the description of motion.

The second aspect is precise delivery of shear stress on catheter sidewalls and actuator surface. Additional computational fluid dynamic simulations need to be studied to optimize actuator geometry and boundary conditions.

Design for manufacturability The current integration process requires manual handing of released substrate which significantly hinders throughput and yields. In the future, a more automated fabrication/integration strategies needs to be explored, for instance, roll-to-roll manufacturing. We might want to consider sandwich the actuator substrate inside silicone sidewall while forming the catheter.

Frequency of actuation treatment During the in vivo study, actuation treatments were conducted at surgery day, one, three and five weeks after implantation. Although this treatment frequency yields satisfactory results, there is little reasoning behind the decision other than logistically convenient and feasible. Therefore, a controlled study should be designed to examine how frequency of treatment impact occlusion outcome. Perhaps, a need based treatment scheme should be developed using feedback from shunt patency sensing.

Reliability This work indicates that the polymer based magnetic actuator can withstand up to 300 millions cycles of cyclic bending without significant shift in beam stiffness. However, the reliability of the magnetic actuators should continue be examined. For instance, the device may subject to sudden mechanical shock (acceleration) while patient is participating intense physical activity or experiencing unexpected head trauma. MEMS device have been previously shown susceptible to fracture due to large magnitude shocks [204].

The geometry of cantilever should be designed not only from the aspect of performance but also from susceptibility to boundary condition change. It is important to realize that the magnetic actuator is intended to function for extended period in human body, a complex and ever changing environment. For example, the newly proposed serpentine beam may be prone to biofilm attachment because of its mesh like spacing. In future iterations, the gap size between adjacent structures needs to be studied.

A. MATLAB SCRIPTS

A.1 Calculation for natural resonant frequencies of magnetic actuators

```
clear
%% Material properties
p_nickel = 7800;% Density of magnet (nickel) (kg/m^3)
p_poly = 1420; % Density of cantilever (polyimide) (kg/m^3)
p_pary = 1289;
p_Cr = 7190;
p_Au = 19300;
E = 2.45e9; % Elastic modulus of polyimide (GPa)
E_pary = 2.3e9;
t_poly = 12e-6;
t_Cr = 20e-9;
t_Au = 50e-9;
t_nickel = 10.265e-6;
t_pary = 0e-6;
l_beam = 400e-6;
w_beam = 49e-6;
R_nickel = 400e-6;
R_poly = 450e-6;
device = 2;

%composite beam add-in
E1 = E;
E2 = E_pary;
```

```
24 t1 = t_poly;
25 t2 = t_pary;
26 L = l_beam;
27 W = w_beam;
28 h0 = t1+t2;
29 h1 = t2;
30 h2 = 0;
31 C11_1 = E1;
32 C11_2 = E2;
33 A11 = C11_1*(h1-h0)+C11_2*(h2-h1);
34 B11 = 0.5*(C11_1*(h1^2-h0^2)+C11_2*(h2^2-h1^2));
35 D11 = 1/3*(C11_1*(h1^3-h0^3)+C11_2*(h2^3-h1^3));
36 EI = abs((B11^2-A11*D11)/A11*W)
37
38 %Dec8 added offset distance 20um
39 %dis_center = [0 100 100 150 200 250]*1e-6+20e-6;
40 dis_center = [0 100 100 150 200 250]*1e-6; % distance from
      center of circle to rotation axis
41 dis_center = dis_center(device);
42 rect_area_poly = [448*155 343*155 343*150 294*150 244*145
      194*145]*1e-12;
43 b_poly = [488 343 343 294 244 194]*1e-6; % long length of
      the polymer rectangle area
44 M_rec_poly = rect_area_poly(device)*(t_poly*p_poly+t_pary*
      p_pary); %mass of rectangle
45 J3_poly = 1/3*M_rec_poly*(b_poly(device))^2 + 1/12*M_rec_poly
      *t_poly^2;
46 %J3_poly is the moment of inertia of rectangular polymer
      region about axis at the end
```

```
47 %of the cantilever, calculated by cuboid reotate about one of
       its edge.
48 rect_area_nickel = [410 300 307 257 208 156]*200*1e-12;
49 d_nickel = [185 130 133.5 109 84 58.5]*1e-6; %distance from
       center of rectangle to rotation axis
50 b_nickel = [410 300 307 257 208 156]*1e-6; %long length of
       rectangle (perpendicular to direction
51 M_rec_nickel = rect_area_nickel(device)*(t_nickel*p_nickel+
       t_Cr*p_Cr+p_Au*t_Au);
52 J3_nickel = 1/12*M_rec_nickel*(b_nickel(device)+t_nickel)^2+
       M_rec_nickel*(d_nickel(device))^2;
53 %J_3_nickel is the moment of inertia of rectangular region of
       metal about axis at the end of
54 %cantilever, caluclated by center axis plus off-set distance
       according to
55 %parallel axis  theorem.
56 J3 = J3_poly+J3_nickel
57 Area_flap = pi*(R_poly)^2-rect_area_poly(device);
58 Area_magnet = [418541 440341 438911 448911 458711 468911]*1e
       -12;
59 A_cross = w_beam*t_poly;
60 m_beam = p_poly*l_beam*A_cross;
61 m_mag = (p_nickel*t_nickel+p_Au*t_Au+p_Cr*t_Cr)*Area_magnet(
       device);
62 m_flap = (p_poly*t_poly+p_pary*t_pary)*Area_flap;
63 M_tip = m_mag+m_flap
64 R = M_tip/m_beam;
65 I = t_poly.^3*w_beam/12;
```

```
66 X = fzero(@(x) 1+1./(cos(x).*cosh(x))-R.*x.*(tan(x)-tanh(x))
       ,0.2);
67 w = X.^2*sqrt(E*I/(p_poly.*A_cross*l_beam^4));
68 f_tipmass = w/2/pi;
69
70 %non-zero moment tip mass
71 m_poly_circle = p_poly*t_poly*pi*(R_poly)^2;
72 m_nickel_circle = (p_nickel*t_nickel+p_Cr*t_Cr+p_Au*t_Au)*pi
       *(R_nickel)^2;
73 J1 = 0.25*m_poly_circle*(R_poly)^2+m_poly_circle*(dis_center)
       ^2+1/12*m_poly_circle*t_poly^2;
74 %J1 is the moment of inertia of circular region of polymer
       about axis at
75 %the end of cantilever, calculated by parallel axis theorem
76 J2 = 0.25*m_nickel_circle*(R_nickel)^2+m_nickel_circle*(
       dis_center)^2+1/12*m_nickel_circle*t_nickel^2;
77 %J2 is the moment of inertia of circular region of metal
       about axis at
78 %the end of cantilever, calculated by parallel axis theorem
79 J = -(J1+J2-J3)
80 p = p_poly;
81 A = A_cross;
82 l = l_beam;
83 M = M_tip
84
85 %Orignial Using E*I Nov 29
86 %fun2 = @(X) -(2*E^2*I^2*X^5*(A^2*l^4*p^2 - J*M*X^4 + A^2*l
       ^4*p^2*cos(X)*cosh(X) + J*M*X^4*cos(X)*cosh(X) + A*J*X^3*l
       *p*cos(X)*sinh(X) + A*J*X^3*l*p*cosh(X)*sin(X) + A*M*X*l
```

```
    ^3*p*cos(X)*sinh(X) - A*M*X*l^3*p*cosh(X)*sin(X)))/(A^2*l
    ^9*p^2);
87 %New Using EI flexural rigitidy from composite beam Nov 29
88 fun2 = @(X) -(2*EI^2*X^5*(A^2*l^4*p^2 - J*M*X^4 + A^2*l^4*p
    ^2*cos(X)*cosh(X) + J*M*X^4*cos(X)*cosh(X) + A*J*X^3*l*p*
    cos(X)*sinh(X) + A*J*X^3*l*p*cosh(X)*sin(X) + A*M*X*l^3*p*
    cos(X)*sinh(X) - A*M*X*l^3*p*cosh(X)*sin(X)))/(A^2*l^9*p
    ^2);
89 X = fzero(fun2,0.3);
90 %Orignal using E*I Nov 29
91 %w = X.^2*sqrt(E*I/(p_poly.*A_cross*l_beam^4));
92 %New using EI
93 w = X.^2*sqrt(EI/(p_poly.*A_cross*l_beam^4));
94 f_inertia = w/2/pi
```

A.2 Magnetic torque and static response

```
1
2  %Oct 29 2018
3  %Qi Yang
4
5  clear
6  close all
7  %load('Per_mag_off_net.mat')
8  mu0 = 4*pi*1e-7;
9  E_m = 2.45e9; % Elastic modulus of polyimide (GPa)
10 %L = 594.8* 1e-6; % Beam length
11 %L = (2000+pi*80*4) * 1e-6;
12 L = 350*1e-6;
13 w = 44 * 1e-6; % Beam width
14 %w = 67*1e-6;
15 %t = 11.2 * 1e-6; % Beam thickness
16 t = 12*1e-6;
17 I = w*t^3/12;
18 p = 7800; %density of Ni Kg/m
19 %Special case for oblate spheroid
20 % assume a<b=c
21 %long axis is b c
22 for thickness = 100:20:100
23 a = thickness/2;
24 b = 790/2;
25 %%b = 800/2;
26 c = 790/2;
27 %c = 905/2;
```

```
%c = 800/2;
C3 = 1;
m = c/a;
Nc = C3/2/(m^2-1)*(m^2/sqrt(m^2-1)*asin(sqrt(m^2-1)/m)-1)
Na = C3 -2*Nc
%
%Torque caluclation as a function of geometry, applied H,
    angle between
%symmetric axis and applied H
%For M< Ms, Ms is saturation magnetization
%Ms = 600KA/m or 0.753T for electroplated nickel
%v = 505000*1e-12*thickness*1e-6; %volume of soft magnet
%H = 40000;  %Applied Magnetic field A/m
mass = p*v
T_offset = 0;
%%% take into account magnetic susceptibility x
%x = 15;  %
x = 11.3;
%Na = (1+Nc*x)/x;
%Nc = (1+Na*x)/x;
%Nc = 0.1;
%
k_theta = E_m*I/(L)
h_max =4e4;
n = 1;
M_sat = 0.74;
M_resi = 0.037/mu0;
%ini = 0.165806; %initial angle at static in Rad
ini = 0*pi/180;
```

```
56 %ini2 = -5.6*pi/180;%diagonal axis differential = -atan(
       diagonal/thickness)
57 ini2 = 0;
58 for H = 0:h_max/1000:h_max
59
60     phi_rad (n) = fzero(@(theta)(mu0*v*((x.*H.^2*cos(theta-
           ini2).*sin(theta-ini2)+M_resi.*H.*cos(theta-ini2)*(1+
           Nc*x))/(1+Nc*x)-x.*H.^2.*sin(theta-ini2).*cos(theta-
           ini2)/(1+Na*x))-T_offset)/k_theta-theta+ini,1);
61
62     %constant M approximation
63     phi_rad2 (n) = fzero(@(theta) v.*M_sat*H*sin(pi/2-theta)/
           k_theta-theta,1);
64     phi_deg (n) = phi_rad(n)*180/pi;
65     phi_deg2 (n) = phi_rad2(n)*180/pi;
66     data(n,:) = [H,phi_deg(n)];
67     data2(n,:) = [H,phi_deg2(n)];
68     n = n+1;
69 end
70 %%%Compare with fix M direction model
71 X = data(:,1)/1000*1000*1000*mu0;
72 Y = data(:,2);
73 plot(X,Y,'o');
74 xlabel('magnetic flux density [mT]')
75 ylabel('deflection angle [DEG]')
76 hold on
77 plot(X,data2(:,2));
78
79 H = 45000 %A/m
```

```
80  theta = pi/2/100;
81  T_mag = mu0*v*abs(x*H.^2*cos(theta).*sin(theta)./(1+Nc*x)-x*H
        .^2.*sin(theta).*cos(theta)/(1+Na*x));
82  theta = pi/2/100;
83  alpha = 0:pi/2/100:pi/2;
84  T_mech = alpha*k_theta;
85
86  figure(2)
87  theta = 0:pi/2/100:pi/2;
88  %for H = (5:2:15)/1000/(4*pi*1e-7)
89  for H = 15/1000/(4*pi*1e-7)
90      %T_mag = mu0*v*abs(x*H.^2*cos(theta).*sin(theta)./(1+Nc*x
            )-x*H.^2.*sin(theta).*cos(theta)/(1+Na*x));
91      T_mag_plot = (mu0*v*abs((x*H.^2.*cos(theta).*sin(theta)+
            M_resi.*H.*cos(theta)*(1+Nc*x))/(1+Nc*x)-x.*H.^2.*sin(
            theta).*cos(theta)/(1+Na*x)));
92      T_mag_old = v.*M_sat*H*sin(pi/2-theta);
93      %take account residual magnetization
94      hold on
95      plot(alpha*180/pi,T_mag_plot)
96      %hold on
97      %plot(alpha*180/pi,T_mag_old)
98      xlabel('Defelction angle [DEG]')
99      ylabel('Magnetic Torque [NM]')
100     %hold on
101     %plot(alpha*180/pi,T_mag_old)
102 end
103 end
```

A.3 Magnetic field visulization

```
%Qi Yang, Jun 20 2017
%analytical solution of magnetic flux generated from
    multiturn multilayer
%solenoid in an air box of any dimension of your choice

clear
close all

r0 = 0.1; %radius of coil . was 0.1
r_out = 0.14; %outer radius of solenoid was 0.14
I = 17;  %current [A] %was 17A
mu0=4*pi*1e-7; %magnetic permeability in vaccuum/air
box_side = 0.2;    %was 0.2
box_top =0.2;      %was 0.2
coil_spacing = 0.003;  % was 0.003m for AWG12
coil_top = 0.055;     %was 0.055
coil_bottom = -coil_top;
mesh_xy_spacing = 0.01;  % was 0.01
mesh_z_spacing = 0.001;    %was 0.001

%%box mesh initialization
[X,Y,Z] = meshgrid(-box_side:mesh_xy_spacing:box_side,-
    box_side:mesh_xy_spacing:box_side,-box_top:mesh_z_spacing:
    box_top);
%Z0 = Z;
Bx = 0*X;
By = 0*Y;
```

```
25 Bz = 0*Z;
26
27 turns_per_layer = length((-abs(-coil_bottom)):coil_spacing:
       coil_top);
28 layer = length(r0:coil_spacing:r_out);
29 turns = turns_per_layer*layer;
30
31 [a1, a2, a3] = size(X);
32 for i = 1:1:a1*a2*a3
33     x = X(i);
34     y = Y(i);
35     z = Z(i);
36     p2 = x.^2+y.^2;
37     gamma = x.^2-y.^2;
38     C = mu0*I/pi;
39     l_cond =0;
40     for r = r0:coil_spacing:r_out
41         for m = (-abs(-coil_bottom)):coil_spacing:coil_top
42
43             r2 = x.^2+y.^2+(z-m).^2;
44             alpha2 = r.^2+r2-2*r.*p2.^0.5;
45             beta2 = r.^2+r2+2*r.*p2.^0.5;
46             k2 = 1-alpha2./beta2;
47             [K,E] = ellipke(k2);
48             %Bx(i) = C.*x.*z/2./alpha2./(beta2.^0.5)./p2.*((
                   r0.^2+r2).*E-alpha2.*K)+Bx(i);
49             Bx(i) = C.*x.*(z-m)/2./alpha2./(beta2.^0.5)./p2
                   .*((r.^2+r2).*E-alpha2.*K)+Bx(i);
50             %By(i) = y./x.*Bx(i)+By(i);
```

```
51                  By(i) = C.*y.*(z-m)/2./alpha2./(beta2.^0.5)./p2
                        .*((r.^2+r2).*E-alpha2.*K)+By(i);
52                  %Bz(i) = C./2./alpha2./(beta2.^0.5).*((r0.^2-r2)
                        .*E+alpha2.*K)+Bz(i);
53                  Bz(i) = C./2./alpha2./(beta2.^0.5).*((r.^2-r2).*E
                       +alpha2.*K)+Bz(i);
54              end
55          end
56      end
57      for r = r0:coil_spacing:r_out
58          l_cond = 2*pi*r*turns_per_layer+l_cond
59      end
60      cross_area = 3.31e-6; %AWG12 wire
61      volume = l_cond*cross_area;
62      density = 8960; %copper Kg/m^3
63      mass= density*volume;
64      resistivity = 1.68e-8; %copper ohm-m
65      resistance = resistivity*l_cond/cross_area
66
67      Y0 = ceil(length(-box_side:mesh_xy_spacing:box_side)/2);
68      for n = 1:1:length(Z(Y0,Y0,:))
69          z_comp(n) = Bz(Y0,Y0,n);
70      end
71
72      Z0 = ceil(length(-box_top:mesh_z_spacing:box_top)/2);
73      for m = 1:1:length(X(:,Y0,Z0))
74          z_comp2(m) = Bz(m,Y0,Z0);
75          net(m) = sqrt((Bz(m,Y0,Z0)).^2+(Bx(m,Y0,Z0)).^2+(By(m,Y0,
                Z0)).^2)
```

```
76 end
77
78 %Z = Z-0.5;
79 %quiver3d(X,Y,Z,Bx,By,Bz);
80 %Visualization
81 %quiverC3D(X,Y,Z,Bx,By,Bz,5000);
82 fprintf('\nthis coil has %d turns\n\n',turns)
83 figure(2)% plot Mganetic flux alon center axis (z)
84 plot(-box_top:mesh_z_spacing:box_top,z_comp,'or')
85 z_output = -box_top:mesh_z_spacing:box_top;
86 xlabel('z axis [m]')
87 ylabel('Magnetic flux [T]')
88 %Z component field strenth across Z axis
89 figure(3)
90 plot(-box_side:mesh_xy_spacing:box_side,z_comp2,'ok')
91 x_output = -box_side:mesh_xy_spacing:box_side;
92 xlabel('x axis [m]')
93 ylabel('Magnetic flux [T]')
94 %Z component field strength across x axis
```

REFERENCES

[1] "Hydrocephalus fact sheet." [Online]. Available: https://www.ninds.nih.gov/Disorders/Patient-Caregiver-Education/Fact-Sheets/Hydrocephalus-Fact-Sheet

[2] J. H. Chi, H. J. Fullerton, and N. Gupta, "Time trends and demographics of deaths from congenital hydrocephalus in children in the united states: National center for health statistics data, 1979 to 1998," *Journal of Neurosurgery: Pediatrics*, vol. 103, no. 2, pp. 113–118, 2005.

[3] T. D. Simon, M. Hall, J. Riva-Cambrin, J. E. Albert, H. E. Jeffries, B. LaFleur, J. M. Dean, and J. R. Kestle, "Infection rates following initial cerebrospinal fluid shunt placement across pediatric hospitals in the united states," *Journal of Neurosurgery: Pediatrics*, vol. 4, no. 2, pp. 156–165, 2009.

[4] T. D. Simon, J. Riva-Cambrin, R. Srivastava, S. L. Bratton, J. M. Dean, and J. R. Kestle, "Hospital care for children with hydrocephalus in the united states: utilization, charges, comorbidities, and deaths," *Journal of Neurosurgery: Pediatrics*, vol. 1, no. 2, pp. 131–137, 2008.

[5] K. T. Kahle, A. V. Kulkarni, D. D. Limbrick Jr, and B. C. Warf, "Hydrocephalus in children," *The lancet*, vol. 387, no. 10020, pp. 788–799, 2016.

[6] "Seizing the moment: Can hydrocephalus cause a seizure?" Aug 2013. [Online]. Available: https://www.emsworld.com/article/11102879/seizing-moment-can-hydrocephalus-cause-seizure

[7] J. Brunski, B. Ratner, A. Hoffman, F. Schoen, and J. Lemons, "Biomaterials science," *Academic Press, San Diego, CA*, pp. 37–130, 1996.

[8] Y. Ikada, "Surface modification of polymers for medical applications," *Biomaterials*, vol. 15, no. 10, pp. 725–736, 1994.

[9] W. F. Schoener, C. Reparon, R. Verheggen, and E. Markakis, "Evaluation of shunt failures by compliance analysis and inspection of shunt valves and shunt materials, using microscopic or scanning electron microscopic techniques," in *Hydrocephalus*. Springer, 1991, pp. 452–472.

[10] N. Kossovsky and R. B. Snow, "Clinical-pathological analysis of failed central nervous system fluid shunts," *Journal of biomedical materials research*, vol. 23, no. S13, pp. 73–86, 1989.

[11] R. Jones, W. Stening, and M. Brydon, "Endoscopic third ventriculostomy," *Neurosurgery*, vol. 26, no. 1, pp. 86–92, 1990.

[12] Y. R. Yadav, V. Parihar, S. Pande, H. Namdev, and M. Agarwal, "Endoscopic third ventriculostomy," *Journal of neurosciences in rural practice*, vol. 3, no. 2, p. 163, 2012.

[13] A. V. Kulkarni, J. M. Drake, C. L. Mallucci, S. Sgouros, J. Roth, S. Constantini, C. P. N. S. Group *et al.*, "Endoscopic third ventriculostomy in the treatment of childhood hydrocephalus," *The Journal of pediatrics*, vol. 155, no. 2, pp. 254–259, 2009.

[14] S. R. Browd, B. T. Ragel, O. N. Gottfried, and J. R. Kestle, "Failure of cerebrospinal fluid shunts: part i: obstruction and mechanical failure," *Pediatric neurology*, vol. 34, no. 2, pp. 83–92, 2006.

[15] C. A. Harris and J. P. McAllister, "What we should know about the cellular and tissue response causing catheter obstruction in the treatment of hydrocephalus," *Neurosurgery*, vol. 70, no. 6, pp. 1589–1602, 2011.

[16] M. R. Del Bigio, "Biological reactions to cerebrospinal fluid shunt devices: a review of the cellular pathology," *Neurosurgery*, vol. 42, no. 2, pp. 319–326, 1998.

[17] S. Tuli, J. Drake, J. Lawless, M. Wigg, and M. Lamberti-Pasculli, "Risk factors for repeated cerebrospinal shunt failures in pediatric patients with hydrocephalus," *Journal of neurosurgery*, vol. 92, no. 1, pp. 31–38, 2000.

[18] J. Lin, M. Morris, W. Olivero, F. Boop, and R. A. Sanford, "Computational and experimental study of proximal flow in ventricular catheters," *Journal of neurosurgery*, vol. 99, no. 2, pp. 426–431, 2003.

[19] W. Serlo, E. Fernell, E. Heikkinen, H. Anderson, and L. Von Wendt, "Functions and complications of shunts in different etiologies of childhood hydrocephalus," *Child's Nervous System*, vol. 6, no. 2, pp. 92–94, 1990.

[20] M. R. Del Bigio and S. Fedoroff, "Short-term response of brain tissue to cerebrospinal fluid shunts in vivo and in vitro," *Journal of biomedical materials research*, vol. 26, no. 8, pp. 979–987, 1992.

[21] J. M. Drake and C. Sainte-Rose, *The shunt book*. Blackwell Science, 1995.

[22] O. Sugar and O. T. Bailey, "Subcutaneous reaction to silicone in ventriculoperitoneal shunts: long-term results," *Journal of neurosurgery*, vol. 41, no. 3, pp. 367–371, 1974.

[23] J. Bruni and M. Del Bigio, "Reaction of periventricular tissue in the rat fourth ventricle to chronically placed shunt tubing implants," *Neurosurgery*, vol. 19, no. 3, pp. 337–345, 1986.

[24] L. N. Sekhar, J. Moossy, and A. N. Guthkelch, "Malfunctioning ventriculoperitoneal shunts: Clinical and pathological features," *Journal of neurosurgery*, vol. 56, no. 3, pp. 411–416, 1982.

[25] S. Bigner, P. Elmore, A. Dee, and W. Johnston, "The cytopathology of reactions to ventricular shunts." *Acta cytologica*, vol. 29, no. 3, pp. 391–396, 1985.

[26] Z. Czernicki, R. Strzałkowski, N. Walasek, and B. Gajkowska, "What can be found inside shunt catheters," in *Brain edema XIV*. Springer, 2010, pp. 81–85.

[27] U. W. Thomale, H. Hosch, A. Koch, M. Schulz, G. Stoltenburg, E.-J. Haberl, and C. Sprung, "Perforation holes in ventricular catheters – is less more?" *Child's Nervous System*, vol. 26, no. 6, pp. 781–789, 2010.

[28] Y. KyungáKim *et al.*, "Biomolecular strategies to modulate the macrophage response to implanted materials," *Journal of Materials Chemistry B*, vol. 4, no. 9, pp. 1600–1609, 2016.

[29] J. S. Baru, D. A. Bloom, K. Muraszko, and C. E. Koop, "John holter?s shunt," *Journal of the American College of Surgeons*, vol. 192, no. 1, pp. 79–85, 2001.

[30] R. H. Pudenz, F. E. Russell, A. H. Hurd, and C. H. Shelden, "Ventriculo-auriculostomy. a technique for shunting cerebrospinal fluid into the right auricle: preliminary report," *Journal of neurosurgery*, vol. 14, no. 2, pp. 171–179, 1957.

[31] U. Kehler, J. Regelsberger, J. Gliemroth, and M. Westphal, "Outcome prediction of third ventriculostomy: a proposed hydrocephalus grading system," *min-Minimally Invasive Neurosurgery*, vol. 49, no. 04, pp. 238–243, 2006.

[32] J. V. Pattisapu, E. R. Trumble, K. R. Taylor, P. D. Howard, and T. M. Kovach, "Percutaneous endoscopic recanalization of the catheter: a new technique of proximal shunt revision," *Neurosurgery*, vol. 45, no. 6, pp. 1361–1367, 1999.

[33] H. J. Ginsberg, J. M. Drake, T. M. Peterson, and R. S. C. Cobbold, "Recanalization of obstructed cerebrospinal fluid ventricular catheters using ultrasonic cavitation." *Neurosurgery*, vol. 59, no. 4 Suppl 2, pp. ONS403–12; discussion ONS412, oct 2006.

[34] W. A. Christens-Barry, M. Guarnieri, and B. S. Carson, "Fiberoptic delivery of laser energy to remove occlusions from ventricular shunts: technical report," *Neurosurgery*, vol. 44, no. 2, pp. 345–349, 1999.

[35] D. P. Becker and F. E. Nulsen, "Control of hydrocephalus by valve-regulated venous shunt: avoidance of complications in prolonged shunt maintenance," *Journal of Neurosurgery*, vol. 28, no. 3, pp. 215–226, 1968.

[36] R. D. Illingworth, V. Logue, L. Symon, and K. Uemura, "The ventriculocaval shunt in the treatment of adult hydrocephalus: results and complications in 101 patients," *Journal of neurosurgery*, vol. 35, no. 6, pp. 681–685, 1971.

[37] J. Vries, "Endoscopy as an adjunct to shunting for hydrocephalus." *Surgical neurology*, vol. 13, no. 1, pp. 69–72, 1980.

[38] S. Tuli, B. O'Hayon, J. Drake, M. Clarke, and J. Kestle, "Change in ventricular size and effect of ventricular catheter placement in pediatric patients with shunted hydrocephalus," *Neurosurgery*, vol. 45, no. 6, pp. 1329–1335, 1999.

[39] T.-T. Wong, L.-S. Lee, R.-S. Liu, S.-H. Yeh, T. Chang, D. M. Ho, G. C. Niu, and Y.-J. Wang, "Hydrogel ventriculo-subdural shunt for the treatment of hydrocephalus in children," in *Hydrocephalus*. Springer, 1991, pp. 438–449.

[40] J. Kopeček and J. Yang, "Hydrogels as smart biomaterials," *Polymer international*, vol. 56, no. 9, pp. 1078–1098, 2007.

[41] J.-P. Montheard, M. Chatzopoulos, and D. Chappard, "2-hydroxyethyl methacrylate (hema): chemical properties and applications in biomedical fields," *Journal of Macromolecular Science, Part C: Polymer Reviews*, vol. 32, no. 1, pp. 1–34, 1992.

[42] J. T. Parsons, A. R. Horwitz, and M. A. Schwartz, "Cell adhesion: integrating cytoskeletal dynamics and cellular tension," *Nature reviews Molecular cell biology*, vol. 11, no. 9, p. 633, 2010.

[43] J. P. Winer, P. A. Janmey, M. E. McCormick, and M. Funaki, "Bone marrow-derived human mesenchymal stem cells become quiescent on soft substrates but remain responsive to chemical or mechanical stimuli," *Tissue Engineering Part A*, vol. 15, no. 1, pp. 147–154, 2008.

[44] M. J. Ellis, C. J. Kazina, M. R. Del Bigio, and P. J. McDonald, "Treatment of recurrent ventriculoperitoneal shunt failure associated with persistent cerebrospinal fluid eosinophilia and latex allergy by use of an ?extracted? shunt: Case report," *Journal of Neurosurgery: Pediatrics*, vol. 1, no. 3, pp. 237–239, 2008.

[45] C. P. Millward, S. P. Da Rosa, D. Williams, G. Kokai, A. Byrne, and B. Pettorini, "Foreign body granuloma secondary to ventriculo-peritoneal shunt: a rare scenario with a new insight," *Pediatric neurosurgery*, vol. 49, no. 4, pp. 236–239, 2013.

[46] K. R. Patel, H. Tang, W. E. Grever, K. Y. S. Ng, J. Xiang, R. F. Keep, T. Cao, and J. P. McAllister II, "Evaluation of polymer and self-assembled monolayer-coated silicone surfaces to reduce neural cell growth," *Biomaterials*, vol. 27, no. 8, pp. 1519–1526, 2006.

[47] K. M. DeFife, M. S. Shive, K. M. Hagen, D. L. Clapper, and J. M. Anderson, "Effects of photochemically immobilized polymer coatings on protein adsorption, cell adhesion, and the foreign body reaction to silicone rubber," *Journal of Biomedical Materials Research: An Official Journal of The Society for Biomaterials, The Japanese Society for Biomaterials, and The Australian Society for Biomaterials*, vol. 44, no. 3, pp. 298–307, 1999.

[48] R. Bayston, C. Bhundia, and W. Ashraf, "Hydromer-coated catheters to prevent shunt infection?" *Journal of Neurosurgery: Pediatrics*, vol. 102, no. 2, pp. 207–212, 2005.

[49] F. Cağavi, N. Akalan, H. Celik, D. Gür, and B. Güçiz, "Effect of hydrophilic coating on microorganism colonization in silicone tubing," *Acta neurochirurgica*, vol. 146, no. 6, pp. 603–610, 2004.

[50] J. J. Boelens, S. A. Zaat, J. Meeldijk, and J. Dankert, "Subcutaneous abscess formation around catheters induced by viable and nonviable staphylococcus epidermidis as well as by small amounts of bacterial cell wall components," *Journal of biomedical materials research*, vol. 50, no. 4, pp. 546–556, 2000.

[51] Y. Izci, H. Secer, C. Akay, and E. Gonul, "Initial experience with silver-impregnated polyurethane ventricular catheter for shunting of cerebrospinal fluid in patients with infected hydrocephalus," *Neurological research*, vol. 31, no. 3, pp. 234–237, 2009.

[52] M. Galarza, Á. Giménez, O. Pellicer, J. Valero, and J. M. Amigó, "New designs of ventricular catheters for hydrocephalus by 3-d computational fluid dynamics," *Child's Nervous System*, vol. 31, no. 1, pp. 37–48, 2015.

[53] H. J. Ginsberg, A. Sum, J. M. Drake, and R. S. Cobbold, "Ventriculoperitoneal shunt flow dependency on the number of patent holes in a ventricular catheter," *Pediatric neurosurgery*, vol. 33, no. 1, pp. 7–11, 2000.

[54] B. A. Kaufman and T. Park, "Ventricular anatomy and shunt catheters," *Pediatric neurosurgery*, vol. 31, no. 1, pp. 1–6, 1999.

[55] C. Zhu, T. Yago, J. Lou, V. I. Zarnitsyna, and R. P. McEver, "Mechanisms for flow-enhanced cell adhesion," *Annals of biomedical engineering*, vol. 36, no. 4, pp. 604–621, 2008.

[56] M. Long, S. Lu, and G. Sun, "Kinetics of receptor-ligand interactions in immune responses," *Cell Mol Immunol*, vol. 3, no. 2, pp. 79–86, 2006.

[57] J. E. Duddridge, C. Kent, and J. Laws, "Effect of surface shear stress on the attachment of pseudomonas fluorescens to stainless steel under defined flow conditions," *Biotechnology and bioengineering*, vol. 24, no. 1, pp. 153–164, 1982.

[58] M. S. Shive, S. M. Hasan, and J. M. Anderson, "Shear stress effects on bacterial adhesion, leukocyte adhesion, and leukocyte oxidative capacity on a polyetherurethane," *Journal of Biomedical Materials Research: An Official Journal of The Society for Biomaterials, The Japanese Society for Biomaterials, and The Australian Society for Biomaterials and the Korean Society for Biomaterials*, vol. 46, no. 4, pp. 511–519, 1999.

[59] M. R. Nejadnik, H. C. van der Mei, W. Norde, and H. J. Busscher, "Bacterial adhesion and growth on a polymer brush-coating," *Biomaterials*, vol. 29, no. 30, pp. 4117–4121, 2008.

[60] Á. Giménez, M. Galarza, O. Pellicer, J. Valero, and J. M. Amigó, "Influence of the hole geometry on the flow distribution in ventricular catheters for hydrocephalus," *Biomedical engineering online*, vol. 15, no. 1, p. 71, 2016.

[61] M. G. Tal, A. J. Peixoto, S. T. Crowley, N. Denbow, D. Eliseo, and J. Pollak, "Comparison of side hole versus non side hole high flow hemodialysis catheters," *Hemodialysis International*, vol. 10, no. 1, pp. 63–67, 2006.

[62] N. J. Hallab, K. J. Bundy, K. O'Connor, R. L. Moses, and J. J. Jacobs, "Evaluation of metallic and polymeric biomaterial surface energy and surface roughness characteristics for directed cell adhesion," *Tissue engineering*, vol. 7, no. 1, pp. 55–71, 2001.

[63] N. J. Hallab, K. Bundy, K. O'connor, R. Clark, and R. Moses, "Cell adhesion to biomaterials: correlations between surface charge, surface roughness, adsorbed protein, and cell morphology." *Journal of long-term effects of medical implants*, vol. 5, no. 3, pp. 209–231, 1995.

[64] S. Schilp, A. Rosenhahn, M. E. Pettitt, J. Bowen, M. E. Callow, J. A. Callow, and M. Grunze, "Physicochemical properties of (ethylene glycol)-containing self-assembled monolayers relevant for protein and algal cell resistance," *Langmuir*, vol. 25, no. 17, pp. 10 077–10 082, 2009.

[65] H. Ma, J. Hyun, P. Stiller, and A. Chilkoti, "?non-fouling? oligo (ethylene glycol)-functionalized polymer brushes synthesized by surface-initiated atom transfer radical polymerization," *Advanced Materials*, vol. 16, no. 4, pp. 338–341, 2004.

[66] J. C. Yarbrough, J. P. Rolland, J. M. DeSimone, M. E. Callow, J. A. Finlay, and J. A. Callow, "Contact angle analysis, surface dynamics, and biofouling characteristics of cross-linkable, random perfluoropolyether-based graft terpolymers," *Macromolecules*, vol. 39, no. 7, pp. 2521–2528, 2006.

[67] W. K. Cho, B. Kong, and I. S. Choi, "Highly efficient non-biofouling coating of zwitterionic polymers: Poly ((3-(methacryloylamino) propyl)-dimethyl (3-sulfopropyl) ammonium hydroxide)," *Langmuir*, vol. 23, no. 10, pp. 5678–5682, 2007.

[68] Y.-F. Yang, Y. Li, Q.-L. Li, L.-S. Wan, and Z.-K. Xu, "Surface hydrophilization of microporous polypropylene membrane by grafting zwitterionic polymer for anti-biofouling," *Journal of Membrane Science*, vol. 362, no. 1-2, pp. 255–264, 2010.

[69] S. Satzl, C. Henn, P. Christoph, P. Kurz, U. Stampfl, S. Stampfl, F. Thomas, B. Radeleff, I. Berger, M. Grunze *et al.*, "The efficacy of nanoscale poly [bis (trifluoroethoxy) phosphazene](ptfep) coatings in reducing thrombogenicity and late in-stent stenosis in a porcine coronary artery model," *Investigative radiology*, vol. 42, no. 5, pp. 303–311, 2007.

[70] F. C. Fang, "Perspectives series: host/pathogen interactions. mechanisms of nitric oxide-related antimicrobial activity." *The Journal of clinical investigation*, vol. 99, no. 12, pp. 2818–2825, 1997.

[71] J.-d. Luo and A. F. Chen, "Nitric oxide: a newly discovered function on wound healing," *Acta Pharmacologica Sinica*, vol. 26, no. 3, p. 259, 2005.

[72] J. Wallis, "Nitric oxide and blood: a review," *Transfusion medicine*, vol. 15, no. 1, pp. 1–11, 2005.

[73] D. L. H. Williams, "A chemist's view of the nitric oxide story," *Organic & biomolecular chemistry*, vol. 1, no. 3, pp. 441–449, 2003.

[74] S. H. Baek, J. A. Hrabie, L. K. Keefer, D. Hou, N. Fineberg, R. Rhoades, and K. L. March, "Augmentation of intrapericardial nitric oxide level by a prolonged-release nitric oxide donor reduces luminal narrowing after porcine coronary angioplasty," *Circulation*, vol. 105, no. 23, pp. 2779–2784, 2002.

[75] A. Chaux, X. M. Ruan, M. C. Fishbein, Y. Ouyang, S. Kaul, J. A. Pass, and J. M. Matloff, "Perivascular delivery of a nitric oxide donor inhibits neointimal hyperplasia in vein grafts implanted in the arterial circulation," *The Journal of thoracic and cardiovascular surgery*, vol. 115, no. 3, pp. 604–614, 1998.

[76] R. Gifford, M. M. Batchelor, Y. Lee, G. Gokulrangan, M. E. Meyerhoff, and G. S. Wilson, "Mediation of in vivo glucose sensor inflammatory response via nitric oxide release," *Journal of Biomedical Materials Research Part A: An Official Journal of The Society for Biomaterials, The Japanese Society for Biomaterials, and The Australian Society for Biomaterials and the Korean Society for Biomaterials*, vol. 75, no. 4, pp. 755–766, 2005.

[77] B. Mellion, L. Ignarro, E. Ohlstein, E. Pontecorvo, A. Hyman, and P. Kadowitz, "Evidence for the inhibitory role of guanosine 3?, 5?-monophosphate," *Blood*, vol. 57, no. 5, 1981.

[78] B. J. Nablo, A. R. Rothrock, and M. H. Schoenfisch, "Nitric oxide-releasing sol–gels as antibacterial coatings for orthopedic implants," *Biomaterials*, vol. 26, no. 8, pp. 917–924, 2005.

[79] M. Radomski, R. Palmer, and S. Moncada, "Comparative pharmacology of endothelium-derived relaxing factor, nitric oxide and prostacyclin in platelets," *British journal of pharmacology*, vol. 92, no. 1, pp. 181–187, 1987.

[80] E. M. Hetrick, J. H. Shin, H. S. Paul, and M. H. Schoenfisch, "Anti-biofilm efficacy of nitric oxide-releasing silica nanoparticles," *Biomaterials*, vol. 30, no. 14, pp. 2782–2789, 2009.

[81] R. J. Barnes, J. H. Low, R. R. Bandi, M. Tay, F. Chua, T. Aung, A. G. Fane, S. Kjelleberg, and S. A. Rice, "Nitric oxide treatment for the control of reverse osmosis membrane biofouling," *Appl. Environ. Microbiol.*, vol. 81, no. 7, pp. 2515–2524, 2015.

[82] G. Regev-Shoshani, M. Ko, C. Miller, and Y. Av-Gay, "Slow release of nitric oxide from charged catheters and its effect on biofilm formation by escherichia coli," *Antimicrobial agents and chemotherapy*, vol. 54, no. 1, pp. 273–279, 2010.

[83] E. J. Brisbois, H. Handa, T. C. Major, R. H. Bartlett, and M. E. Meyerhoff, "Long-term nitric oxide release and elevated temperature stability with s-nitroso-n-acetylpenicillamine (snap)-doped elast-eon e2as polymer," *Biomaterials*, vol. 34, no. 28, pp. 6957–6966, 2013.

[84] K. K. Chung, J. F. Schumacher, E. M. Sampson, R. A. Burne, P. J. Antonelli, and A. B. Brennan, "Impact of engineered surface microtopography on biofilm formation of staphylococcus aureus," *Biointerphases*, vol. 2, no. 2, pp. 89–94, 2007.

[85] E. P. Ivanova, J. Hasan, H. K. Webb, V. K. Truong, G. S. Watson, J. A. Watson, V. A. Baulin, S. Pogodin, J. Y. Wang, M. J. Tobin *et al.*, "Natural bactericidal surfaces: mechanical rupture of pseudomonas aeruginosa cells by cicada wings," *Small*, vol. 8, no. 16, pp. 2489–2494, 2012.

[86] S. Pogodin, J. Hasan, V. A. Baulin, H. K. Webb, V. K. Truong, T. H. P. Nguyen, V. Boshkovikj, C. J. Fluke, G. S. Watson, J. A. Watson *et al.*, "Biophysical model of bacterial cell interactions with nanopatterned cicada wing surfaces," *Biophysical journal*, vol. 104, no. 4, pp. 835–840, 2013.

[87] M. N. Dickson, E. I. Liang, L. A. Rodriguez, N. Vollereaux, and A. F. Yee, "Nanopatterned polymer surfaces with bactericidal properties," *Biointerphases*, vol. 10, no. 2, p. 021010, 2015.

[88] M. Nedelmann, C. Brandt, F. Schneider, B. M. Eicke, O. Kempski, F. Krummenauer, and M. Dieterich, "Ultrasound-induced blood clot dissolution without a thrombolytic drug is more effective with lower frequencies," *Cerebrovascular Diseases*, vol. 20, no. 1, pp. 18–22, 2005.

[89] U. Rosenschein, V. Furman, E. Kerner, I. Fabian, J. Bernheim, and Y. Eshel, "Ultrasound imaging–guided noninvasive ultrasound thrombolysis: Preclinical results," *Circulation*, vol. 102, no. 2, pp. 238–245, 2000.

[90] N. Kucher, P. Boekstegers, O. J. Müller, C. Kupatt, J. Beyer-Westendorf, T. Heitzer, U. Tebbe, J. Horstkotte, R. Müller, E. Blessing *et al.*, "Randomized, controlled trial of ultrasound-assisted catheter-directed thrombolysis for acute intermediate-risk pulmonary embolism," *Circulation*, vol. 129, no. 4, pp. 479–486, 2014.

[91] J. Kim, B. D. Lindsey, W.-Y. Chang, X. Dai, J. M. Stavas, P. A. Dayton, and X. Jiang, "Intravascular forward-looking ultrasound transducers for microbubble-mediated sonothrombolysis," *Scientific reports*, vol. 7, no. 1, p. 3454, 2017.

[92] V. Pepakayala, J. Stein, and Y. Gianchandani, "Resonant magnetoelastic microstructures for wireless actuation of liquid flow on 3d surfaces and use in glaucoma drainage implants," *Microsystems & Nanoengineering*, vol. 1, p. 15032, 2015.

[93] C.-H. Hong, A. Arosemena, D. Zurakowski, and R. S. Ayyala, "Glaucoma drainage devices: a systematic literature review and current controversies," *Survey of ophthalmology*, vol. 50, no. 1, pp. 48–60, 2005.

[94] G. Hwang, A. J. Paula, E. E. Hunter, Y. Liu, A. Babeer, B. Karabucak, K. Stebe, V. Kumar, E. Steager, and H. Koo, "Catalytic antimicrobial robots for biofilm eradication," *Science Robotics*, vol. 4, no. 29, p. eaaw2388, 2019.

[95] W. Wang, J. V. Timonen, A. Carlson, D.-M. Drotlef, C. T. Zhang, S. Kolle, A. Grinthal, T.-S. Wong, B. Hatton, S. H. Kang *et al.*, "Multifunctional ferrofluid-infused surfaces with reconfigurable multiscale topography," *Nature*, vol. 559, no. 7712, p. 77, 2018.

[96] P.-Y. J. Yeh, J. N. Kizhakkedathu, J. D. Madden, and M. Chiao, "Electric field and vibration-assisted nanomolecule desorption and anti-biofouling for biosensor applications," *Colloids and Surfaces B: Biointerfaces*, vol. 59, no. 1, pp. 67–73, 2007.

[97] H. Lee, *Development and Functional Evaluation of Unobstructing Magnetic Microactuators for Self-Clearing Implantable Catheters*. University of California, Los Angeles, 2011.

[98] S. A. Lee, H. Lee, J. R. Pinney, E. Khialeeva, M. Bergsneider, and J. W. Judy, "Development of microfabricated magnetic actuators for removing cellular occlusion," *Journal of Micromechanics and Microengineering*, vol. 21, no. 5, p. 054006, 2011.

[99] H. Lee, K. Kolahi, M. Bergsneider, and J. W. Judy, "Mechanical evaluation of unobstructing magnetic microactuators for implantable ventricular catheters," *Journal of Microelectromechanical Systems*, vol. 23, no. 4, pp. 795–802, 2014.

[100] H. Lee, Q. Xu, F. G. Shellock, M. Bergsneider, and J. W. Judy, "Evaluation of magnetic resonance imaging issues for implantable microfabricated magnetic actuators," *Biomedical microdevices*, vol. 16, no. 1, pp. 153–161, 2014.

[101] J. W. Judy, R. S. Muller, and H. H. Zappe, "Magnetic microactuation of polysilicon flexure structures," *Journal of microelectromechanical systems*, vol. 4, no. 4, pp. 162–169, 1995.

[102] J. W. Judy and R. S. Muller, "Magnetically actuated, addressable microstructures," *Journal of Microelectromechanical systems*, vol. 6, no. 3, pp. 249–256, 1997.

[103] ——, "Magnetic microactuation of torsional polysilicon structures," *Sensors and Actuators A: Physical*, vol. 53, no. 1-3, pp. 392–397, 1996.

[104] S. A. Lee, J. R. Pinney, M. Bergsneider, and J. W. Judy, "Magnetic microactuators for mems-enabled ventricular catheters for hydrocephalus," in *2007 3rd International IEEE/EMBS Conference on Neural Engineering*. IEEE, 2007, pp. 65–68.

[105] Q. Yang, H. Park, T. N. Nguyen, J. F. Rhoads, A. Lee, R. T. Bentley, J. W. Judy, and H. Lee, "Anti-biofouling implantable catheter using thin-film magnetic microactuators," *Sensors and Actuators B: Chemical*, vol. 273, pp. 1694–1704, 2018.

[106] Q. Yang, A. Lee, R. T. Bentley, and H. Lee, "Piezoresistor-embedded multifunctional magnetic microactuators for implantable self-clearing catheter," *IEEE Sensors Journal*, vol. 19, no. 4, pp. 1373–1378, 2018.

[107] M. Simões, L. C. Simões, and M. J. Vieira, "A review of current and emergent biofilm control strategies," *LWT - Food Science and Technology*, vol. 43, no. 4, pp. 573 – 583, 2010.

[108] L. Yu, B. J. Kim, and E. Meng, "Chronically implanted pressure sensors: challenges and state of the field," *Sensors*, vol. 14, no. 11, pp. 20 620–20 644, 2014.

[109] W. K. Ward, "A review of the foreign-body response to subcutaneously-implanted devices: the role of macrophages and cytokines in biofouling and fibrosis." *Journal of diabetes science and technology (Online)*, vol. 2, no. 5, pp. 768–777, 2008.

[110] J. H. Chi, H. J. Fullerton, and N. Gupta, "Time trends and demographics of deaths from congenital hydrocephalus in children in the United States: National Center for Health Statistics data, 1979 to 1998." *Journal of Neurosurgery*, vol. 103, no. Pediatrics 2, pp. 113–118, 2005.

[111] T. D. Simons, M. Hall, J. Riva-Cambrin, J. E. Albert, H. E. Jeffries, B. Lafleur, J. M. Dean, J. R. W. Kestle, and T. H. C. R. Network, "Infection rates following initial cerebrospinal fluid shunt placement across pediatric hospitals in the United States," *Journal of Neurosurgery Pediatric*, vol. 4, no. 2, pp. 156–165, 2010.

[112] B. R. Lutz, P. Venkataraman, and S. R. Browd, "New and improved ways to treat hydrocephalus: pursuit of a smart shunt," *Surgical neurology international*, vol. 4, no. Suppl 1, p. S38, 2013.

[113] S. Krishnan, C. J. Weinman, and C. K. Ober, "Advances in polymers for anti-biofouling surfaces," *J. Mater. Chem.*, vol. 18, pp. 3405–3413, 2008.

[114] K. K. Chung, J. F. Schumacher, E. M. Sampson, R. A. Burne, P. J. Antonelli, and Brennan, "Impact of engineered surface microtopography on biofilm formation of Staphylococcus aureus," *Biointerphases*, vol. 2, no. 2007, pp. 89–94, 2016.

[115] A. T. Poortinga, J. Smit, H. C. V. D. Mei, and H. J. Busscher, "Electric Field Induced Desorption of Bacteria from a Conditioning Film Covered Substratum," *Biotechnology and Bioengineering*, pp. 395–399, 2001.

[116] S. Y. Xiao, L. F. Che, X. X. Li, and Y. L. Wang, "A novel fabrication process of MEMS devices on polyimide flexible substrates," *Microelectronic Engineering*, vol. 85, no. 2, pp. 452–457, 2008.

[117] R. J. Roark, *Roark's Formulas for Stress and Strain*. New York: McGraw-Hill, 1989.

[118] S. S. Rao, *Transverse Vibration of Beams*. Wiley, 2007.

[119] J. W. Weisel, H. Shuman, and R. I. Litvinov, "Protein–protein unbinding induced by force: single-molecule studies," *Current opinion in structural biology*, vol. 13, no. 2, pp. 227–235, 2003.

[120] M. Chiao and J.-C. Chiao, *Biomaterials for MEMS*. Jenny Stanford Publishing, 2011.

[121] H. J. Busscher, W. Norde, and H. C. Van Der Mei, "Specific molecular recognition and nonspecific contributions to bacterial interaction forces," *Appl. Environ. Microbiol.*, vol. 74, no. 9, pp. 2559–2564, 2008.

[122] Y. F. Dufrêne, "Sticky microbes: forces in microbial cell adhesion," *Trends in microbiology*, vol. 23, no. 6, pp. 376–382, 2015.

[123] S. H. Brewer, W. R. Glomm, M. C. Johnson, M. K. Knag, and S. Franzen, "Probing bsa binding to citrate-coated gold nanoparticles and surfaces," *Langmuir*, vol. 21, no. 20, pp. 9303–9307, 2005.

[124] I. Vlasova and A. Saletsky, "Study of the denaturation of human serum albumin by sodium dodecyl sulfate using the intrinsic fluorescence of albumin," *Journal of Applied Spectroscopy*, vol. 76, no. 4, pp. 536–541, 2009.

[125] O. Y. Milyaeva, G. Gochev, G. Loglio, R. Miller, and B. Noskov, "Influence of polyelectrolytes on dynamic surface properties of fibrinogen solutions," *Colloids and Surfaces A: Physicochemical and Engineering Aspects*, vol. 532, pp. 108–115, 2017.

[126] B. Fernández-Montes Moraleda, J. San Román, and L. M. Rodríguez-Lorenzo, "Adsorption and conformational modification of fibronectin and fibrinogen adsorbed on hydroxyapatite. a qcm-d study," *Journal of Biomedical Materials Research Part A*, vol. 104, no. 10, pp. 2585–2594, 2016.

[127] S. Preibisch, S. Saalfeld, and P. Tomancak, "Globally optimal stitching of tiled 3D microscopic image acquisitions," *Bioinformatics*, vol. 25, no. 11, pp. 1463–1465, 2009.

[128] M. Zhang, R. Peltier, M. Zhang, H. Lu, H. Bian, Y. Li, Z. Xu, Y. Shen, H. Sun, and Z. Wang, "In situ reduction of silver nanoparticles on hybrid polydopamine–copper phosphate nanoflowers with enhanced antimicrobial activity," *Journal of Materials Chemistry B*, vol. 5, no. 27, pp. 5311–5317, 2017.

[129] J. R. W. Kestle, "CSF shunts 50 years on past , present and future," *Child's Nervous System*, vol. 16, no. 10-11, pp. 800–804, 2000.

[130] J. Riva-cambrin, J. R. W. Kestle, R. Holubkov, J. Butler, A. V. Kulkarni, J. Drake, W. E. Whitehead, J. C. W. Iii, C. N. Shannon, M. S. Tamber, D. D. L. Jr, C. Rozzelle, S. R. Browd, T. D. Simon, and H. Clinical, "Risk factors for shunt malfunction in pediatric hydrocephalus: a multicenter prospective cohort study," *Journal of Neurosurgery: Pediatrics*, no. April, pp. 382–390, 2016.

[131] I. A. Anderson, L. F. Saukila, J. M. W. Robins, C. Y. Akhunbay-Fudge, J. R. Goodden, A. K. Tyagi, N. Phillips, and P. D. Chumas, "Factors associated with 30-day ventriculoperitoneal shunt failure in pediatric and adult patients," *Journal of Neurosurgery*, vol. Preprint, pp. 1–9, 2018.

[132] Q. Yang, T. Nguyen, C. Liu, J. Miller, J. F. Rhoads, J. Linnes, and H. Lee, "Polyimide-based magnetic microactuators for biofouling removal," in *2016 38th Annual International Conference of the IEEE Engineering in Medicine and Biology Society (EMBC)*, Aug 2016, pp. 5757–5760.

[133] S. Basati, K. Tangen, Y. HSU, H. Lin, D. Frim, and A. Linninger, "Impedance Changes Indicate Proximal Ventriculoperitoneal Shunt Obstruction In-vitro." *IEEE Transactions on Biomedical Engineering*, vol. 9294, no. c, Jul 2014.

[134] B. J. Kim, W. Jin, A. Baldwin, L. Yu, E. Christian, M. D. Krieger, J. G. Mccomb, and E. Meng, "Parylene MEMS patency sensor for assessment of hydrocephalus shunt obstruction," *Biomedical Microdevices*, pp. 1–13, 2016.

[135] J. S. Balami and A. M. Buchan, "Complications of intracerebral haemorrhage," *The Lancet Neurology*, vol. 11, no. 1, pp. 101–118, 2012.

[136] N. J. Naff, D. F. Hanley, P. M. Keyl, S. Tuhrim, M. Kraut, J. Bederson, R. Bullock, S. a. Mayer, E. Schmutzhard, W. R. Selman, W. F. Chandler, H. Garton, C. J. Chittum, S. J. Haines, J. M. Findlay, and R. G. Grossman, "Intraventricular thrombolysis speeds blood clot resolution: Results of a pilot, prospective, randomized, double-blind, controlled trial," *Neurosurgery*, vol. 54, no. 3, pp. 577–584, 2004.

[137] U. Rosenschein, V. Furman, E. Kerner, I. Fabian, J. Bernheim, and Y. Eshel, "Ultrasound imaging–guided noninvasive ultrasound thrombolysis: preclinical results," *Circulation*, vol. 102, no. 2, pp. 238–245, 2000.

[138] N. Kucher, P. Boekstegers, O. Müller, C. Kupatt, J. Beyer-Westendorf, T. Heitzer, U. Tebbe, J. Horstkotte, R. Müller, E. Blessing *et al.*, "Randomized controlled trial of ultrasound-assisted catheter-directed thrombolysis for acute intermediate-risk pulmonary embolism," *Circulation*, p. 113, 2013.

[139] S. Stassi, V. Cauda, G. Canavese, and C. F. Pirri, "Flexible tactile sensing based on piezoresistive composites: A review," *Sensors*, vol. 14, no. 3, pp. 5296–5332, 2014.

[140] C. S. Smith, "Piezoresistance effect in germanium and silicon," *Physical review*, vol. 94, no. 1, p. 42, 1954.

[141] W. Mason and R. Thurston, "Use of piezoresistive materials in the measurement of displacement, force, and torque," *The Journal of the Acoustical Society of America*, vol. 29, no. 10, pp. 1096–1101, 1957.

[142] J. Y. Seto, "Piezoresistive properties of polycrystalline silicon," *Journal of Applied Physics*, vol. 47, no. 11, pp. 4780–4783, 1976.

[143] S. Sahli and D. Aslam, "Ultra-high sensitivity intra-grain poly-diamond piezoresistors," *Sensors and Actuators A: Physical*, vol. 71, no. 3, pp. 193–197, 1998.

[144] S. Lee, A. Reuveny, J. Reeder, S. Lee, H. Jin, Q. Liu, T. Yokota, T. Sekitani, T. Isoyama, Y. Abe, Z. Suo, and T. Someya, "A transparent bending-insensitive pressure sensor," *Nature Nanotechnology*, vol. 11, pp. 472–478, 2016.

[145] C. Stampfer, A. Jungen, R. Linderman, D. Obergfell, S. Roth, and C. Hierold, "Nano-electromechanical displacement sensing based on single-walled carbon nanotubes," *Nano letters*, vol. 6, no. 7, pp. 1449–1453, 2006.

[146] K.-K. Lee, J. He, A. Singh, S. Massia, G. Ehteshami, B. Kim, and G. Raupp, "Polyimide-based intracortical neural implant with improved structural stiffness," *Journal of Micromechanics and Microengineering*, vol. 14, no. 1, pp. 32–37, 2004.

[147] P.-J. Chen, D. C. Rodger, S. Saati, M. S. Humayun, and Y.-C. Tai, "Microfabricated implantable parylene-based wireless passive intraocular pressure sensors," *Journal of Microelectromechanical Systems*, vol. 17, no. 6, pp. 1342–1351, 2008.

[148] Y.-H. Wang, C.-Y. Lee, and C.-M. Chiang, "A mems-based air flow sensor with a free-standing micro-cantilever structure," *Sensors*, vol. 7, no. 10, pp. 2389–2401, 2007.

[149] P. Gideon, F. Ståhlberg, C. Thomsen, F. Gjerris, P. Sørensen, and O. Henriksen, "Cerebrospinal fluid flow and production in patients with normal pressure hydrocephalus studied by mri," *Neuroradiology*, vol. 36, no. 3, pp. 210–215, 1994.

[150] A. R. Aiyar, C. Song, S.-H. Kim, and M. G. Allen, "An all-polymer airflow sensor using a piezoresistive composite elastomer," *Smart Materials and Structures*, vol. 18, no. 11, p. 115002, 2009.

[151] P. Cong, D. J. Young, B. Hoit, and W. H. Ko, "Novel long-term implantable blood pressure monitoring system with reduced baseline drift," in *Engineering in Medicine and Biology Society, 2006. EMBS'06. 28th Annual International Conference of the IEEE*. IEEE, 2006, pp. 1854–1857.

[152] B. Ziaie and K. Najafi, "An implantable microsystem for tonometric blood pressure measurement," *Biomedical Microdevices*, vol. 3, no. 4, pp. 285–292, 2001.

[153] C. Song, A. Aiyar, S.-H. Kim, and M. Allen, "Exploitation of aeroelastic effects for drift reduction, in an all-polymer air flow sensor," *Sensors and Actuators A: Physical*, vol. 165, no. 1, pp. 66–72, 2011.

[154] Y. Shang, X. Ye, J. Feng, H. Zhou, and Y. Wang, "Fabrication and characterization of a polymer/metal bimorph microcantilever for ultrasensitive thermal sensing," *IEEE Sensors Journal*, vol. 14, no. 4, pp. 1304–1312, 2014.

[155] C. Marais and G. Villoutreix, "Analysis and modeling of the creep behavior of the thermostable pmr-15 polyimide," *Journal of applied polymer science*, vol. 69, no. 10, pp. 1983–1991, 1998.

[156] C.-Y. Lee and G.-B. Lee, "Micromachine-based humidity sensors with integrated temperature sensors for signal drift compensation," *Journal of micromechanics and microengineering*, vol. 13, no. 5, p. 620, 2003.

[157] K. Hoffmann, *Applying the wheatstone bridge circuit*. HBM Germany, 1974.

[158] T. Steiner, M. N. Diringer, D. Schneider, S. A. Mayer, K. Begtrup, J. Broderick, B. E. Skolnick, and S. M. Davis, "Dynamics of intraventricular hemorrhage in patients with spontaneous intracerebral hemorrhage: Risk factors, clinical impact, and effect of hemostatic therapy with recombinant activated factor VII," *Neurosurgery*, vol. 59, no. 4, pp. 767–773, 2006.

[159] A. I. Qureshi, A. D. Mendelow, and D. F. Hanley, "Intracerebral haemorrhage," *The Lancet*, vol. 373, no. 9675, pp. 1632–1644, 2009.

[160] B. P. Murphy, T. E. Inder, V. Rooks, G. A. Taylor, N. J. Anderson, N. Mogridge, L. J. Horwood, and J. J. Volpe, "Posthaemorrhagic ventricular dilatation in the premature infant: natural history and predictors of outcome." *Archives of disease in childhood. Fetal and neonatal edition*, vol. 87, no. 1, pp. F37–41, 2002.

[161] F. Guzzetta, E. Mercuri, and M. Spanò, "Mechanisms and evolution of the brain damage in neonatal post-hemorrhagic hydrocephalus." *Child's nervous system : ChNS : official journal of the International Society for Pediatric Neurosurgery*, vol. 11, no. 5, pp. 293–6, 1995.

[162] T. Gaberel, A. Montagne, F. Lesept, M. Gauberti, E. Lemarchand, C. Orset, R. Goulay, T. Bertrand, E. Emery, and D. Vivien, "Urokinase versus Alteplase for intraventricular hemorrhage fibrinolysis," *Neuropharmacology*, vol. 85, pp. 158–165, 2014.

[163] J. N. Goldstein and S. M. Greenberg, "Should anticoagulation be resumed after intracerebral hemorrhage?" *Cleveland Clinic Journal of Medicine*, vol. 77, no. 11, pp. 791–799, 2010.

[164] D. F. Hanley, K. Lane, N. McBee, W. Ziai, S. Tuhrim, K. R. Lees, J. Dawson, D. Gandhi, N. Ullman, W. A. Mould, S. W. Mayo, A. D. Mendelow, B. Gregson, K. Butcher, P. Vespa, D. W. Wright, C. S. Kase, J. R. Carhuapoma, P. M. Keyl, M. Diener-West, J. Muschelli, J. F. Betz, C. B. Thompson, E. A. Sugar, G. Yenokyan, S. Janis, S. John, S. Harnof, G. A. Lopez, E. F. Aldrich, M. R. Harrigan, S. Ansari, J. Jallo, J. L. Caron, D. LeDoux, O. Adeoye, M. Zuccarello, H. P. Adams, M. Rosenblum, R. E. Thompson, and I. A. Awad, "Thrombolytic removal of intraventricular haemorrhage in treatment of severe stroke: results of the randomised, multicentre, multiregion, placebo-controlled CLEAR III trial," *The Lancet*, vol. 389, no. 10069, pp. 603–611, 2017.

[165] L. Basaldella, E. Marton, A. Fiorindi, B. Scarpa, H. Badreddine, and P. Longatti, "External ventricular drainage alone versus endoscopic surgery for severe intraventricular hemorrhage: a comparative retrospective analysis on outcome and shunt dependency." *Neurosurgical focus*, vol. 32, no. 4, p. E4, 2012.

[166] E. A. Ryan, L. F. Mockros, J. W. Weisel, and L. Lorand, "Structural origins of fibrin clot rheology," *Biophysical journal*, vol. 77, no. 5, pp. 2813–2826, 1999.

[167] C. Storm, J. J. Pastore, F. C. MacKintosh, T. C. Lubensky, and P. A. Janmey, "Nonlinear elasticity in biological gels," *Nature*, vol. 435, no. 7039, p. 191, 2005.

[168] J. W. Weisel, "The mechanical properties of fibrin for basic scientists and clinicians," *Biophysical chemistry*, vol. 112, no. 2-3, pp. 267–276, 2004.

[169] R. E. Adams and M. N. Diringer, "Response to external ventricular drainage in spontaneous intracerebral hemorrhage with hydrocephalus." *Neurology*, vol. 50, no. 2, pp. 519–523, 1998.

[170] D. F. Hanley, M. Fisher, and K. Lees, "Intraventricular hemorrhage severity factor and treatment target in spontaneous intracerebral hemorrhage," *Stroke*, vol. 40, no. 4, pp. 1533–1538, 2009.

[171] D. M. Morales, R. Holubkov, T. E. Inder, H. C. Ahn, D. Mercer, R. Rao, J. P. McAllister, D. M. Holtzman, and D. D. Limbrick, "Cerebrospinal fluid levels of amyloid precursor protein are associated with ventricular size in post-hemorrhagic hydrocephalus of prematurity," *PLoS ONE*, vol. 10, no. 3, pp. 1–14, 2015.

[172] H. Park, A. H. Raffiee, S. W. John, A. M. Ardekani, and H. Lee, "Towards smart self-clearing glaucoma drainage device," *Microsystems & Nanoengineering*, vol. 4, no. 1, p. 35, 2018.

[173] S. H. Weisenberg, S. C. Termaath, C. E. Seaver, and J. A. Killeffer, "Ventricular Catheter Development: Past, Present, and Future," *Journal of Neurosurgery*, pp. 1–9, 2016.

[174] M. A. Karami and D. J. Inman, "Analytical modeling and experimental verification of the vibrations of the zigzag microstructure for energy harvesting," *Journal of Vibration and Acoustics*, vol. 133, no. 1, p. 011002, 2011.

[175] D. F. Berdy, P. Srisungsitthisunti, B. Jung, X. Xu, J. F. Rhoads, and D. Peroulis, "Low-frequency meandering piezoelectric vibration energy harvester," *IEEE transactions on ultrasonics, ferroelectrics, and frequency control*, vol. 59, no. 5, pp. 846–858, 2012.

[176] M. Amin Karami and D. J. Inman, "Powering pacemakers from heartbeat vibrations using linear and nonlinear energy harvesters," *Applied Physics Letters*, vol. 100, no. 4, p. 042901, 2012.

[177] M. A. Karami and D. J. Inman, "Electromechanical modeling of the low-frequency zigzag micro-energy harvester," *Journal of Intelligent Material Systems and Structures*, vol. 22, no. 3, pp. 271–282, 2011.

[178] B. J. Nelson, I. K. Kaliakatsos, and J. J. Abbott, "Microrobots for minimally invasive medicine," *Annual review of biomedical engineering*, vol. 12, pp. 55–85, 2010.

[179] W. Andrä and H. Nowak, *Magnetism in medicine: a handbook*. John Wiley & Sons, 2007.

[180] D. G. Nishimura, *Principles of magnetic resonance imaging*. Standford Univ., 2010.

[181] Z. Czosnyka, M. Czosnyka, H. K. Richards, and J. D. Pickard, "Posture-related overdrainage: comparison of the performance of 10 hydrocephalus shunts in vitro," *Neurosurgery*, vol. 42, no. 2, pp. 327–334, 1998.

[182] S. Bratton, R. Chestnut, J. Ghajar, F. H. McConnell, O. Harris, R. Hartl, G. Manley, A. Nemecek, D. Newell, G. Rosenthal *et al.*, "Guidelines for the management of severe traumatic brain injury. viii. intracranial pressure thresholds." *Journal of neurotrauma*, vol. 24, pp. S55–8, 2007.

[183] I. R. Chambers, P. A. Jones, T. M. Lo, R. J. Forsyth, B. Fulton, P. J. Andrews, A. D. Mendelow, and R. A. Minns, "Critical thresholds of intracranial pressure and cerebral perfusion pressure related to age in paediatric head injury," *Journal of Neurology, Neurosurgery & Psychiatry*, vol. 77, no. 2, pp. 234–240, 2006.

[184] M. Smith, "Monitoring intracranial pressure in traumatic brain injury," *Anesthesia & Analgesia*, vol. 106, no. 1, pp. 240–248, 2008.

[185] T. Yamane, O. Maruyama, M. Nishida, M. Toyoda, T. Tsutsui, T. Jikuya, O. Shigeta, and Y. Sankai, "The most profitable use of flow visualization in the elimination of thrombus from a monopivot magnetic suspension blood pump," *Artificial organs*, vol. 28, no. 4, pp. 390–397, 2004.

[186] S. Hashimoto, H. Maeda, and T. Sasada, "Effect of shear rate on clot growth at foreign surfaces," *Artificial Organs*, vol. 9, no. 4, pp. 345–350, 1985.

[187] M. K. Runyon, C. J. Kastrup, B. L. Johnson-Kerner, T. G. Van Ha, and R. F. Ismagilov, "Effects of shear rate on propagation of blood clotting determined using microfluidics and numerical simulations," *Journal of the American Chemical Society*, vol. 130, no. 11, pp. 3458–3464, 2008.

[188] G. K. Reddy, P. Bollam, and G. Caldito, "Long-term outcomes of ventriculoperitoneal shunt surgery in patients with hydrocephalus," *World Neurosurgery*, vol. 81, no. 2, pp. 404–410, 2014.

[189] G. Raffa, L. Marseglia, E. Gitto, and A. Germanò, "Antibiotic-impregnated catheters reduce ventriculoperitoneal shunt infection rate in high-risk newborns and infants," *Child's Nervous System*, vol. 31, no. 7, pp. 1129–1138, 2015.

[190] O. Klein, B. Demoulin, R. Jean Auque, G. Audibert, C. Sainte-Rose, J.-C. Marchal, and F. Marchal, "Cerebrospinal fluid outflow and intracranial pressure in hydrocephalic patients with external ventricular drainage," *Acta Neurologica Scandinavica*, vol. 122, no. 2, pp. 140–147, 2010.

[191] L. Jaques, "Protamine?antagonist to heparin," *Canadian Medical Association Journal*, vol. 108, no. 10, p. 1291, 1973.

[192] M. J. McGirt, J.-C. Leveque, J. C. Wellons III, A. T. Villavicencio, J. S. Hopkins, H. E. Fuchs, and T. M. George, "Cerebrospinal fluid shunt survival and etiology of failures: a seven-year institutional experience," *Pediatric neurosurgery*, vol. 36, no. 5, pp. 248–255, 2002.

[193] J. F. Mustard and M. A. PACKHAM, "Factors influencing platelet function: adhesion, release, and aggregation," *Pharmacological Reviews*, vol. 22, no. 2, pp. 97–187, 1970.

[194] M. Guthold, W. Liu, E. Sparks, L. Jawerth, L. Peng, M. Falvo, R. Superfine, R. R. Hantgan, and S. T. Lord, "A comparison of the mechanical and structural properties of fibrin fibers with other protein fibers," *Cell biochemistry and biophysics*, vol. 49, no. 3, pp. 165–181, 2007.

[195] H. Duong, B. Wu, and B. Tawil, "Modulation of 3d fibrin matrix stiffness by intrinsic fibrinogen–thrombin compositions and by extrinsic cellular activity," *Tissue Engineering Part A*, vol. 15, no. 7, pp. 1865–1876, 2009.

[196] J. J. Abbott, O. Ergeneman, M. P. Kummer, A. M. Hirt, and B. J. Nelson, "Modeling magnetic torque and force for controlled manipulation of soft-magnetic bodies," *IEEE Transactions on Robotics*, vol. 23, no. 6, pp. 1247–1252, 2007.

[197] B. D. Cullity and C. D. Graham, *Introduction to magnetic materials*. John Wiley & Sons, 2011.

[198] J. Osborn, "Demagnetizing factors of the general ellipsoid," *Physical review*, vol. 67, no. 11-12, p. 351, 1945.

[199] A. Aharoni, "Demagnetizing factors for rectangular ferromagnetic prisms," *Journal of applied physics*, vol. 83, no. 6, pp. 3432–3434, 1998.

[200] D.-X. Chen, J. A. Brug, and R. B. Goldfarb, "Demagnetizing factors for cylinders," *IEEE Transactions on magnetics*, vol. 27, no. 4, pp. 3601–3619, 1991.

[201] D.-X. Chen, E. Pardo, and A. Sanchez, "Fluxmetric and magnetometric demagnetizing factors for cylinders," *Journal of Magnetism and Magnetic Materials*, vol. 306, no. 1, pp. 135–146, 2006.

[202] G. Elsner, "Residual stress and thermal expansion of spun-on polyimide films," *Journal of applied polymer science*, vol. 34, no. 2, pp. 815–828, 1987.

[203] J. C. Simpson, J. E. Lane, C. D. Immer, and R. C. Youngquist, "Simple analytic expressions for the magnetic field of a circular current loop," 2001.

[204] D. M. Tanner, J. A. Walraven, K. Helgesen, L. W. Irwin, F. Brown, N. F. Smith, and N. Masters, "Mems reliability in shock environments," in *2000 IEEE International Reliability Physics Symposium Proceedings. 38th Annual (Cat. No. 00CH37059)*. IEEE, 2000, pp. 129–138.